STUDY OF COLLOIDAL TRANSPORT AND MULTIPHASE FLOW IN BEAD-BASED MICROMODELS WITH SURFACE CHARGE AND WETTABILITY HETEROGENEITIES

by

Yang Guo

A thesis submitted to the Faculty and the Board of Trustees of Colorado School of Mines in partial fulfillment of the requirements for degree of Doctor of Philosophy (Chemical Engineering).

Golden, Colorado

Date ____________________________

Signed: __________________________
Yang Guo

Signed: __________________________
Dr. Keith B. Neeves
Thesis Advisor

Signed: __________________________
Dr. Ning Wu
Thesis Advisor

Golden, Colorado

Date ____________________________

Signed: __________________________
Dr. Anuj Chauhan
Professor and Head
Department of Chemical and Biological Engineering

ABSTRACT

Micromodels are porous media analogs that help scientists understand the transport phenomena in real-world porous media at the laboratory scale. Compared with traditional field- and column-scale experiments, micromodels have two distinct advantages: (1) its transparency allows researchers to directly visualize relevant transport phenomena occurred inside through optical microscopy. (2) its highly controllable physicochemical properties allow scientists to conveniently decouple the porous medium parameters from various process parameters and study their specific or synergistic impacts systematically.

In this thesis we developed new approaches to fabricate bead-based micromodels to study the pore-scale and population behavior of colloidal transport and multiphase flow through porous media. By injecting microscopic beads with different surface functionalities in a microfluidic channel, we were able to fabricate unconsolidated porous media analogs with surface charge and wettability heterogeneities. We also developed a MATLAB program that detected the mass center of each bead in the porous media, which allowed us to replicate the exact experimental domains in numerical simulators for faithful comparison between experiments and modelling. For colloidal transport in porous media with surface charge heterogeneity, we performed experiments at the single pore level and directly extracted the deposition coefficient between colloidal particles and the bead collectors under the favorable deposition conditions. Meanwhile we also obtained the surface blocking function of the particle deposition. Both information can be used directly in numerical simulations, thus eliminating the need of fitting parameters. We obtained a good agreement in the deposition coefficient between pore-scale and population experiments. We further used Norland Optical Adhesive 81 (NOA81) as the material to fabricate micromodels with heterogeneous wettability. Due to its high elastic modulus NOA81 can sustain

high pressure during multiphase flow. Our preliminary experiments for the displacement of oil by water demonstrated the feasibility of studying multiphase flow in a close-packed porous medium with wettability heterogeneities.

TABLE OF CONTENTS

LIST OF FIGURES

LIST OF TABLES

ACKNOWLEDGEMENTS

Here at this point of my life, I would like to express my sincere gratitude to my thesis advisors Prof. Ning Wu and Prof. Keith Neeves for all the insightful guidance and supportive encouragement when I met difficulties during my PhD work. I would also like to thank my parents, Lei Wang and Wei Guo for your support during the whole school era of my life, without you this would not be accomplished.

Meanwhile, I would like to thank all the collaborators I have worked with. Prof. Xiaolong Yin, Dr. Jae Kyoung Cho, Dr. Kenton Rod, Dr. Jaehun, Chun, and Dr. Wooyoong Um, your invaluable advices really make my research better. I also want to thank all the people from Neeves and Wu's labs: Dr. Adam Wufsus, Dr. Abimbola Onasoga-Jarvis, Dr. Joanna Sylman, Dr. Marcus Lehmann, Dr. Rogier Schoeman, Dr. Kuldeepsinh Rana, Matthew Sorrells, Chidiebere Agwu, Dante Disharoon, Alison Wallbank, Dr. Onur Tasci, Dr. Fuduo Ma, Dr. Sijia Wang, Dr. Chixia Tian, Dr. Jingjing Gong, Dr. Tao Yang, Xingfu Yang, It was really a pleasure to work with you in the past 5 years. Dr. Kevin Roth and Dr. Aditya Kasukurti, thank you for teaching my photolithography skills. David Goggin and Sijia Hu, thank you for teaching me how to measure viscosity and contact angle. Prof. Tissa Illangasekare, it was a pleasure to be in your class and I really enjoyed your lectures.

At last I want to thank all my friends, Nan Zheng, Dr. Dehui Yang, Jincheng Lou, thank you for all the time we spent on snow. Dr. Yisu Nie, Dr. Zhihong Yuan, Dr. Rongpeng Zhang, Dr. Jianfeng Liu, Dr. Yue Hu, and Dr. Heewon Jung, thank you for all the good memories we shared together.

CHAPTER 1

INTRODUCTION

Micromodels are porous media analogs that imitate the real world porous environment based on either direct replication or representative simplification. Normally, micromodels have dimensions ranging from several millimeters to several centimeters and the pore size inside varies from several to hundred micrometers. The micromodels have been fabricated with different materials such as glass, silica, calcite, poly(methyl methacrylate) (PMMA), polydimethylsiloxane (PDMS), and Norland Optical Adhesive 81 (NOA81).[1–7] Compared with the conventional column-scale experiments, one of the major advantages of using micromodels lies in the transparency of those materials and therefore researchers could directly visualize relevant transport phenomena occurred inside through optical microscopy. Another strength of using micromodels is its highly controllable physical and chemical environments so that scientists can focus on the experimental conditions that they are interested in and decouple the porous media properties from the influence of other factors such as the flow conditions. Hence, micromodels have become a very useful tool in studying transport phenomena in porous media that have broad societal impacts such as colloid-facilitated contaminant transport and multiphase flow.

Colloidal particles typically range from tens of nanometers to several micrometers in size.[8] In subsurface environments, colloidal particles are released into groundwater from the soil matrix or by human activity. The release of colloidal particles from the soil is caused by perturbations in the hydrogeochemical environment[9] such as the changes in ion concentration, pH, and oxygen level. Human activities such as waste disposal, groundwater recharge, or contaminants leakage can also introduce colloidal particles into groundwater. After entering the subsurface, these colloidal particles could act as a mobile phase and enhance the transport of low solubility contaminants by carrying them together in groundwater. As a result, contaminants such as radionuclides,[10,11] heavy metals,[12,13] and organic substances[14,15] travel much faster and further than by themselves. This phenomenon is the so-called colloid-facilitated transport of contaminants. Similarly, pathogens that have the similar sizes as colloids, when present in groundwater, can also have ramifications on public health.[16,17] Therefore, identifying the transport mechanisms of colloids in soil is essential for predicting the fate of and preventing the spread of contaminants and diseases.

Besides the transport of colloids, multiphase flow in porous media is also commonly encountered. By definition, multiphase flow refers to any fluid flow consisting of more than one phase.[18] Researchers are interested in multiphase flow in porous media because it influences many important environmental or industrial processes including enhanced oil recovery (EOR), geological CO_2 sequestration, non-aqueous phase liquid (NAPL) remediation, and membrane separation.[19–22] Among all those topics mentioned above, EOR is a classical problem since petroleum is the essential material for industrialization. More efficient EOR technologies are desired since currently the average oil recovery rate is still below 40%.[23] Therefore, understanding the oil displacement by water in porous media not only helps the petroleum industry but also provides insights in other types of multiphase flow that are relevant in CO_2 sequestration and NAPL remediation.

Initially, micromodels were made of materials with homogeneous pore size within. This is the so-called homogeneous micromodel. Later on, researchers started to introduce pore size variation based on statistical analysis, real fracture replication or simplified models. These micromodels containing heterogeneous pore size distributions are called physically heterogeneous micromodels. Recently, a few researchers tried to systematically modify the surface properties such as the wettability and surface charge of the micromodels to different extents. But for each individual micromodel, its surface property is still uniform. In this thesis, we developed methods to make bead-based chemically heterogeneous micromodels by introducing microscopic beads (~10 μm in diameter) with different surface properties. Due to the pseudo-three dimensional nature of our porous media, we were able to locate the *x-y-z* coordinate of each bead in our system so that the exact experimental porous media can be faithfully replicated in numerical simulations. Taking the above-mentioned advantages, we applied our experimental system to investigate both the transport of colloids and oil displacement by water. With pore-scale and populational data we revealed key mechanisms for those transport phenomena and demonstrated the effectiveness of our new experimental platform.

CHAPTER 2

LITERATURE REVIEW

2.1 Colloid-facilitated transport of contaminants

The spreading of contaminants in groundwater has been conventionally treated as a two-phase transport problem where the contaminants partition between an immobile solid phase (*i.e.,* soil matrix) and a mobile liquid phase (*i.e.,* groundwater). Previously researchers argued that those less soluble contaminants tend to adsorb on the soil matrix instead of traveling with water. Therefore although some of them may be very detrimental to the environment, people thought the influenced area would be rather limited.[9] More recently, evidence suggests that suspended colloids in groundwater also act as a mobile solid phase to adsorb and accelerate the spreading of otherwise retarded pollutants.[24–29] This process is called the colloid-facilitated transport of contaminants.

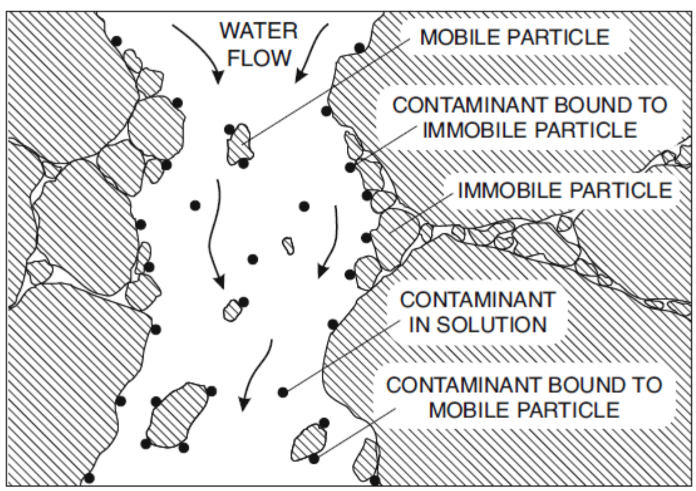

Figure 2.1 Colloid-facilitated transport of contaminants.[26,30] The transport of pollutants (•) is accomplished by either dissolving in the aqueous phase or binding to a colloidal carrier. Reprinted with permission from [26], Copyright (1996) American Chemical Society.

There are four criteria of colloid-facilitated transport of contaminants:[13] (1) Mobile colloids are present; (2) Pollutant molecules adsorb on the mobile colloids; (3) Colloids travel long distance with groundwater flow; and (4) The contaminants are toxic that even a trace amount is intolerable. In the following, we will review the transport of colloidal particles based on the scale of experiments.

2.2 Field scale experiment

Field tracer test (FTT) is the most realistic method to characterize the groundwater flow patterns and subsurface matrix properties. The direct information obtained from FTT includes the measured tracer concentration versus time (*i.e.*, breakthrough curve) at the monitoring locations. From which, two types of information could be extracted: the groundwater transport parameters such as velocity and dispersivity and the aquifer structure parameters such as porosity, preferential flow paths, and structural anisotropy.[31] These data are widely used to build or calibrate aquifer transport models.

A variety of reactive and non-reactive tracers can be used in FTT for different purposes. Non-reactive tracers do not degrade or interact with the subsurface maxtrices, therefore they are often used for characterizing preferential flow paths or aquifer anisotropy. Based on the site condition, non-reactive tracers can be salt-based (chloride and bromide), fluorescent (fluoresceine, eosine, pyranine, sodium naphthionate, and tinopal), radioactive ($^{1}H^{3}HO$ and environmental isotopes), or particulate-based (fluorescent microspheres and micro-organism).[31] Two factors are worth noting in the use of non-reactive tracers. First, laboratory test is required to prove that the selected tracer is truly conservative under the site condition. Second, the local environmental and administrative laws need to be followed. Reactive tracers interact with aquifer materials, hence they can bind to the soil matrix temporarily or permanently. Moreover, the reaction products could further alter the aquifer structure and preferential flow path. Therefore reactive tracers are normally the contaminants themselves and the sites for FTT are usually places already contaminated.

The two primary ways to conduct FTT are natural gradient tracer test (NGTT) and forced gradient tracer test (FGTT). With these methods multiple kinds of tracers (8-10) can be applied within one experiment to extract as much information as possible.[32,33] Multi-tracer experiments use different analytical techniques such as fluorescence spectrometry, ion chromatography, and mass spectrometry to discriminate among tracers. More recently, with the development of multilevel sampling and DNA sequence-based tracers, researchers are able to gather tracer transport data for different aquifer depth in one experiment with much higher sensitivity.

In NGTT, an injection well is placed at the upstream of the groundwater flow for a continuous or pulse injection of tracer solutions, and several sampling wells are located at the downstream to monitor the injectates concentration change over time as shown in Fig. 2.2B. The advantage of NGTT is its natural condition that provides the most realistic data. However, NGTT is often limited by the large amount of experimental efforts due to slow groundwater flow rate under natural conditions. For example, Rugge *et al.* reported a NGTT of a leachate plume down gradient of Grindsted landfill in Denmark, bromide and other tracers were injected for 195 days and the whole experiment lasted for 924 days.[34] Meanwhile, 4-12 monitoring wells were drilled for sampling at five-meter intervals downstream of the injection well. Other important NGTT experiments were performed at Cape Cod (Massachusetts), Columbus (Ohio), and Canadian Forces Base Borden (Ontario). From those experiments researchers learnt the transport of certain chemicals under real hydrological conditions, as well as the effectiveness of lab scale column experiments.

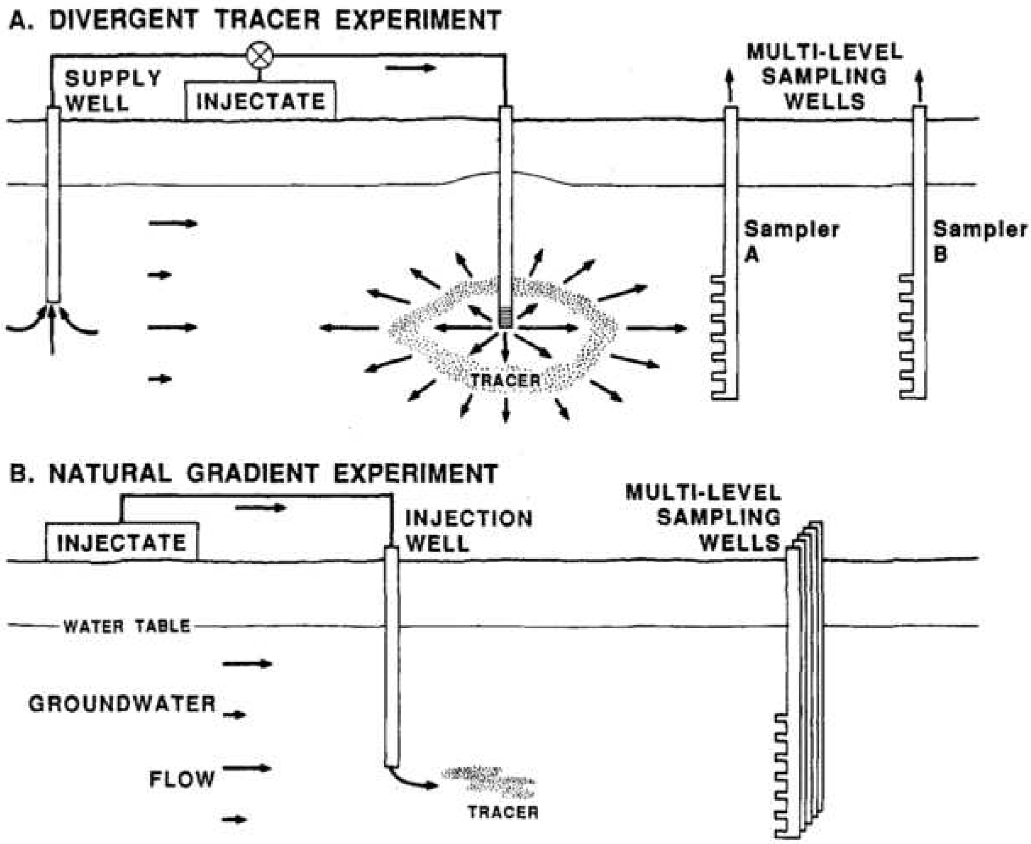

Figure 2.2 Field tracer test schematics.[35] (A) An illustration of the divergent forced gradient tracer test (FGTT). (B) A natural gradient tracer test (NGTT). The FGTT is usually performed under well-defined experiment conditions and takes a relative short period of time, while the NGTT normally has a larger scale.[31] Reprinted with permission from [35], Copyright (1991) American Chemical Society.

In contrast with NGTT, FGTT introduces a much larger pressure gradient between injection and monitoring wells. Hence, the effects of natural gradient variation are minimized and well-defined experimental conditions can be achieved. The experiment duration is also reduced.[31] There are three kinds of setups for a typical FGTT, which are divergent, convergent, and dipole type groundwater flow fields. In the divergent approach, groundwater and tracers are injected through the injection well and monitoring wells are placed in the downstream along one direction or several directions around the injection well. Fig. 2.2A illustrates the procedure. The convergent method pumps the water from an extraction well and tracers are introduced through the surrounding wells. In this method, the tracer breakthrough information is also measured from the extraction well. The dipole flow approach is the combination of two methods mentioned above, which include both injection and withdrawing wells. The groundwater can be recycled and tracers are introduced through the injection well or a third infiltration well. Due to the reduced experimental time in FGTT, many researchers adopted this approach for their field-scale experiments. For example Chen *et al.* used tracer tests in a radially convergent flow field to evaluate transverse dispersivity.[36] Fernandez-Garcia *et al.* used convergent flow tracer tests in an experimental tank to study the applicability of effective transport parameters.[37] And Ptak Brusseau, Annable *et al.* and many other researchers had also used FGTT in field-scale experiments. [38–41]

2.3 Laboratory-scale experiment

Due to the heterogeneous (physical, chemical, or both) aquifer conditions naturally presented in the field, it is very hard to infer any universal laws for colloidal transport. Furthermore, the intensive investment of money and time for field sampling also limits the amount of work that can be done. In order to tackle these problems, researchers started to make porous media in lab with model or real soil grains and conduct experiments based upon these artificial porous media. The advantage of this method is that experiment conditions are well controlled in terms of porous medium properties (*e.g.,* porosity, surface property, structural isotropy) and water chemistry (*e.g.,* pH, ionic concentration, and salt composition). By tuning the relative size of the packed porous medium, the transport process can be approximated in one, two, or three dimensions.[42] The measurement of these experiments is still focused on the effluent colloid concentration over time. Nevertheless, because of the small scale and sensitive detectors (backscatter electron detection,[43] HPLCUV-vis detector,[44] fluorescence spectroscopy[45]), the mass balance for colloids is well preserved. Therefore, the lab-scale experiment data are often used to verify or fit for theoretical colloid transport models.

Due to the advantages described above, a few straightforward measurements provide qualitative results. For example, Torok *et al.* used lab-scale lysimeter experiments to simulate low-level radioactive waste repository and found that ^{137}Cs transport is facilitated by its adsorption on clay particles.[46] Puls and Powell applied a core column collected from Pinal Creek (Arizona) to study the factors that affect both arsenate and hematite transport. They found that both ionic composition and particle size have the most significant influence on the particle breakthrough.[47] Amrhein *et al.* packed roadside soils into columns and studied the influence of deicing salts on trace metal transport. They found that, under low salinity, colloid-facilitated transport occurred and Cu, Pb, Ni, Cr, and Fe concentration were increased in the column leachate.[48] In contrast, under high salinity conditions, colloid-facilitated transport barely happened. Grolimund *et al.* studied the effect of monovalent (Na^+) and divalent (Ca^{2+}) salt solution on the mobilization of strongly sorbing contaminant Pb^{2+} in silt loam soil.[26] They found that the infiltration of low concentration of divalent solution could effectively mobilize Pb^{2+} in a previously high monovalent concentration environment. Roy and Dzombak studied the colloid release due to ionic strength reduction in Ottawa sand column and found the release rate has a weak correlation with ionic strength change, which is different from the prediction of Derjaguin, Landau, Vervey, and Overbeek (DLVO) theory.[14] They attributed this deviation to the surface charge and size heterogeneity of colloids. Noell *et al.* studied the effect of Cs^+ transport with and without the presence of colloids under two different granular size columns. From their experiments, colloids largely facilitated the transport of Cs^+ and the smaller the bed grains were, the more significant the facilitation occured. Karathanasis studied the effects of montmorillonitic, illitic, and kaolinitic colloids on the transport of Cu and Zn in Maury and Loradale core columns. He found that the presence of colloids typically enhanced metal transport by 5 to 50 times compared with runs without colloids. Colloids with strongly negative surface charges and organic carbon contents are more favorable in facilitating Cu and Zn transport. In the opposite, colloids with large size, weakly charged surface, and high Fe- and Al-hydroxyoxide contents showed low capacity to assist their movement.

Apart from those straightforward measurements, researchers have also included more complexities such as the physical and chemical heterogeneities in porous media to investigate the inherent mechanisms that govern the transport of colloidal particles. In 1971, Yao *et al.* first linked the macroscopic advection-diffusion transport model with three additive microscopic mechanisms that control colloids retention: diffusion, interception, and sedimentation.[49] This started the development of the so-called classic colloidal filtration theory (CFT). Although from his model the predicted collector efficiency of colloids is several times different from the experimental values obtained in a sand-packed column, his theory successfully predicted a minimum collector efficiency when the colloidal particle size is around 1 μm. Since Yao's initial work there has been significant effort to modify CFT. These efforts will be presented in the next section.

The CFT was developed based on the average properties of the porous medium, hence, many researchers tried to expend its usage to porous media that possess physical and chemical heterogeneities. Elimelech *et al.* randomly mixed negatively and positively charged quartz beads to form a chemically heterogeneous column and characterized the porous medium as a whole with the mean zeta potential. They found that the experimental colloid retention results were very different from the calculation of DLVO theory based upon the average grain zeta potential.

It indicates that, for chemically heterogeneous porous medium, new characterization metrics beyond mean zeta potential should be used.[50] Chen *et al.* built a heterogeneous column with layered structures.[51] In contrast with Elimelech's findings, spatially varied chemical heterogeneities such as layers did not influence the overall behavior of colloids breakthrough. They found that using an average deposition rate over the entire column in the model is sufficient to match the actual experiment outcome. Johnson *et al.* adopted the same method to pack a chemically heterogeneous column as Elimelech *et al.*, but they used a random sequential adsorption (RSA) based blocking function to predict the colloids deposition rate and their results matched experiments well.[52] Bradford *et al.* studied the effect of relative size between colloids and porous medium grains for both homogeneous and physically heterogeneous porous media. They found that when the ratio between particles and median grain diameter (d_p/d_{50}) is over 0.005 straining could become a significant mechanism for colloids retention. It is important to note that straining is not considered in the standard CFT.[45,53] By dissecting the sand column after experiments, they found straining mostly happened at the column inlet.

2.4 The colloid filtration theory

As mentioned above, the first colloid filtration model was developed by Yao *et al.*[49] In this seminal study, they defined each of bead in the packed bed as a spherical collector. It removes suspended particles from the bulk flow based on three different mechanisms: interception, sedimentation, and diffusion.

The interception is the physical contact between the collector and finite-sized particles when they flow along the streamline. Sedimentation is the physical contact caused by the gravitational force. And diffusion is the contact due to Brownian motion of particles. All these three effects were assumed to contribute additively to the single collector efficiency η_0, which is defined as the ratio between the number of particles contact with the collector and that flowing toward the collector per unit time.

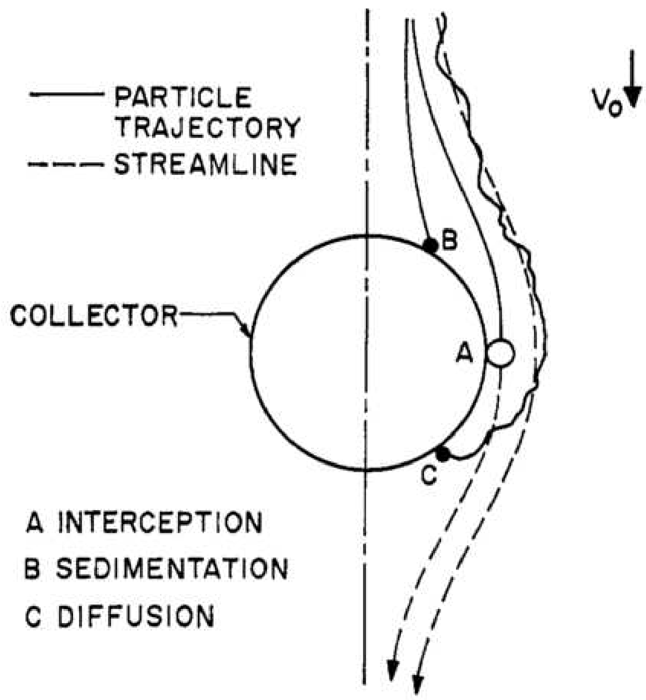

Figure 2.3 Schematics of three colloid removal mechanisms.[49] Reprinted with permission from [49], Copyright (1971) American Chemical Society.

The performance of a packed bed can then be related to the efficiency of a single spherical collector by

$$ln\frac{C}{C_0}=-\frac{3}{2}(1-f)\alpha\eta_0\left(\frac{L}{d}\right) \tag{2.1}$$

where C and C_0 are the effluent and influent particle concentration, respectively. f is the porosity of the bead packing, α is the collision efficiency, L is the bed depth, and d is the individual collector's diameter. Meanwhile, the transport equation that governs the particle concentration under steady state can be written as [8]

$$\nabla\cdot(\mathrm{u}C)=\nabla\cdot(D\nabla C)-\nabla\cdot\left(\frac{D\mathrm{F}}{k_BT}C\right) \tag{2.2}$$

where $\boldsymbol{u}$ is the fluid velocity, D is the diffusion coefficient, $\boldsymbol{F}$ is the body force, k_B is the Boltzmann constant, and T is the temperature. The term on the left represents the advection and the terms on the right describe the effect of diffusion and body forces (such as gravity), respectively. The interception effect is included in the boundary condition, *i.e.*, $C = 0$ at a distance $|\mathbf{r}| = (d + d_p)/2$, where d_p is the diameter of the suspended particles. The other boundary condition is $C = C_0$ at $r \to \infty$. In order to solve Eq. 2.2 analytically, several other assumptions need to be made. For example, the Stokes flow is assumed to be valid. The collision coefficient α is set to 1, and the diffusion coefficient of a particle is estimated by the Stokes-Einstein's equation.

From the two equations mentioned above, η_0 can be solved when each of the three removal mechanisms is dominant:

$$\eta_D = 4.04 Pe^{-2/3} = 0.9\left(\frac{k_B T}{\mu d_p d v_0}\right)^{2/3} \qquad (2.3)$$

$$\eta_I = \frac{3}{2}\left(\frac{d_p}{d}\right)^2 \qquad (2.4)$$

$$\eta_G = \frac{(\rho_p - \rho) g d_p^2}{18 \mu v_0} \qquad (2.5)$$

where Pe is the Peclet number, μ is the fluid viscosity, v_0 is the fluid interstitial velocity. In the above, η_D, η_I, and η_G represent theoretical values for the single collector efficiency when the dominant transport mechanism is diffusion, interception, or sedimentation, respectively. In a comparison between numerical solution of Eq. 2.2 and the analytical solutions (*i.e.,* Eq. 2.3-5), Yao *et al*. found η_0 approximately equals to the sum of those analytical expressions, *i.e.,*

$\eta_0 = \eta_D + \eta_I + \eta_G$.[49] This model successfully captured the trends of the removal efficiency for suspended particles of different sizes and correctly predicted the particle size that leads to the minimum removal efficiency. But its predicted collector efficiency for most particle size tested has an error of more than 50% of the experimental data.

Later Rajagopalan *et al.*[54] developed another model based on the trajectory analysis of fluid flow in Happel's sphere-in-cell fluid envelope model.[55] In Happel's model, the porous medium is an assemblage of identical spherical collectors. Each collector is surrounded by a fluid shell with the same thickness, which is determined from the porosity of the medium.

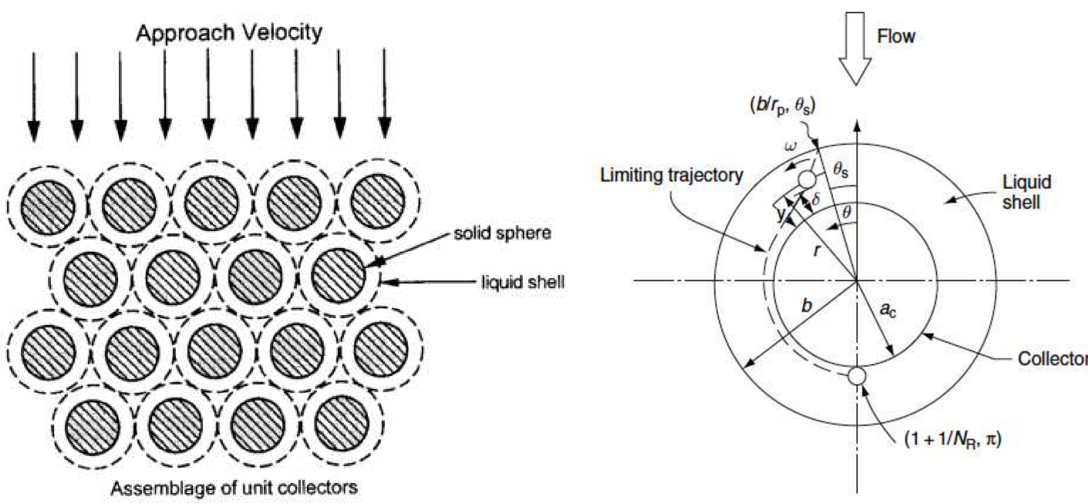

Figure 2.4 Happel's sphere-in-cell model and the associated spherical coordinate system.[8,54] Reprinted with permission from [8], Copyright (1996) Elsevier. Reprinted with permission from [54], Copyright (2004) John Wiley and Sons.

The flow field inside each liquid shell can be calculated from the stream function in a spherical coordinate

$$v_r = \frac{1}{r^2 \sin\theta} \frac{\partial \psi}{\partial r} \tag{2.6}$$

$$v_\theta = -\frac{1}{r \sin\theta} \frac{\partial \psi}{\partial r} \tag{2.7}$$

The corresponding boundary conditions are

(1) the radial velocity at the outer surface of the liquid shell is zero, *i.e.*, at $r = a_c$:

$$v_r = U\cos\theta \tag{2.8}$$

$$v_\theta = -U\sin\theta \tag{2.9}$$

(2) the tangential stress at the outer surface is zero, *i.e.*, at $r = b$,

$$\frac{\partial v_r}{r\partial\theta} + \frac{\partial v_\theta}{\partial r} - \frac{v_\theta}{r} = 0 \tag{2.10}$$

(3) no-slip at the solid-liquid boundary, *i.e.*, at $r = b$,

$$v_r = 0 \tag{2.11}$$

The resulting expression for the stream function is

$$\psi = \frac{U}{2}\sin^2\theta a_c^2\left(\frac{K_1}{r^*} + K_2 r^* + K_3 r^{*2} + K_4 \mathrm{r}^{*4}\right) \tag{2.12}$$

where $r^* = \dfrac{r}{a_c}$, $K_1 = \dfrac{1}{w}$, $K_2 = \dfrac{\left(3+2p^5\right)}{w}$, $K_3 = \dfrac{p\left(3+2p^5\right)}{w}$, $K_4 = -\dfrac{p^5}{w}$, $w = 2-3p+3p^5-2p^6$,

and $p = \left(1-\varepsilon\right)^{1/3} = a_c / b$.

After the flow field was obtained, they further accounted for the particle sedimentation, convection, van der Waal force, drag force, and double layer interaction to derive a limiting trajectory of suspended particles that approach the collector. When a particle's trajectory falls in between the limiting trajectory and the collector's surface, it is captured. In their model, they first considered that η_0 is only a function of η_I and η_G, with the assumption that the suspended particles are non-Brownian. Later they solved the governing trajectory equation numerically and found the relationship between η_0, η_I, and η_G in terms of dimensionless parameters that characterize different interactions. Then they used Yao's additive assumption to add the effect of diffusion into the final formula

$$\eta_0 = 4A_s^{1/3}Pe^{-2/3} + A_s N_{LO}^{1/8} N_R^{15/8} + 3.38\times10^{-3} A_s N_G^{1.2} N_R^{-1.4} \tag{2.13}$$

where A_s is a porosity-dependent parameter defined by Happel:[55]

$$A_s = \frac{2\left(1-\gamma^5\right)}{2-3\gamma+3\gamma^5-2\gamma^6} \text{ and } \gamma = \left(1-f\right)^{1/3}$$

N_{LO}, N_R, and N_G are the dimensionless parameters that characterize the van der Walls attraction, particle/collector size ratio, and gravitational effect:

$$N_{LO} = \frac{4A_{123}}{9\pi\mu d_p^2 U} \tag{2.14}$$

$$N_R = \frac{d_p}{d} \tag{2.15}$$

$$N_G = \frac{\left(\rho_p - \rho\right) g d_p^2}{18\mu U} \tag{2.16}$$

It is noted that the inclusion of van der Walls attraction in Eq. 2.13 provides a better prediction than Yao's model. However, Rajagopalan's model assumed that particles are removed only when the double layer interaction between the particle and the collector is attractive. This leaves room for improvement of the collision efficiency α because repulsive interaction between particles and collectors can also lead to particle deposition.

In 2004, Tufenkji *et al*. published two papers to further improve the accuracy of the CFT. In the first paper,[56] they pointed out that for Brownian particles, all previous models neglected the influence of hydrodynamic and van der Waals interactions. In their work, instead of directly adding the Levich equation to model diffusion, they used numerical regression to obtain η_D as a function of N_R, Pe, and N_{vdW}. Then the influence of interception was added to obtain another set of optimum coefficients for N_R, Pe, and N_{vdW}. The expression for η_I was obtained by subtracting the diffusion term. The same method was applied for getting η_G. The general equation for η_0 is

$$\eta_0 = 2.4 A_s^{1/3} N_R^{-0.081} Pe^{-0.715} N_{vdW}^{0.052} + 0.55 A_s N_R^{1.675} N_A^{0,125} + 0.22 N_G^{1.11} N_R^{-0.24} N_{vdW}^{0.053} \tag{2.17}$$

where $N_A = A_{123} / 3\pi\mu d_p^2 U$ and $N_{vdW} = A_{123} / k_B T$. They reflect the effect of van der Waals attraction on the interception and diffusion terms. The rest of the parameters are the same as what were defined by Rajagopalan *et al*.[54]

The η_0 calculated by Eq. 2.17 matches the numerical solution of Eq. 2.2 very well. But it still cannot predict particle deposition under the scenario of double layer repulsion. In order to solve this problem, Tufenkji *et al.* proposed a dual-deposition mode (DDM) model,[57] which proposed that even when the particle-collector interaction is repulsive, there could still exist a secondary energy minimum that causes particle deposition. Therefore, the authors defined two deposition modes. The first is fast deposition, where particles deposit in the secondary energy minimum under an unfavorable condition or particles deposit in the primary energy minimum under a favorable condition. The second deposition mode is slow, where particles overcome the energy barrier to deposit in the primary energy minimum under an unfavorable condition. After accounting for the influence of the secondary energy minimum, the improved filtration equation contains an extra deposition rate coefficient k, which converts Eq. 2.1 to

$$C(x) = C_0 \int_0^{\infty} \exp\left[-\frac{k}{v} x\right] p(k)\,\mathrm{d}k \tag{2.18}$$

and

$$p(k) = f_{slow} \frac{1}{\sigma_{slow}\sqrt{2\pi}} \exp\left[-\frac{1}{2}\left(\frac{k-\bar{k}_{slow}}{\sigma_{slow}}\right)^2\right] + f_{fast} \frac{1}{\sigma_{fast}\sqrt{2\pi}} \exp\left[-\frac{1}{2}\left(\frac{k-\bar{k}_{fast}}{\sigma_{fast}}\right)^2\right] \tag{2.19}$$

where $p(k)$ represents the bimodal distribution of the deposition rate coefficient k.[58] Here, f is the fraction of particle deposition caused by slow (f_{slow}) or fast (f_{fast}) deposition. σ_{fast} and σ_{slow} are the corresponding standard deviations. In Eq. 2.19 $\bar{k}_{slow}$ and f_{slow} can be regressed from experimental data. $\bar{k}_{fast}$ is calculated from $\bar{k}_{fast} + 3\sigma_{fast} = 1$ and f_{fast} is calculated from $1 - f_{slow}$. With this correction, they obtained the calculated particle deposition that matches very well with experimental data.

2.5 Micromodel experiment

Micromodels are typically made of glass, silicon, or polymers with pores sizes ranging from 1 to 100 µm and their overall dimensions are on the order of millimeters to centimeters.[59] Typically the pore networks of these micromodels consist of periodic features such as arrays of polygons,[60] random networks with statistically similar porosity and permeability of real rocks,[61] or replicas of real rock pore spaces based on imaging data.[62] Micromodels have been particularly useful in visualizing and simulating water, surfactant, and polymer flooding of oil-saturated pore networks that mimic sedimentary rocks.[61–65] Lately researchers started to use micromodels in the study of colloidal particles filtration.[66–68]

2.5.1 Micromodel experiment

Since its debut in 1950s, researchers had developed several methods to fabricate micromodels. Each of them has its own advantages and drawbacks.

2.5.1.1 Etching

There are two ways of etching, wet etching was first applied to make micromodel by Mattax *et al.*[70] At that time photoresist had not been developed to protect the matrix surface, therefore, they used a layer of wax on the glass as the protection layer. In order to etch the channel network, they used a stylus to scribe lines through the wax and expose the glass surface for hydrofluoric acid etching from 1 to 3 minutes. After etching, the wax layer was removed and a second glass plate was fused to the etched glass through annealing. Later micromodels based on wet etching basically followed the same procedure except using photoresist instead of wax to protect the unetched area. Lenormand *et al.* etched a network pattern on glass to mold resin micromodel and conducted immiscible solvent displacement and obtained a phase diagram for the first time for different viscosity ratios and capillary numbers.[71,72] Xu *et al.* further extended the etching depth in the horizontal directions and formed a 2.5 dimensional glass micromodels.[1]

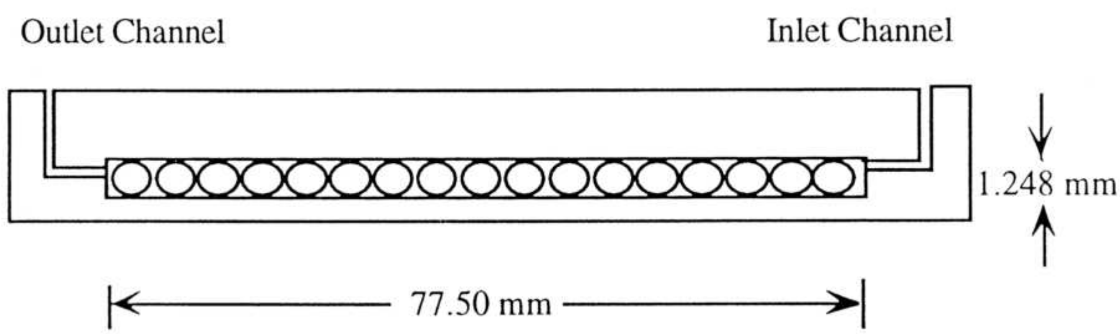

Figure 2.5 A monolayer of glass beads sandwiched between two glass plates (side view), similar to the very first micromodel used by Chatenever and Calhoun.[69] Reprinted with permission from [69], Copyright (1996) Elsevier.

Wet etching is a relatively mature and inexpensive method for micromodel fabrication. Also, due to the high modulus of glass, wet etching made micromodels withstand high pressure in experiments. Along with the advantages, it also has several shortcomings. First, the isotropic erosion of the hydrofluoric acid could lead to a round shape at the bottom of the channel, this curvature causes refraction of light and affects the quality of images captured from the microscope.[73] Second, the wet etching process could cause channel size variation in the micromodel, many researchers have encountered such problem and it impaired the conclusions drawn from their studies.[71,74] Third, the uncontrolled isotropic erosion limited the aspect ratio of the channel. Hence it is very hard to fabricate 3D micromodel with this method.

Dry etching includes several methods like plasma etching, chemical dry etching, reactive ion etching (RIE) *et al.*[75] In this process, plasmas or ions are shot onto the bare silica surface, by chemical reaction or physical momentum transfer, atoms are removed from the silica surface. Laser etching is another dry etching method, but its working principle is more like a direct cutting rather than reacting at atomic level.[76] Therefore its accuracy is not as good as other methods. The advantage of dry etching is its etching direction is highly controllable. The wall of the microchannel produced is nearly vertical with very low surface roughness, and the aspect ratio of the channel depth versus width can reach 20:1.[77,78] The shortcomings of dry etching mostly lie on the expensive equipment setup and toxic gases used or generated.

2.5.1.2 Solid freeform fabrication

Solid freeform fabrication manufactures micromodels from liquid polymer or solid powder. Among them stereolithography is the mostly used and versatile fabrication process that was first proposed by Hull.[79] The working mechanism is that controlled solidification of liquid polymer is assisted by a laser beam, and by lowering/rising the platform in the liquid polymer container, additional layers of the structure is added piece by piece.[59,80] The advantage of stereolithography is its 3D construction ability and flexibility of design, which could come from software drawing, mathematical description or scanning image of a real object.[81] The last part makes this method very useful in biomedical application such as surgeon preparation, implantable devices and tissue engineering.[82–85] The disadvantages of this technology are its expensive setup and relative low resolution in terms of fabricating porous media. Besides, the limited selection of photocurable polymer is another drawback, but this problem is diminishing because more and more photocurable resins are developed.

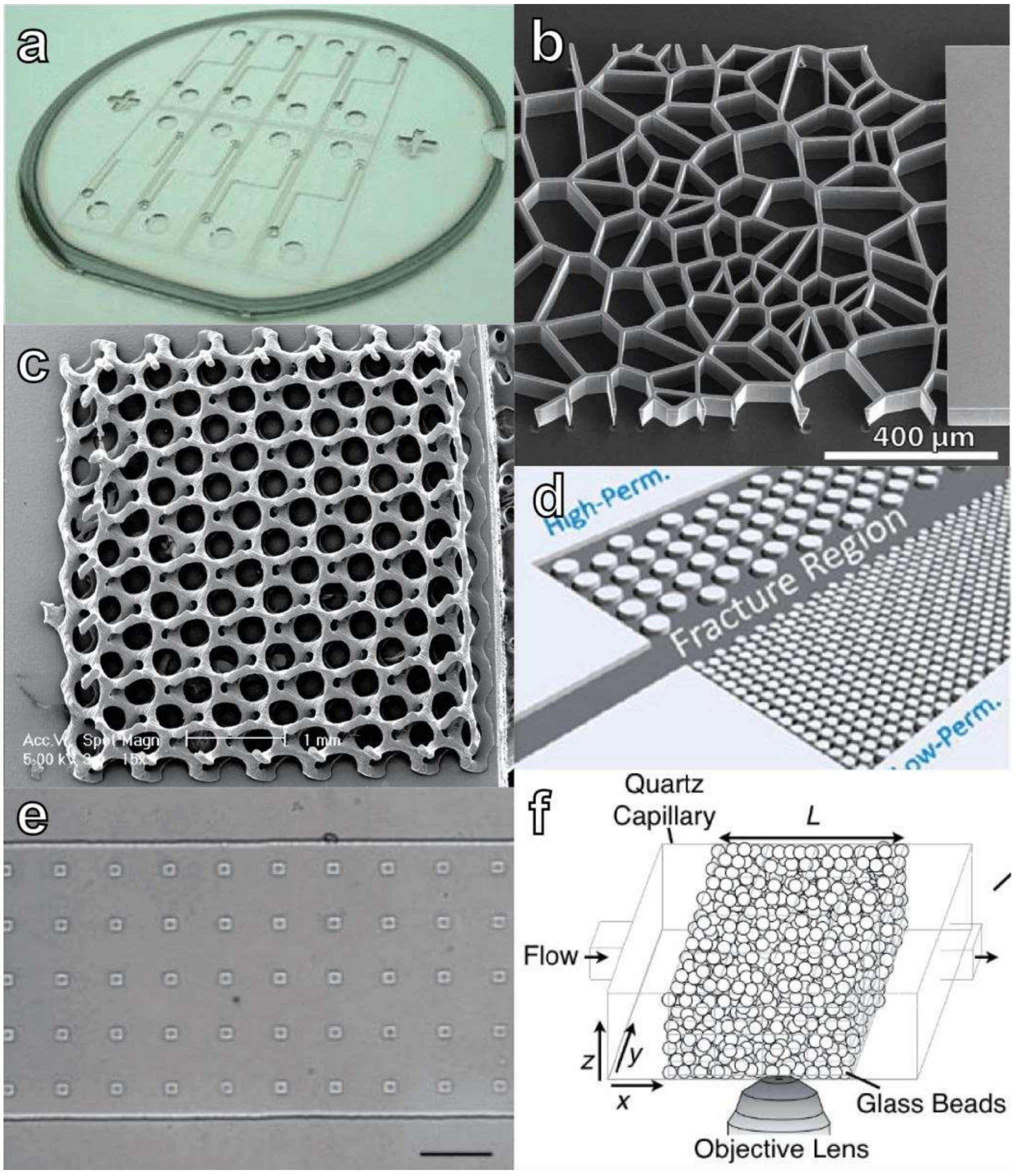

Figure 2.6 Examples of micromodels fabricated with different methods. (a) Wet etching.[73] (b) Dry etching.[61] (c) Stereolithography.[86] (d) Photo and soft lithography.[7] (e) Stop flow lithography.[87] (f) Beads packing.[2] Reprinted with permission from [73], Copyright (2007) Elsevier. Reproduced from [61] [87]with permission from The Royal Society of Chemistry. Reprinted with permission from [86], Copyright (2012) American Chemical Society. Reprinted with permission from [86], Copyright (2009) American Chemical Society. Reprinted with permission from [7], Copyright (2018) American Chemical Society. Reprinted with permission from [2], Copyright (2013) John Wiley and Sons.

2.5.1.3 Photo and soft lithography

Currently, photo and soft lithography are the most widely used combination to fabricate micromodels. Normally photolithography is first used to make a master mold on a wafer or glass slide. In this step, a layer of UV-curable polymer called photoresist is first spin coated on the wafer. The thickness of the photoresist, which is also the channel depth of the micromodel, is controlled by its viscosity and the spin rate. After spin coating, the wafer is transferred onto a hot plate to evaporate the solvent in the photoresist, which is usually called soft baking. Then it is placed under a UV mask aligner for exposure. The mask is designed beforehand with computer software and then fabricated with UV blocking paint either filling the patterned region or the unwanted space, depending on the type of photoresist used. During the UV exposure, if the exposed photoresist is hardened, it is called negative photoresist, if it is softened and become more soluble in the developer, it is called positive photoresist. After the exposure, the negative photoresist usually needs an additional step of hard baking to crosslink the polymer, but this step is not necessary for positive photoresist. The last step of photolithography is to immerse the wafer in the developer that dissolves the residue photoresist.

During early time when photolithograph was first invented, a glass slide cover was directly placed on the manufactured photoresist to make the micromodel. This method suffered from sealing problems because some features made of photoresist were too small to form a solid bonding to the glass cover. Meanwhile, the photoresist itself generated N_2 bubbles under UV light, which also caused the device to fail.[59]

In order to solve this problem, people developed soft lithography that used photoresist as a mold to shape the micromodel made of other elastomeric materials such as polydimethylsiloxane (PDMS).[88] In their procedures, commercially available PDMS prepolymer and curing agent were mixed at 10:1 (mass ratio) and degassed under vacuum. After fully degassing, the mixture was poured onto the master mold and cured for 1h at 65℃. Afterwards the PDMS was peeled off from the mold, cleaned with ethanol, dried, and plasma bonded with another piece of pristine PDMS. The successful application of PDMS on micromodel has brought a lot of innovative research in multiple disciplines such as biology, physics, and chemistry.[6,88,89] However, in multiphase flow studies, this method has some drawbacks such as low modulus and swelling by oil. To overcome these problems, researchers further developed other materials such as NOA81 that has a much higher modulus and stronger chemical resistance.[90,91]

2.5.1.4 Stop flow lithography

In 2001, Love *et al*. first conducted continues lithography in a microchannel with shuttered UV light focused by an microscopic objective.[87,92,93] Later on Lee *et al*. improved this technique, *i.e.*, the stop flow lithography, to fabricate porous media inside a glass microchannel.[94] The basic principles were first coating a layer of 3-(trimethoxysilyl)propyl acrylate at the channel surface to promote polymer adhesion. Then mixtures of crosslinker, monomer, and photoinitiator were injected into the channel. A photomask was placed into the field stop of the microscope for the desired pattern. During the UV exposure, the flow was stopped for bonding between polymer and the glass substrate. After the porous medium was formed, the unreacted polymer was washed off with acetone. The advantages of this method are easy setup and flexible material choices for controlling different surface properties of the porous media. For example, Lee *et al.* modified the wettability of the porous media by using different monomers and the water contact angle were varied from 60° to 144°.[94] The current drawback of this method is the pore-space in the micromodel is still big (~100 μm) and its performance under high pressure is still unknown.

2.5.1.5 Packing by Beads

Beads packing is the oldest method to make the micromodel because of the simplicity of sandwiching a monolayer of beads between two glass plates. In 1952, Chatenever *et al*. first used this method to observe water displacing filtered crude oil at both channel flow and slug flow regimes.[95] At that time the beads created pore sizes at the sub-millimeter level, much bigger than those in real reservoirs. Therefore later on researchers used the etching method that generated pore size about tens of micrometers-on the high end of real sandstone reservoirs. Moreover, the pore-throat network fabricated with etching was easier to be modeled in numerical simulation. In 2013, Datta *et al.* used beads packing with refractive index matching to observe multiphase flow in 3D.[2] They first packed and sintered 35 μm glass beads in a rectangular glass capillary. By using fluorescent index-matching fluid, they observed both the structure of the porous medium and the liquid flow under a fast-scanning confocal microscope. This is the first micromodel that provides detailed insight in 3Dmultiphase flow. However, for the observation of the 3D dynamics is limited by the scanning speed of the confocal microscope.[96]

2.5.2 Application of micromodels in studies of colloidal transport and multiphase flow

The application of micromodels in studying porous medium flow can be dated back to 1950s, when Chatenever and Calhoun sandwiched a monolayer of 0.007” glass beads between two glass plates,[95] from which they were able to observe two-phase flow of water and crude oil under flow rates ranging from 350 ft to 1000 ft per day. But due to the immature image processing techniques at that time, quantitative analyses were impossible. Therefore, micromodels were not widely used until 1980s, when Lenormand *et al.* conducted a series of experiments on transparent array micromodels to study two-phase liquid displacement under different flow conditions.[60,71,97,98]

2.5.2.1 Application of micromodels in colloidal transport

Due to good agreement between experimental results and theoretical predictions, micromodels returned to people's sight as an important experimental tool for colloidal transport study. In 1994, Wan and Wilson studied the retention of 1 μm colloidal particles in an unsaturated micromodel which was patterned by both regularly and irregularly spaced glass-based pillar arrays.[99] As they introduced air bubbles in the channel, they observed that particles were preferably adsorbed on the air-water than the solid-water interface because of the reduction of interfacial energy. The colloid sorption on the air-water interface increased at higher ionic strength and when the particles became more hydrophobic.

Since Lenormand's work, micromodels had become widely used for multiphase flow research.[100] But it was not until twenty-first century that people started to apply them for studying colloidal transport in porous media. For example, Keller *et al.* tried both rock-pattern replica and artificial pillar array micromodels to visualize the transport of particles of various sizes.[66,101] According to their work, smaller particles have more access to the side of the channel, hence they are more likely to go through detours if there are branched channels on the side. And these detours result in a long residential time. In contrast, larger colloids tend to stay closer to the center of the flow, therefore they have less access to the branches and essentially a shorter residential time. Their work directly proved the effect of size exclusion and demonstrated that colloids size should be an important factor to consider for computational simulation. In 2006, Auset and Keller adopted similar micromodels to study the straining effect and the influence of surface roughness of pillars on the retention of particles with different sizes.[68] According to their study, when the size ratio of throat to particle (T/C) is smaller than 1.8, straining is the major mechanism for particle removal, when T/C is larger than 2.5, straining is negligible and interception dominates the retention. Straining only happened at the first one to two pore throats of the micromodel, which was in good agreement with column experiments conducted by Bradford *et al.*[45] In addition, their experiments on rough surface pillars showed that the collision efficiency for particles of different sizes increased by two to three times, compared with smooth pore surfaces. This could be another factor worth noting when people try to model colloidal filtration.

Baumann and Werth studied the trajectories of colloids in a 2D silicon micromodel and compared them with simulations based on the Lattice Boltzmann Method (LBM).[67] Their simulation only took the parabolic flow profile into account and neglected both double layer and van der Waals interactions. Therefore only 50% of the simulated trajectories matched the experimental results. Meanwhile, the collision efficiency determined from their work varied two orders of magnitude for different flow rates, which was too large compared with other results.[102] Hence, both of their experimental methodologies and findings are not very convincing. Later Baumann *et al.* studied the factors that affect colloids dispersion coefficient in both physically homogeneous and heterogeneous silicon micromodels.[103] They measured the longitudinal dispersion coefficient $D_{L,T}$, which is defined as

$$D_{L,T} = \frac{\sigma_{L,T}^2}{2t} \qquad (2.20)$$

where σ is the variance of colloids' velocity distribution. And the longitudinal dispersivity $\alpha_{L,T}$ can be found from

$$D_{L,T} = U\alpha_{L,T} + D^* \qquad (2.21)$$

where U is the average velocity and D^* is the effective diffusion coefficient. Their method was one of the first that measured the dispersion coefficient directly, which represents another advantage of micromodels. The dispersivity measured in the homogeneous micromodel matches the empirical model well, while there are some discrepancies in the heterogeneous micromodel. Moreover, the dispersion coefficient varied in a much narrower range compared with column or field data, which was attributed to the more significant influence of dispersion at larger scales.

Liu *et al.* studied the transport of Cryptosporidium parvum oocysts in a 2D pillar-based silicon micromodel under different pH and ionic concentrations.[104] In all conditions, over 90% oocysts attached to the front half of those pillars. Multiples layers of oocysts could form during the attachment, and the time for multilayers deposition increased with decreasing ionic strength. Moreover, when measuring the percentage of oocysts attachment along the length of the micromodel, they found that the oocysts distribution followed a concave shape: more oocysts attached at two ends of the micromodel and less attached in the middle. The reason, however, remains elusive. After the attachment experiment, they also performed the detachment test by flowing through low ionic strength and high pH solutions. The low ionic strength solution did not release the attached oocysts because they were already located in the primary energy minimum.[57] The high pH solution, however, released more than 60% of the attached oocysts since the adsorption of ions on cells altered the charges on oocysts from being positive to negative. Here an important observation is that an environment pH increase could lead to more oocysts to breakthrough. Later Liu *et al.* introduced chemical heterogeneities into a silicon micromodel.[3] This was achieved by sputtering a thin iron oxide (Fe_2O_3) layer selectively on part of the silicon pillars. They studied the retentions of both polystyrene microspheres and Cryptosporidium parvum oocysts. When the barrier of the DLVO interaction potential between colloids and silicon pillar is low, η is significantly larger in the micromodels where Fe_2O_3 patches were partially coated on silicon pillars than those fully coated micromodels. When the barrier is high, the result, however, is opposite. Although the former phenomenon remains unexplained, the latter was attributed to the so-called hydrodynamic bump,[105] where the high energy barrier between silicon and colloidal particles prevents them from approaching the collector surface. Liu's experiments clearly demonstrated that the presence of chemically heterogeneous patches in micromodels have a great impact on the retention of colloidal particles.

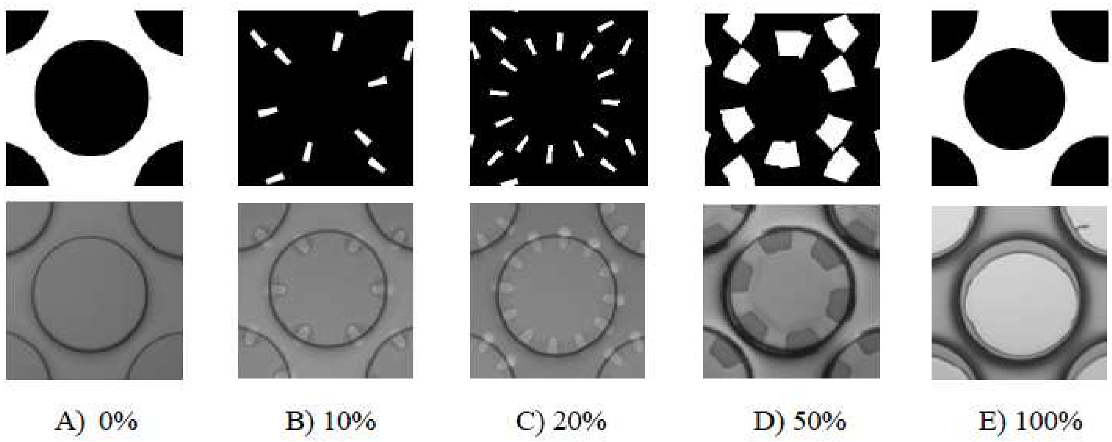

Figure 2.7 Patterned masks (top row) used for the fabrication of heterogeneous Fe_2O_3 patches on silicon micromodels (bottom row).[3] The darker parts on the perimeters of the silicon pillar are the coated Fe_2O_3 patches. Reprinted with permission from [3], Copyright (2013) American Chemical Society.

2.5.2.2 Application of micromodels in multiphase flow

In 1988, Lenormand *et al.* conducted both simulation and experiments in a grid-based micromodel network.[106] In their simulation, they tested two linearization methods (Koplik & Lasseter method and Dias & Payatakes method) to solve the nonlinear problem induced by the capillary pressure. From the simulation, Lenormand *et al.* plotted a phase diagram based on the invading fluid saturation after displacement under various capillary numbers ($Ca=\mu v/\gamma$) and viscosity ratios between invading and defending fluids ($M = \mu_2/\mu_1$). They also found three distinguishing regimes where viscous fingering, capillary fingering, and stable displacement are observed. In the corresponding experiments, they used fluids of different viscosities and achieved similar ranges of *Ca* and *M* as in the simulation. And their experimental results validated the numerical prediction. Later Zhang *et al.* complemented Lenormand's results using oil as the non-wetting invading fluid to displace aqueous defending fluid, and they found a narrower crossover regime from viscous fingering to capillary fingering than that of Lenormand's work.[74] They attributed it to the more homogeneous micromodel that they used. It is also possible that the experimentally determined phase diagram depends sensitively on the type of micromodels. Chen *et al.* studied the crossover regime from capillary fingering to viscous fingering in a rough fracture micromodel,[107] which was replicated from a granite block. In their study, they injected water to displace silicone oil at different capillaries numbers. The water saturation in the crossover regime is 15% and 25% lower than that in viscous and capillary fingering zones, respectively. The competition between capillary and viscous forces leads to less bifurcation and a higher tip velocity of the invading fluid. Therefore, this regime should be avoided in the real applications.

Wu *et al*. fabricated homogeneous and heterogeneous networks based on Voronoi tessellations.[61] With the existence of large cavities, they found that the permeability is no longer predictable by Kozeny-Carman equation. Instead, a 3D lattice Boltzmann simulation generates really good results. Moreover, they found the presence of cavities largely increased the water-oil displacement efficiency. In another study, Xu *et al.* adopted a similar network generation method and compared the water-oil displacement results with other periodically patterned porous media networks.[63] They found that the existence of cavities decreased the displacement efficiency. And in those periodic networks, the displacement efficiency was reduced with increasing coordinate numbers.

In another study, Xu *et al.* utilized the hydrofluoric acid to isotropically etch glass substrate to fabricate a 2.5D porous medium.[1] By carefully designing a plateau between grooves and accurately controlling the etching time, they were able to etch the plateau into a ridge at a different depth than the grooves. Hence, in their micromodel they have two characteristic depths representing a 2.5D configuration. With such a micromodel, they demonstrated the existence of isolated oil droplet after water flooding in an imbibition scenario as well as the snap-off phenomenon caused by the throat during the emulsion flooding.

Although many researchers fabricated physically heterogeneous micromodels, only a few tried to incorporate chemical heterogeneities, *e.g.* wettability heterogeneity in the micromodels. The reason why people are interested in this problem is that oil reservoir rocks typically contain different types of minerals, which exhibit different wettability. For example, the primary components of reservoir rocks such as quartz, carbonate, and dolomite are water wettable before oil immersion.[108] Although people often think reservoir rocks become oil wettable after immersion, there are portions of the reservoir that remain water wet. According to a study conducted by Treiber *et al*. for carbonate reservoirs, 8% are water wet, 8% are intermediate, and 84% are oil wet. In contrast for silicate reservoir, 43% are water wet, 7% are intermediate, and 50% are oil wet.[109] Therefore, it is also important to study water-oil replacement in reservoirs with heterogeneous wettability.

Traditionally, in the core flooding experiments, people inferred the core based on the amount of oil being pushed out. Some recent studies used x-ray micro-tomography to visualize the oil-water interface inside the core sample and inferred the wettability based on contact angle.

Various factors such as structure, composition, and wettability all influence the results obtained from these top-down methods. However, the appearance of micromodel provided a powerful tool to decouple these effects.

Trojer *et al.* used a radial Hele-Shaw cell packed with glass beads as porous media and studied the displacement of water/glycerol mixture by air.[110] Using chemical vapor deposition of silane, they were able to modify the wettability of glass beads from extremely hydrophilic to moderate hydrophobic. From the experiments, the more wetting the porous medium is, the more stabilized displacement occurs. More specifically, at low *Ca* numbers, the imbibition leads to a compact displacement. At high *Ca* numbers, the finger width expands from single pore to multiple several pores. In all case, the displacement efficiency is increased.

Later Zhao *et al.* improved Trojer's method by using NOA 81 to fabricate 2D pillar based micromodels.[111] The advantage of using NOA 81 is its wettability can be tuned from extremely hydrophilic to extremely hydrophobic. Meanwhile, unlike PDMS, NOA 81 has a much higher modulus which allows it to withstand higher pressure. Therefore they were able to apply water to displace oil in the micromodel. In terms of invading fluid saturation, they found a similar trend as Trojer *et al.* The only difference happened at strong imbibition conditions, where the saturation dropped sharply. By examining the displacing interface, they found that the invading water just moved along the perimeters of the pillars and did not push the oil in pores at all since the porous medium was extremely hydrophilic. Therefore, though imbibition is good for water-oil displacement, strong imbibition results in different outcomes.

Recently, Lee *et al.* developed another method to fabricate porous media with heterogeneous wettability using stop flow lithography in a glass capillary.[94] By using different types of photoinitiator and crosslinker with different ratio, they could modify the pore surfaces with a wide range of wettability. Unlike previous methods that form porous media with uniform wettability, Lee's approach is one of first that is capable of assembling spatially heterogeneous porous media. In their latest work calcite nanoparticles was added in the polymer solution and they could grow a layer of $CaCO_3$ in-situ on the surface of the porous media matrix. Currently, their method still face some challenges such as low throughput (one device per lithography), complicated procedures, indistinguishable surface property after fabrication. But this promising methodology is inexpensive and versatile. Table 2.1 summarizes different methods to modify the wettability of micromodels.

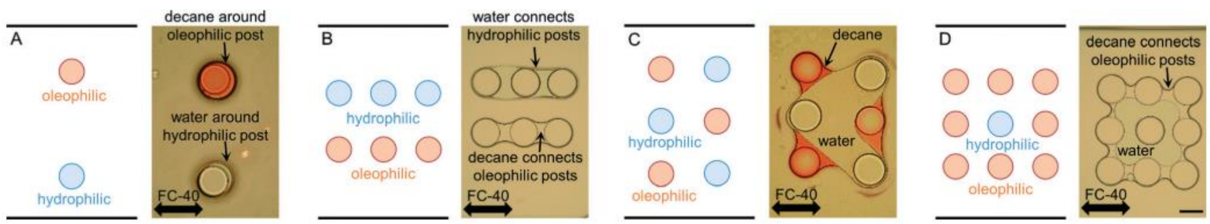

Figure 2.8 Wettability heterogeneous micromodel fabricated by stop flow lithography.[94] Reproduced from [94] with permission from The Royal Society of Chemistry

Table 2.1 Comparison of different methods to modify the wettability of micromodels

Method	Bead mixture in a flow cell	NOA modification	Stop flow lithography
wettability modification	Silane on glass beads	Silane on NOA for hydrophobicity, high energy UV for hydrophilicity.	Different composition of photoinitiator and crosslinker
Major conclusion	1. Visual phase diagram of fluid-fluid displacement as a function of *Ca* number and wettability	1. Wetting film on solid surfaces dominates the fluid-fluid displacement at high *Ca* number	1. Tunable wetting heterogeneity
	2. Stabilization of wettability as system transition from drainage to imbibition	2.Strong imbibition results in dramatic decrease in invading fluid saturation, which is due to the corner flow	2. Tunable spatial wetting heterogeneity
Spatial wetting heterogeneity	No	No	Yes

2.6 Pore scale simulations

In contrast to the relatively scarce pore-scale experiments focused on matrix chemical heterogeneity, numerical modeling of the colloidal behavior under such situations are abundant. Gao *et al.*,[112,113] simulated colloidal transport in a three dimensional homogeneous porous medium composed of 25 beads with Lattice Boltzmann (LB) and Physalis method and Lagrangian particle tracking based on force model. The hydrodynamic interaction, Brownian motion, and physicochemical forces were considered in the colloidal-bead interactions. According to their results, LB is better than the Physalis method in terms of flow field calculation, especially when the domain contains different levels of porosity and grain-grain contact. In their particle tracking simulation, they found all the colloidal deposition occurred at the secondary energy minimum. And hydrodynamic interaction could largely prevent the colloids from moving into the secondary energy minimum.

Pham *et al.*,[114,115] also used LB and Lagrangian method but their colloidal deposition was based on a probability adsorption and desorption mechanism validated by column experiments. In their work they successfully matched their simulation results with macroscopic experiments for a pulse injection of stabilized nanoparticles, as well as analytical solution. Later on they used the same simulation scheme but added surface charge heterogeneities on their porous media. They introduced the heterogeneity by varying the probability of colloidal deposition at certain regimes in the porous medium. With this method, they also studied the influence of different heterogeneity configurations. Their results indicated that the configuration is an important factor for high attachment rate, small particle size, and a balanced amount of favorable and unfavorable deposition sites. What's more, they also found when the Da/Pe is larger than 0.0008, the effect of configuration would become critical.

Johnson *et al.*,[116] also tried to predict colloid retention profiles in glass and quartz porous media with surface charge heterogeneities. Under unfavorable conditions, two types of particle adsorption modes were defined based on their arresting time scales. A fast arresting indicates the particle adsorption is quicker than that under favorable conditions, and a slow arresting means the adsorption takes more time that that under favorable condition. For each arresting time scale, there is a corresponding macroscopic adsorption rate constant. By substituting the fractional summation of the rate constants into the retention equation, it generated a hyper-exponential retention profile that matched the glass beads experimental data very well. For quartz grain porous media, their rough surfaces lead to more grain to grain contact. Consequently, the colloids that approach the surface of a grain have a higher chance to translate to the down-gradient grain upon flushing. Macroscopically, this is reflected by an initial increment in the retention profile and its peak will be pushed further away from the entrance with longer elution. However, because the surface properties of quartz grains are not as well-characterized as the glass beads, the above-mentioned behavior is only described qualitatively.

CHAPTER 3

BEAD-BASED MICROFLUIDIC SEDIMENT ANALOGS: FABRICATION AND COLLOID TRANSPORT

Modified from a paper published in Langmuir[117], Reprinted with permission from American Chemical Society

Yang Guo,[1] Jingwei Huang,[2] Feng Xiao,[2] Xiaolong Yin,[2] Jaehun Chun,[3] Wooyong Um,[3], Keith B. Neeves,[*, 1] and Ning Wu[*, 1]

[1]Department of Chemical and Biological Engineering, Colorado School of Mines, Golden Colorado 80401, United States

[2]Department of Petroleum Engineering, Colorado School of Mines, Golden Colorado 80401, United States

[3]Pacific Northwest National Laboratory, 902 Battelle Boulevard, Richland, Washington 99352, United States

[*]Corresponding author

3.1 Abstract

Mobile colloids can act as carriers for low- solubility contaminants in the environment. However, the dominant mechanism for this colloid-facilitated transport of chemicals is unclear. Therefore, we developed a bead-based microfluidic platform of sediment analogues and measured both single and population transport of model colloids. The porous medium is assembled through a bead-by-bead injection method. This approach has the versatility to build both electrostatically homogeneous and heterogeneous media at the pore scale. A T-junction at the exit also allowed for encapsulation and enumeration of colloids effluent at single particle resolution to give population dynamics. Tortuosity calculated from pore-scale trajectory analysis

and its comparison with lattice Boltzmann simulations revealed that transport of colloids was influenced by the size exclusion effect. The porous media packed by positively and negatively charged beads into two layers showed distinctive colloidal particle retention and significant remobilization and re-adsorption of particles during water flushing. We demonstrated the potential of our method to fabricate porous media with surface heterogeneities at the pore scale. With both single and population dynamics measurement, our platform has the potential to connect pore-scale and macroscale colloid transport on a lab scale and to quantify the impact of grain surface heterogeneities that are natural in the subsurface environment.

3.2 Introduction

The application of micromodel on colloidal particles transport study rose with the maturing of photolithography and etching technology. With this method, the pore networks of these models may consist of periodic features such as arrays of polygons,[60] random networks with statistically similar porosities and permeabilities of real rocks,[61] or replicas of real rock pore spaces based on imaging data.[62] All these replicates give a continuous solid phase and a series of interconnected channels that provides good imitation of the pore space of many resource-rich rocks in deep underground. But contaminants that are of most concern to human health usually reside the shallower subsurface where soils are the dominating media as unconsolidated, rough, spherical, and micrometer- to millimeter-sized grains. As such, bead-based or post-based micromodels are potentially a better model for measuring colloid transport in soils.[69] For example, the influence of colloid size on dispersion has been measured in polydimethylsioxane (PDMS) and silicon pillar based micromodels.[66,67] Studies in a glass-bead micromodel show that rod-shaped colloids are more likely to attach to the beads than spherical ones due to local charge heterogeneity and surface roughness.[118] In unsaturated porous media, bead-based micromodel show that the adsorption of colloids at air-liquid interfaces as a function of their wetting properties, surface charge, and the ionic strength of the solution.[8,99,119] In these micromodel studies, individual colloid trajectories and adsorption kinetics were observed, but the average transport properties of a large population of colloids were not collected. This is possibly due to the challenge of collecting and analyzing the effluent of micromodel since the total volumes are on the order of nano- to micro-liters. An important property of natural soils is the heterogeneity of interfacial properties between grains.[8] Yet, unlike the bead-based proteomics and genotyping methods,[120–122] the existing work has not fully exploited a distinct advantage of the beads-based soil analogs, namely each bead can have its own interfacial properties.

To address the shortcomings described above, we developed a bead-by-bead assembly platform to fabricate soil analogs. By integrating a T-junction droplet generator into the device, we encapsulated and enumerated the effluent in microliter scale to obtain the average transport behavior of a population of colloids. Using the same device we also measured the individual trajectories of colloids by optical microscopy. Simulations of fluid and solute transport based on the Lattice Boltzmann Method (LBM) were performed on digitally reconstructed replicas of the soil analog to aid in the interpretation of the experimental results. The measured pore scale dynamics of colloid transport such as trajectory lengths were in good agreement with simulations for small particles in ionic solutions, while larger particles showed size exclusion effects that are not considered in numerical simulations. Finally, we demonstrate the profound impact of heterogeneous interfacial properties on colloid transport with an analog consisting of beads with positive and negative surface charges.

3.3 Materials and Methods

3.3.1 Materials

Polydimethylsioxane (PDMS) was from Dow Corning (Sylgard 184, Midland, MI). Mineral oil and cyclopentanone (≥99%) was from Sigma Aldrich (St Louis, MO). 1H-1H-2H-2H-perfluorooctyltrichlorosilane was from Gelest (Morrisville PA). Photoresist (KMPR1010 and KMPR1050) was from MicroChem (Newton, MA). Developer (AZ300 MIF) was from AZ Electronic Materials (Somerville, NJ). 0.5 µm carboxylated yellow-green (505/515) colloids, 1 µm sulfate yellow-green (505/515), 15 µm blue (365/415), 10 µm crimson (625/645) fluorescent polystyrene (PS) microspheres and 10 µm aliphatic amine latex beads were from Life Technologies (Carlsbad, CA). 3 µm carboxylated yellow-green (480/501) fluorescent PS microspheres were from Magsphere Inc. (Pasadena, CA). Three-inch silicon wafers were from Silicon Inc. (Boise, ID). Gauge 30 Tygon tubing was from Saint-Gobain North America (ID = 0.01”, OD = 0.03”, Valley Forge, PA). Biopsy punch (0.75 mm) was from World Precision Instrument (Sarasota, FL).

3.3.2 Device fabrication

Microfluidic channels were defined in PDMS using standard soft lithography techniques.[123] A two-layer photolithography procedure was used to create channels with two different heights on the master. For the first layer, KMPR1010 was spin coated at 3000 rpm for 40 sec, soft baked for 6 min at 100ºC, exposed through a photomask (CAD/Art service, Bandon, Oregon) to UV light (200 W, 365–405 nm exposure) in a Karl Suss MJB-3 Mask Aligner (Sunnyvale, CA) at a dose of 10 mW/cm^2, and hard baked for 2 min at 100ºC. For the second layer, KMPR 1050 was diluted to 40 wt% solids in cyclopentanone and spun at 4000 rpm for 40 sec. The same soft bake, exposure, and hard bake procedures were followed. The photoresist master was made hydrophobic by incubation with 1H-1H-2H-2H-perfluorooctyltrichlorosilane for 24 h under vacuum. To make the microfluidic device, PDMS (5:1 polymer vs. curing agent in mass) was poured over the master and cured for 4 h at 80 ℃. The devices were then peeled off from the master and plasma bonded on a glass slide. Both the inlet and outlet holes were made with 0.75 mm punch.

3.3.3 Device operation

Fig. 3.1 shows a schematic of the device. It was operated in two modes: the bead filling and colloid transport mode. In the bead filling mode, a dilute suspension (5×10^5/ml) of 15 µm beads was introduced through inlet *a*. All other inlets and outlets except *e* were blocked. The beads were trapped at barrier *d*, where the channel height is reduced from 21 µm to 12 µm. As beads were trapped, they formed a porous medium that grew upstream.

For the layered packing of carboxyl- and amine-functionalized beads in the chemically heterogeneous soil analog, we injected them sequentially. Note that the channel height was slightly larger than the diameter of the beads. Therefore, the beads packed pseudo-two-dimensionally into a porous soil analog that was 840 µm in width, 21 µm in height, and 500–2000 µm in length. In the colloid transport mode, suspensions of fluorescent colloids (0.5, 1, and 3 µm) were injected through inlet *b*. Since the pore volume was small (~10 nL), collecting fluid from the outlet of the device was not feasible when trying to measure the transient in colloid breakthrough. Instead, we placed a T-junction droplet generator downstream at position *f* to encapsulate the effluent colloids. DI water entered from inlet *c* to stabilize droplet generation before colloids entered. Mineral oil was injected from inlet *e* and used as the continuous phase. The aqueous solution emanating from the soil analog is the dispersed phase.

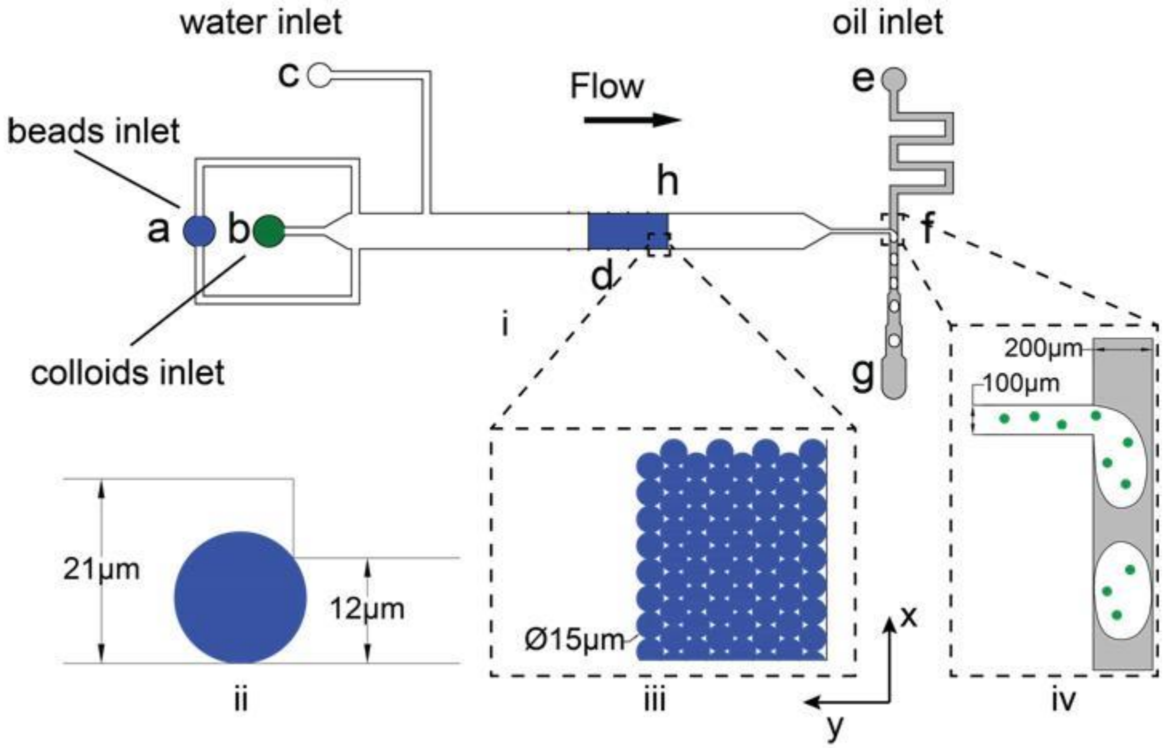

Figure 3.1 Configuration of the microfluidic device designed for building the soil analog and studying *in situ* colloidal transport. (i) The top view; *a* and *b* are the inlets for flowing PS beads and small colloids into the device; *c* is the inlet for DI water used to wet the fabricated porous medium when we switch from the bead-filling mode to colloid-transport mode; *d* represents the height barrier (e.g., 10µm) where large (e.g., 15 µm) PS beads are trapped and packed into the soil analog; *e* is the inlet for mineral oil; *f* is the T-junction where the colloidal solution passing through the soil analog forms individual droplets in the oil phase; *g* is a gradually expanded channel that slows down the droplet flow, which facilitates counting the number of colloids in each droplet. (ii) The side view of the height barrier *h*. (iii) Schematics of the bead-based soil analog. (iv) The T-junction, where the gray indicates mineral oil, and the white droplets represent colloidal solution that passes through the porous medium. Green dots inside the droplet represent fluorescent colloids.

For capillary numbers $Ca < 0.01$ ($Ca = \mu U / \gamma$, where μ is dynamic viscosity, U is velocity, and γ is interfacial tension), the dispersed phase forms into droplets, where individual colloids are encapsulated.[124–126] The droplet size depends on the flow rates of two phases and the channel sizes, *i.e.*, $L/W = 1 + \alpha Q_{in}/Q_{out}$, where L is the length of droplet slug, W is the width of the channel, Q_{in} and Q_{out} are the flow rates of the dispersed and continuous phases, and α is an order one constant.[24] We adjusted the oil flow rates to control the droplet diameter at around 300 μm. Downstream of the T-junction the channel was expanded from 200 μm to 400 μm to reduce the droplet velocity allowing for real-time imaging. By taking both fluorescent and bright-field images, the number of colloids in each droplet and droplet volumes were measured.

For the layered packing of carboxyl- and amine-functionalized beads in the chemically heterogeneous soil analog, we injected them sequentially. Note that the channel height was slightly larger than the diameter of the beads. Therefore, the beads packed pseudo-two-dimensionally into a porous soil analog that was 840 μm in width, 21 μm in height, and 500–2000 μm in length. In the colloid transport mode, suspensions of fluorescent colloids (0.5, 1, and 3 μm) were injected through inlet *b*. Since the pore volume was small (~10 nL), collecting fluid from the outlet of the device was not feasible when trying to measure the transient in colloid breakthrough. Instead, we placed a T-junction droplet generator downstream at position *f* to encapsulate the effluent colloids. DI water entered from inlet *c* to stabilize droplet generation before colloids entered. Mineral oil was injected from inlet *e* and used as the continuous phase. The aqueous solution emanating from the soil analog is the dispersed phase. For capillary numbers $Ca < 0.01$ ($Ca = \mu U / \gamma$, where μ is dynamic viscosity, U is velocity, and γ is interfacial tension), the dispersed phase forms into droplets, where individual colloids are encapsulated.[124–126] The droplet size depends on the flow rates of two phases and the channel sizes, *i.e.*, $L/W = 1 + \alpha Q_{in}/Q_{out}$, where L is the length of droplet slug, W is the width of the channel, Q_{in} and Q_{out} are the flow rates of the dispersed and continuous phases, and α is an order one constant.[24] We adjusted the oil flow rates to control the droplet diameter at around 300 μm. Downstream of the T-junction the channel was expanded from 200 μm to 400 μm to reduce the droplet velocity allowing for real-time imaging. By taking both fluorescent and bright-field images, the number of colloids in each droplet and droplet volumes were measured.

3.3.4 Identification of bead location

The positions of individual beads in the soil analog were determined by stitching a series of images together using a 20X objective (field of view = 440 μm × 325 μm) on an inverted microscope (IX81, Olympus) with a 16-bit CCD camera (ORCA-R2, Hamamatsu). For a 1000 μm long soil analog, 15 images were stitched together using the ImageJ macro stitching.[127] A custom MATLAB script identified the *x* and *y* coordinates of the center of each bead using the following steps: (i) a Canny algorithm[128] located the edge of each bead; (ii) a first filtration operation eliminated any debris or imaging artifacts with a circumference larger than 51 μm; (iii) features remaining after filtration were filled and a second filtration operation eliminated debris or imaging artifacts with areas less than 31 μm^2 or larger than 104 μm^2; (iv) a third filtration operation eliminated debris or imaging artifacts with circularity larger than 0.9. Circularity is defined as $P^2/4\pi A$, where P is the perimeter and A is the object area,[129] and (v) the *imfindcircles* command identified the coordinates of the center of each bead. For the heterogeneous bead packing, one extra step was added before we run the Canny algorithm. Since we have two different types of beads, the *polycrop* command was used to define the region of interest for the carboxyl-functionalized beads first. The area of other beads was then filled with black pixels. This operation kept the beads at the same location in the original image. We run the image processing program for each section of beads first and then combined them to obtain the center positions of all beads in the whole porous medium.

3.3.5 Measurement of hydraulic permeability

A reservoir of deionized water was connected to inlet *b* of the device with 30 gauge tubing and raised 20–60 cm above the device to establish the inlet pressure head. The device for permeability measurements was similar to that in Fig. 1, but without the droplet generator.The outlet channel *f'* was connected to 30 gauge tubing placed at the height of the device and open to the atmospheric pressure. The linear velocity of water was measured by tracking the meniscus in the outlet tubing for 1 minute. It was then converted to a volumetric flow rate Q using the cross-sectional area of the tubing. Each pressure drop, ΔP, was repeated in triplicate. The total hydraulic resistance of the device, R, was calculated by $R=\Delta P / Q$. The total resistance includes the resistance of tubing R_t, the pre/post-analog channel R_c, and the soil analog R_p connected in series. R_t, and R_c were calculated by:[130]

$$R_t = \frac{8\mu L_t}{\pi r^4} \tag{2.22}$$

$$R_c = \frac{12\mu L_c}{W_c H_c^{\,3}\left(1-0.63 H_c / W_c\right)} \tag{2.23}$$

where L_t and r are the length and radius of the tubing, respectively. L_c, W_c, and H_c are the length, width, and height of the pre/post-analog channel. By subtracting R_t and R_c from the total resistance R, we can obtain the resistance of the soil analog R_p, which is related to the permeability κ by

$$\kappa = \frac{\mu L_p}{W_p H_p R_p} \tag{2.24}$$

where L_p, W_p, and H_p are the length, width, and height of the analog.

3.3.6 Measurement of the colloidal particles population dynamics

The zeta potentials of the colloids were measured using ZetaPALS (Holtsville, Brookhaven Instruments Corporation, NY). Suspensions of colloids in DI water were injected at a flowrate of 1 nL/sec through inlet *b* (Fig. 1). Mineral oil was injected into the oil inlet *e* at a flowrate of 1.6 nL/sec. The colloids emanating from the soil analog were emulsified at the T-junction. Due to the expansion in channel width at *g*, the droplet flow velocity was reduced by half and images of individual droplets were taken in both fluorescent and bright-field modes. A custom MATLAB script was used to enumerate the number of colloids in each droplet using the following procedure: (i) the *im2bw* command turned the gray scale image to black and white, and a contrast threshold is set to ensure all the fluorescent particle turned to white dots, (ii) the *bwboundaries* command detected the edge of each white dot and counted their total number.

3.3.7 Trajectory of individual colloids and calculation of tortuosity

At a volumetric flow rate of 1 nL/sec, the trajectories of 0.5, 1, or 3 µm colloids were measured by epifluorescence microscopy (20X, NA 0.45) with an exposure time of 500 ms. These imaging conditions yielded pathlines whose lengths were measured to calculate tortuosity. The diffusion coefficient of the colloids was calculated using the Stokes-Einstein equation: $D = k_B T / 6\pi\mu a$, where k_B is the Boltzmann constant; T is absolute temperature; and a is the radius of the spherical particle. The Peclet number was defined based on a length scale of porous medium as $Pe = dU/D$, where d is the characteristic length of the porous medium (i.e., the bead diameter); U is the superficial velocity of the fluid; and D is the colloid diffusion coefficient. The tortuosity was defined by $\tau = L_a / L_e$, where L_a and L_e are the arc-length and end-to-end distance of the trajectory.

3.3.8 Colloids retention on chemically heterogeneous soil analog

The chemically heterogeneous soil analog was assembled from two types of 10 µm beads functionalized with carboxyl and amine groups, respectively. We arranged their packing in two ways. The aliphatic amine beads first packed into a 500×840 (L×W) μm^2 rectangular layer, followed by another layer of carboxylated beads with 500×840 μm^2, and vice versa. After the soil analog was formed, 1 µm colloids at the concentration of 0.054 mg/mL were introduced at 2 nL/s for 2 hours and followed by DI water flush at the same rate for another 2 hours. During the experiment, both fluorescence and bright-field images were taken. A custom MATLAB script was used to calculate the mean fluorescence intensities at specific regimes over time. For a 16-bit grayscale image, each pixel was associated with a value from 0 to 65535 based on its brightness (0 is the darkest and 65535 is the brightest). For each fluorescence image, we added all pixel intensities over the region occupied by one specific type of beads and then divided by its area. In this way we obtained the mean fluorescence intensity per unit area.

3.4 Results and discussion

3.4.1 Characterization of the porous medium

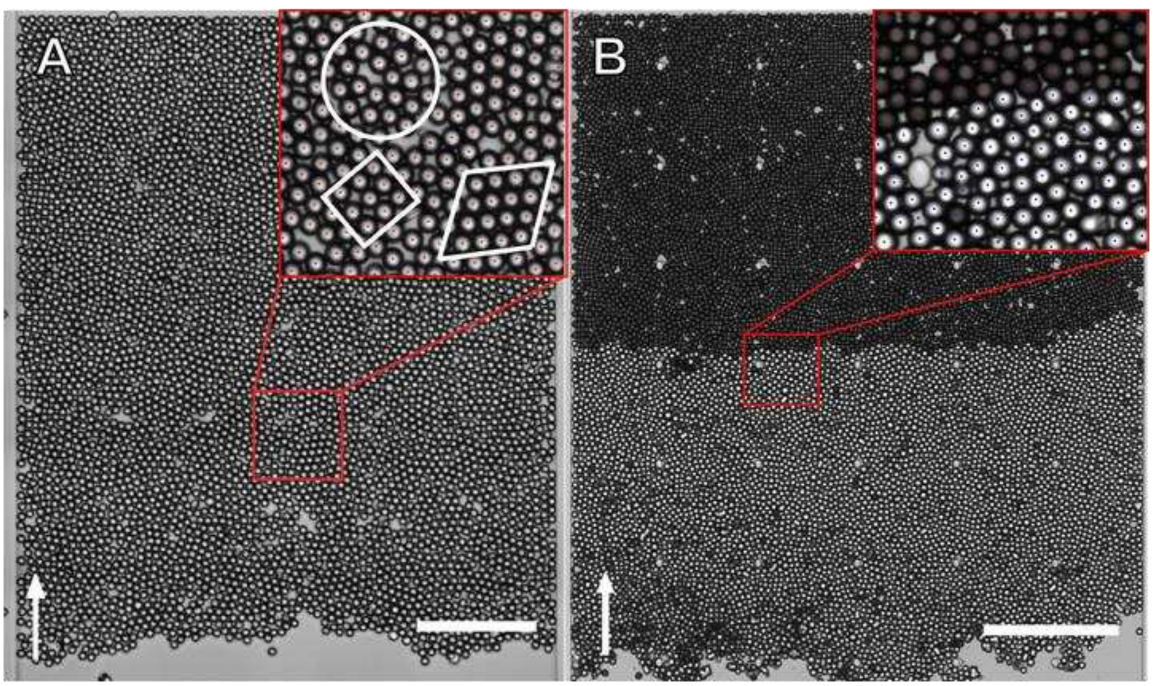

Figure 3.2 The porous soil analog formed by trapping (A) 15 µm PS beads in a rectangular channel (1030 µm × 840 µm × 21 µm) and (B) a binary mixture of 10 µm PS beads in another channel (990 µm × 840 µm × 15.5 µm). The arrows indicate the flow direction. For (A), the white frames in the inset highlight the hexagonal, square, and irregular packing of beads locally. The red dots indicate the center of each bead detected by image processing. For (B), carboxylated crimson beads (darker ones) are introduced first and followed with aliphatic aminated beads (brighter ones). Scale bar for both images: 200 µm.

Polystyrene beads were introduced into the device through inlet *a* and trapped by the height barrier *h* (Fig. 3.1). Fig. 3.2A displays a soil analog homogeneously packed by 15 µm PS beads. As shown by the inset of Fig. 3.2A, there were three types of sphere-packing: hexagonal array, square lattice, and irregular arrangement with voids, all of which have been observed in real soil sediments.[131]

One of the advantages of the bead-based microfluidic soil analogs is that one can conveniently introduce beads with different types of chemical properties in the same channel. The resulted porous medium will possess chemical heterogeneities at the pore scales. As a proof of concept, we sequentially injected 10 µm carboxyl- and amine-functionalized beads to form a bilayer soil analog shown in Fig. 3.2B. Since these beads have opposite charges (-40.0 ± 4.9 mV for carboxylated and 21.2 ± 4.8 mV for amine aliphatic beads, respectively) in DI water, the resulting soil analog mimics soil layers with different surface charges. Although all particles have the same diameters, the carboxylated and amine coated beads can be distinguishable under bright-field microscopy because the additional fluorophores on the carboxylated beads tend to absorb more light (Fig. 3.2B) giving a darker appearance. Table 3.1 summarizes all relevant characteristics of the fabricated homogeneous and heterogeneous soil analogs.

Table 3.1 Characteristics of the fabricated soil analogs and fluid and colloid transport properties

Soil analog type	homogeneous	heterogeneous
porous medium dimension (μm^3)	1030×840×21	985×840×15.5
number of packed beads	4669	10771
porosity	0.56	0.57
pore volume (nL)	11.2	7.4
colloid size (µm)	1 ± 0.031	1 ± 0.031
zeta potential of colloids that flow through(mV)	-60.4 ± 2.5	-23.1 ± 4.7
flow rate (nL/sec)	1	2
superficial linear velocity (µm/sec)	93	269
colloidal diffusivity (μm^2/sec)	0.429	0.429
Peclet number	3200	6171

A key feature of a transparent soil analog compared to columns is that we can measure the position of each bead and then digitally reconstruct the entire porous medium used in experiments. This allows us to faithfully compare the pore-scale numerical calculations of fluid flow and colloidal transport with experiments. The image processing routine correctly identified 99% of soil analogs filled with 4000-10,000 beads. Since the bead diameter (15 μm for the homogeneous soil analog) is less than the chamber height (21 μm), not all beads are located at the same vertical position. However, it was difficult to determine the vertical positions of each bead by optical microscopy. Therefore, we used our LBM simulations to determine the impact of bead vertical position on fluid flow. A series of simulations were performed whereby we randomly displaced a percentage of beads in the z-direction from being in contact with the bottom of the chamber to being in contact with the top. Fig. 3.3 shows the cross-sectional and perspective views when 0%, 25%, and 50% of the beads were displaced.

The hydraulic permeability is an intrinsic property of porous media that characterizes macroscopic fluid transport. We calculated the permeability by measuring the hydraulic resistance in the entire device and subtracting the resistances of the other components. Supplemental Table 1 lists the contribution of all individual components to the total resistance in a typical measurement. The highest resistance is through the soil analog, however other resistances are significant (~30%) and cannot be ignored. Fig. 3.4 summarizes the experimentally measured and numerically simulated permeabilities of soil analogs with lengths of 500, 1000, and 1500 μm.

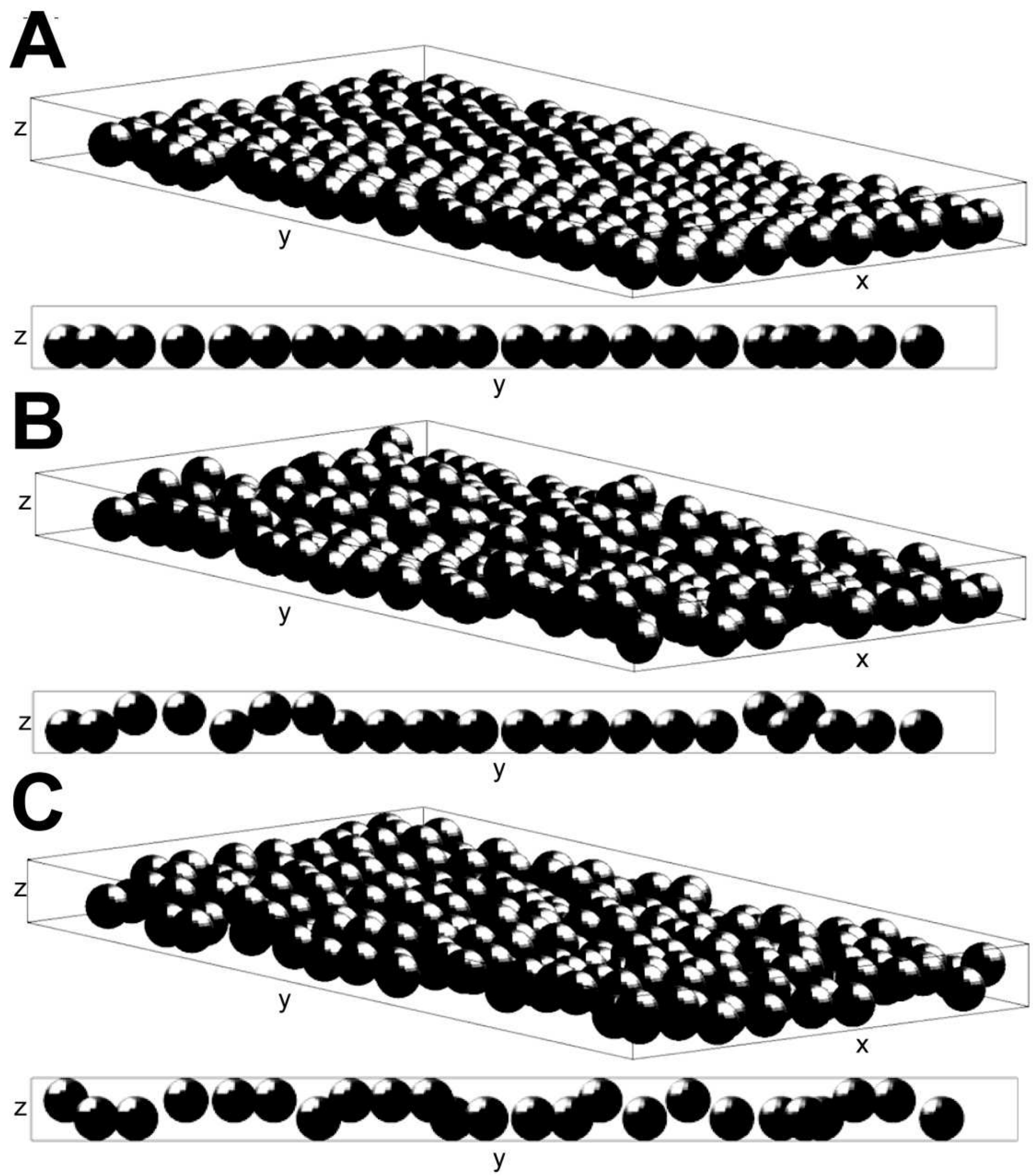

Figure 3.3 The cross-sectional and perspective views of the porous medium with 0%, 25%, and 50% bead displaced to the top of the chamber and the balance in contact with the bottom of the chamber. The x-y positions of each bead were digitally reconstructed from experiments. These geometries are used in the LBM and RWPT simulations.

As expected from an intrinsic property, the experimentally measured permeability is independent of the length of the porous media. The low variance in the permeability measurement suggests that the average hydraulic resistance between different soil analog preparations is reproducible, even as the exact positions of beads change. The calculated permeabilities from LBM simulations show a significant influence on the vertical positions of beads. When all beads were in contact with the bottom of the chamber, the predicted permeability was two-fold larger than the experimental results. This large difference is primarily due to the low-resistance zone formed by the 6μm gap between the beads and top of the chamber. In essence, fluid can bypass the beads by flowing through the top of the channel. In comparison, the calculated permeability when 50% of the beads were in contact with the top of the chamber is in good agreement with experimental results.

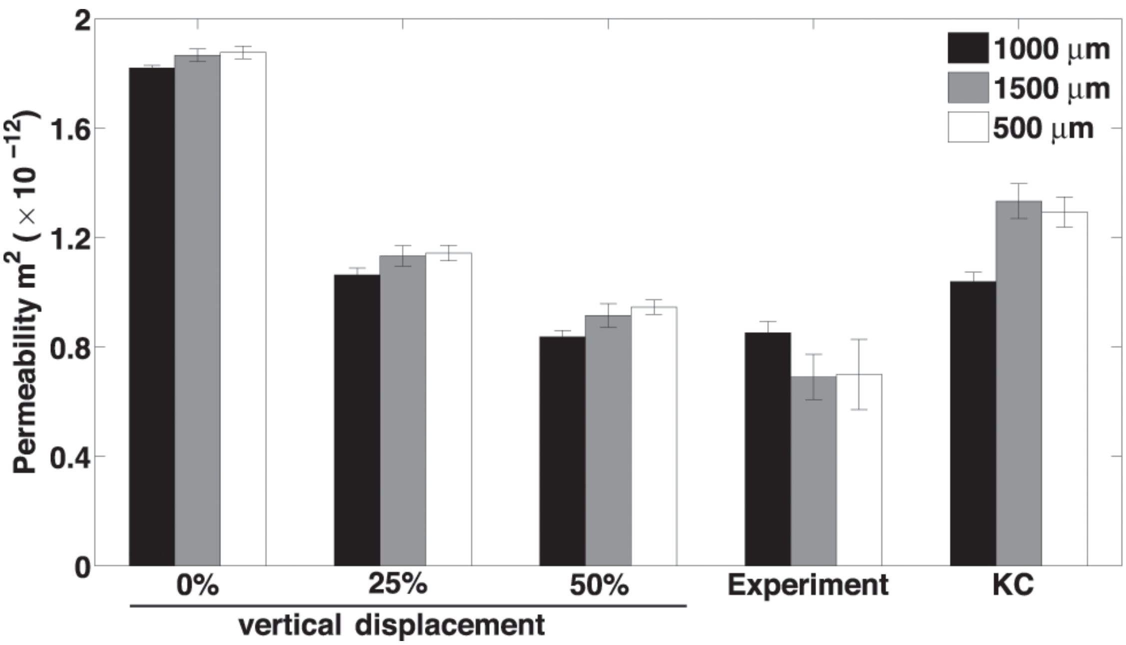

Figure 3.4 Numerical simulation with 0, 25, and 50% vertical displacement of beads, experimental measurement, and calculation using the Kozeny-Carmen (KC) equation (eq. 4) of the permeabilities of soil analogs with three different lengths (500, 1000, and 1500 μm). The error bars represent the standard deviations of three replicas.

We also calculated the permeability using the semi-empirical Kozeny-Carman (KC) equation[132]

$$\kappa = \frac{d^2}{180} \frac{\phi^3}{(1-\phi)^2} \tag{2.25}$$

where d is the bead diameter and ϕ is the porosity. The Kozeny-Carman equation predicts a higher permeability than the measured values, possibly because it does not account for the pseudo-two-dimensional packing of beads in our soil analog.

3.4.2 Macro- and microscopic transport of colloids

We used a colloid flow-through curve to quantify the population dynamics of colloids transporting through the soil analog. The flow-through curve is defined as the concentration of colloids emanating from the porous media as a function of pore volume. Owing to the small volumes perfused through our microfluidic porous media, it is difficult to make an off-chip concentration measurement of colloids at the temporal resolution needed to measure the transient portion of the flow-through curve. Therefore, we incorporated a T-junction droplet generator downstream of the porous medium where the effluent colloidal solution was emulsified into individual droplets in a continuous stream of mineral oil. This feature allowed us to generate a colloid flow-through curve at single colloid resolution.

Fig. 3.5A shows the overlay of bright-field and fluorescent images in the expansion channel (*g* in Fig. 3.1). The volume of each droplet and the number of colloids per drop was used to generate a flow-through curve of an injection of more than 2000 colloids (Fig. 3.5B). The colloidal concentration was normalized by its inlet concentration. The concentration reached steady-state after about ten pore volumes (~100 nL).

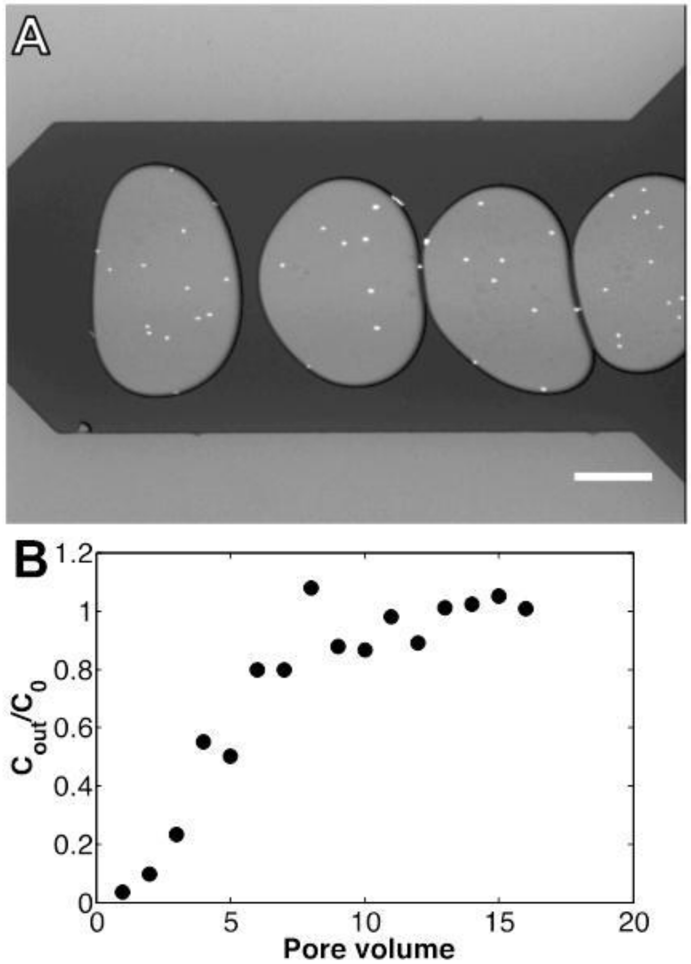

Figure 3.5 Colloidal breakthrough curve. (A) Overlay of bright field and fluorescent images where the colloid suspension (light grey) exiting the soil analog is emulsified into droplets in a continuous stream of mineral oil (dark grey). The bright dots are 1 µm fluorescent colloids encapsulated in the droplets. Scale bar = 100 µm. (B) Measured flow-through curve of 5.4 × 10-3 wt% 1 µm colloidal suspension passing through a soil analog with a pore volume of 10 nL.

Measurements of microscopic colloid transport at the pore scale are inaccessible by imaging techniques in column experiments. This limitation partially motivates the need for our microfluidic soil analog where the real-time transport of colloids can be captured by optical microscopy. We measured the trajectories of colloids sized 0.5, 1, and 3 µm using exposure times that produce pathlines (Fig. 3.6).

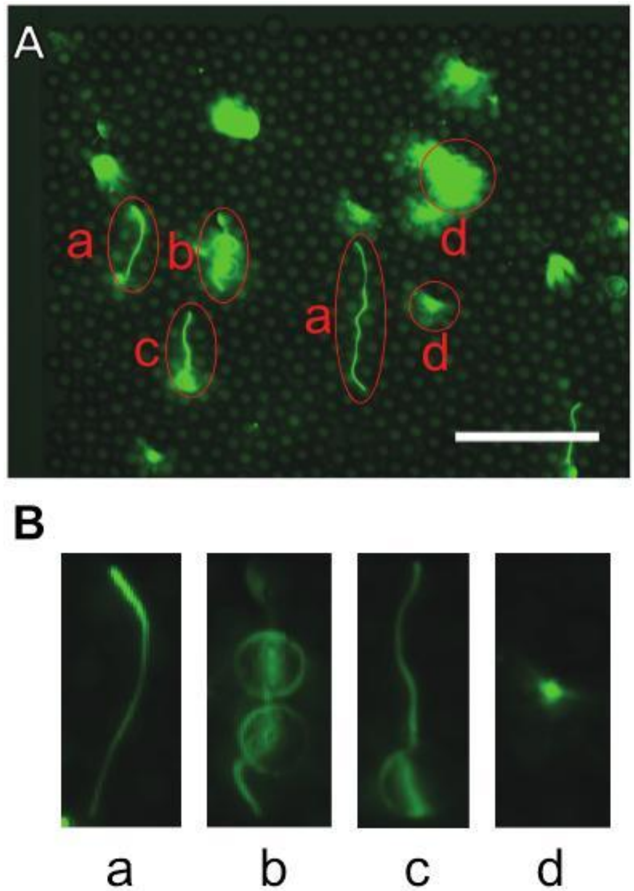

Figure 3.6 The trajectories of individual colloids in the soil analog. (A) *a* is the trajectory of colloids that flow below the equator of the beads; *b* is the trajectory of colloids that flow above the equator of the beads; *c* is the trajectory of colloids that flow from top to bottom or bottom to top of the beads; and *d* are colloids that are immobilized. Scale bar: 100 μm. (B) Zoom-in images of four types of trajectories, where the contrast was adjusted to reveal the trajectories more clearly.

The diffusion coefficients for 0.5, 1, and 3 μm colloids were estimated with the Stokes-Einstein equation as 8.6×10^{-13}, 4.3×10^{-13}, and 1.4×10^{-13} m^2/s, respectively. With a fluid linear velocity of 94 μm/s, these colloids have Peclet numbers of 1600, 3200, and 9600. Zeta potentials for them in deionized (DI) water and 0.5 μm colloids in 0.1M NaCl solution were measured as -74.2 ± 3.9, -60.4 ± 2.5, -44.6 ± 2.3, and -58.9 ± 5.0 mV. Fig. 6 shows four types of trajectories observed: (a) colloids that flow between the beads and the bottom of the channel appear as sharp and continuous lines; (b) colloids that flow above the beads appear blurred due to scattering of emitted light; (c) colloids that flow from above the beads to below, or vice versa; and (d) colloids that are immobilized appear as bright aggregated spots. Table 2 shows the mean trajectory length for 0.5, 1, and 3 μm colloids in DI water and 0.5 μm colloids in 0.1 M NaCl, the corresponding mean velocities are 88, 117, 117, and 86.2 μm/s, respectively. The superficial velocity of the fluid is 94 μm/s. Larger colloids move faster than the average fluid velocity because of the size exclusion effect; they cannot approach solid boundaries as closely as smaller particles and consequently are biased towards higher velocity regions of the flow profile.[66]

Table 3.2 Average values of pathline length and tortuosity measured in four different colloidal flow conditions

Conditions	0.5 μm in DI water	1 μm in DI water	3 μm in DI water	0.5 μm in 0.1M NaCl water
length (μm)	44.0 ± 22.7	58.5 ± 26.9	58.5 ± 23.5	43.1 ± 22.9
tortuosity	1.171 ± 0.078	1.172 ± 0.079	1.161 ± 0.061	1.175 ± 0.091

Based on the trajectories, we also determined the effects of colloid size and salt concentration on the tortuosity of colloid transport. Fig. 3.7 shows the tortuosity distribution of differently sized colloids suspended in DI water and 0.5 μm colloids suspended in 0.1 M NaCl. Their mean values and the associated standard deviation are summarized in Table 3.2. For comparison, the predicted tortuosity distribution of point particles in LBM simulations is also shown. The distributions are non-Gaussian, but the mode for all colloids falls within 1.1–1.15 tortuosity. However, the variance in tortuosity is lower for 3 μm colloids, indicative of the size exclusion effect where larger colloids sample a smaller volume of the pore space than smaller ones. Furthermore, the tortuosity distribution for 0.5 μm colloids in a 0.1 M NaCl solution most closely matched the point particles in LBM simulation. These results reflect the influence of size exclusion and electric double layer suppression in high ionic strength solution.

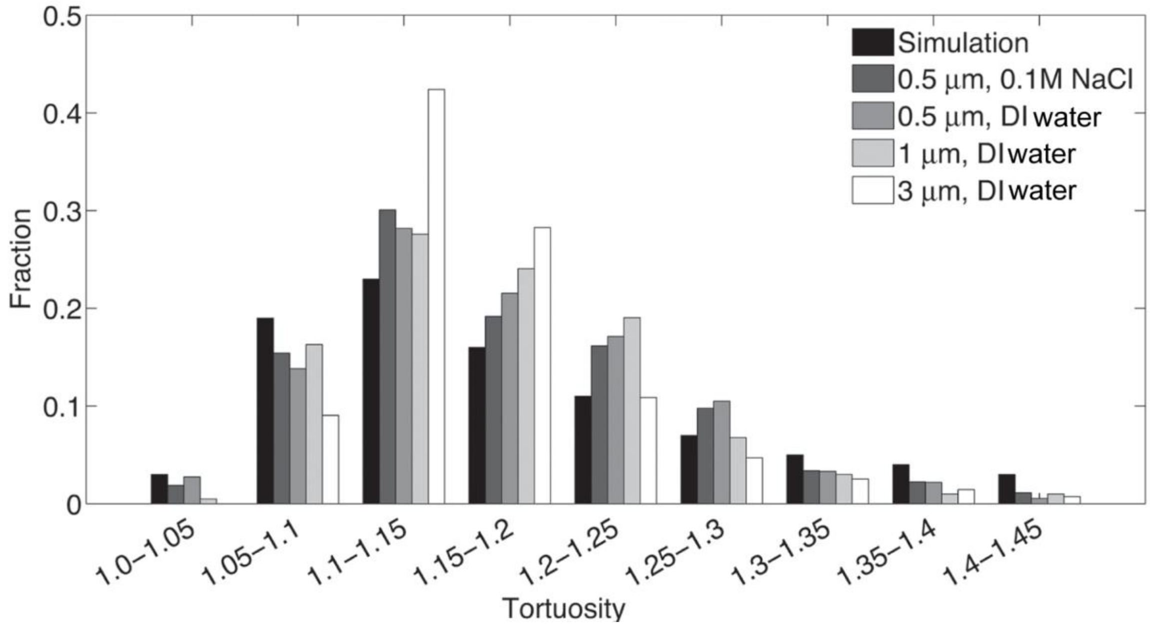

Figure 3.7 The distribution of tortuosity for colloids of different sizes in water.

3.4.3 Retention of colloids in heterogeneous soil analogs

Real soils are often layered with physical and chemical heterogeneities, although generally soil is negatively charged. However, under low pH condition, they can turn into positively charged.[133] As a proof of concept, we fabricated bi-layered soil analog that was packed by carboxyl- and amine-functionalized beads, respectively. Fig. 3.2B shows that the carboxylated beads are located at the downstream. The measured zeta potentials of carboxylated and aminated beads are -40.0 ± 4.9 and 21.2 ± 4.8 mV, respectively, and thus they will have different electrostatic interactions with the negatively charged colloids (e.g., 1µm and -23mV). Fig. 3.8 shows the average fluorescent intensities of retained colloids within the carboxylated and aminated layers. As expected, the positively charged (aminated) beads retained more colloids than the negatively charged (carboxylated) beads in both configurations.

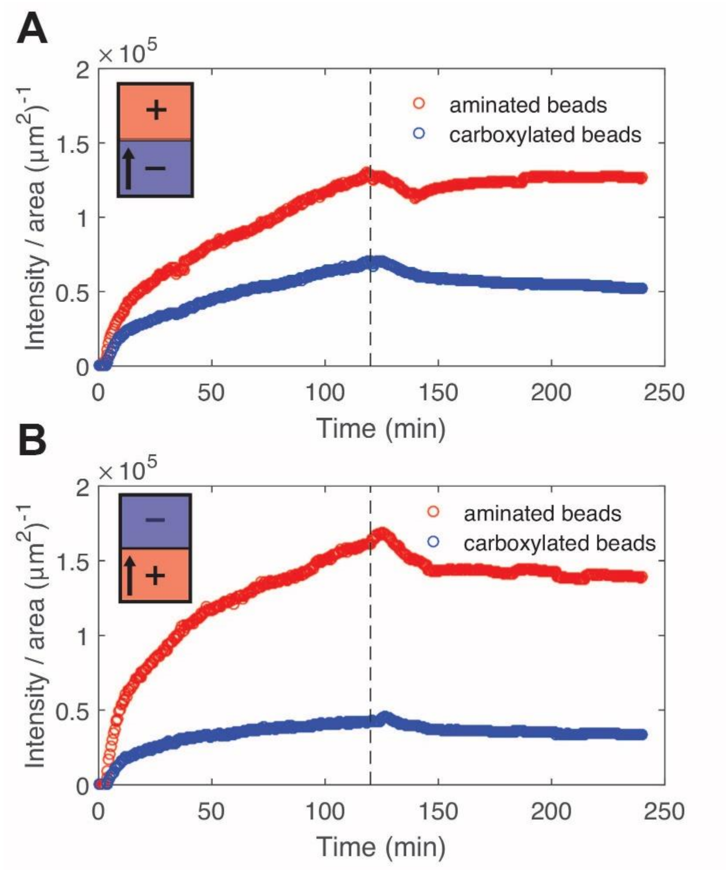

Figure 3.8 Colloids retention in two different types of layered soil analogs. The fluorescent intensities of colloids retained in the soil analog where the carboxylated beads are packed (A) upstream and (B) downstream. The insets on the top left corner illustrate the analog configuration .The circles represent the colloids accumulated in the aminated bead packing and the squares are for the carboxylated bead packing. The dash line indicates the moment when we stopped injecting colloid solution and start to flush with DI water containing no colloids.

During the DI water flush some colloids detached from the beads, which cause the intensities in both types of bead packing to decrease first. This indicates that some of the colloidal attachment in the porous media can be metastable. In Fig. 3.8A, where the carboxylated beads were located upstream, the intensity within the aminated bead packing increased while it decreased in the carboxylated bead packing. This observation is due to the re-adsorption of colloids in the aminated bead packing that were removed from the carboxylated bead packing. In the opposite configuration (Fig. 3.8B), re-adsorption of colloids in the downstream carboxylated bead packing was minimal since the colloid-bead electrostatic interactions are repulsive. As a result, the fluorescent intensity remains constant at later stage of DI flushing (Fig. 3.8B). The detachment-reattachment of colloids observed in certain types of layered soil analogs can have important implications to colloidal transport in the subsurface environments. First, it would delay the transport of colloids even in the event of multiple flushing due to the differently charged soil surfaces. Second, instead of dilution, the flushing could cause the contaminants to concentrate at locations where colloidal adsorption is energetically favorable. Supplemental video 4 shows the detachment-reattachment process at certain beads section.

3.5 Conclusion

We developed a microfluidic bead-based platform that can make soil analogs consisting of model grains with homogeneous or heterogeneous surface properties. We measured the transport of both individual and populations of colloids in these soil analogs. Using the pathlines of individual colloids flowing through the pseudo-two-dimensional bead pack, we were able to extract the tortuosity of differently sized colloids and measure the effects of size exclusion and double layer suppression. The T-junction droplet generator allowed us to measure the transport of thousands of colloids in a single experiment and generate flow-through curves. By demonstrating the capability to make heterogeneous soil analogs in this paper, we expect our approach can be used in future to study colloidal transport in porous media with different types of surface heterogeneities (e.g., charge, wettability, and chemical functionality) at the pore scale. Important insights into the colloid-soil interactions and colloidal transport and retention could also be obtained by direct comparison of the results obtained from the microscale soil analogs and larger scale column experiments.

3.6 Acknowldgement

This work is supported by the Department of Energy NEUP program under the award DE-NE0000719 and National Science Foundation CAREER award (CBET-1351672, KN). The authors thank Drs. Ning Wu, Keith Neeves, Aditya Kasukurti, Sijia Wang, Adam Wufsus, Joanna Sylman, Kuldeepsinh Rana, and Marcus Lehmann for technical assistance.

CHAPTER 4

COLLOIDAL TRANSPORT IN MICROSCOPIC POROUS MEDIUM ANALOGS WITH SURFACE CHARGE HETEROGENEITY: EXPERIMENT AND PORE-SCALE SIMULATION

4.1 Abstract

In this work, we studied the transport of colloidal nanoparticles in bead-assembled microfluidic porous media with surface charge heterogeneity both experimentally and numerically. We not only obtained breakthrough curves and retention profiles of deposited nanoparticles, but also recorded the dynamics of nanoparticle deposition at single grain. To compare with our experimental observations, we further developed a pore-scale simulator that combined lattice Boltzmann and random walk particle tracking methods. Simulations of advection and diffusion of nanoparticles under the assumption of irreversible adsorption between nanoparticles and oppositely charged beads were carried out on exact digital reconstructions of experimental porous media. Critical modeling parameters, namely maximum surface coverage and the range of particle-bead interactions, were determined from experiments and first principles of colloidal-surface interaction, respectively. Both breakthrough curves and retention profiles agree well between experiments and simulations for porous media containing collector beads less than 20%. Our work not only reveals that the nanoparticle transport in porous media with surface charge heterogeneities is controlled by irreversible kinetic adsorption and surface blocking, but also presents a complete simulation scheme that uses parameters directly obtained from pore-scale experiments. The elimination of fitting parameters could potentially make pore-scale simulations more predictive than descriptive.

4.2 Introduction

Colloidal particles can find paths into porous sediments and enter groundwater due to their small sizes relative to pores. These particles endanger aquifers in two ways. First, they pose a threat to human health. Engineered particles such as carbon nanotubes, graphene oxide, titanium oxide, and silver nanoparticles released from disposal sites are toxic.[134–139] Biocolloids such as *Cryptosporidium* also contaminate drinking water.[17] Second, colloidal particles could act as carriers for otherwise less soluble contaminants in aqueous environment such as radionuclides, heavy metals, and organic substances.[9] Consequently, contaminants adsorbed to colloidal particles travel over much longer distances than by themselves. Transport of colloidal particles is further complicated by the inherent geochemical heterogeneities present in natural soils and sediments, the composition of which includes different mineral silicates, metal oxides, hydroxides, oxyhydroxide, and organic matter.[140] This mixed composition, under different pH and ionic strengths, renders varied surface charges and wettability of the pore grains, leading to a highly heterogeneous environment. It is therefore imperative to develop abilities to measure and model transport of colloidal particles in geochemically heterogeneous porous media.

Experimental studies on colloid transport are typically performed in centimeter-scale columns filled with model or real soil/sediment grains.[141] Measurements obtained from the column experiments, however, are usually more descriptive than predictive because of the uncertainties in inferring pore-scale transport mechanisms such as irreversible deposition, adsorption and desorption, straining, and aggregation from breakthrough curves (BTC).[57,142–146] Alternatively, porous media analogs (PMA) fabricated with microfluidic technologies allow for direct visualization of both pore structures and particle trajectories via optical microscopy.[103,117,147,148] However, lithographic techniques used for the fabrication of PMAs (and the corresponding hydrodynamic flow in the system) are essentially two-dimensional. Moreover, unlike column experiments where grains with different physical and chemical properties can be packed together to form a heterogeneous porous medium,[51,149,150] PMAs are typically made of a single material with homogeneous surface properties. Although efforts have been made to fabricate chemically heterogeneous PMAs via silane coupling chemistry,[151] UV exposure,[111] or sputtering,[3] varying surface properties in a controllable fashion at the scale of single grain is still a challenge.

In this study, we advanced our previous microfluidic approach[117] to assemble heterogeneous PMAs with a binary mixture of beads containing opposite surface charges. Depending on the sequence to introduce them into the microfluidic channel, a variety of PMA structures with different configurations of surface charge heterogeneities were fabricated. With the position of each bead in PMA registered and their surface properties distinguished by fluorescent labels, the surface charge heterogeneities were tracked down to the level of individual beads. In addition, beads were packed into a 1.5 layer so that the transparency of microfluidic PMA was maintained, allowing us to measure the dynamics of pore-scale colloidal deposition *in situ*, as well as BTC and retention profiles of deposited nanoparticles.

Experiments carried out in these bead-based PMAs offered opportunities to evaluate predictive pore-scale simulations. The pore-scale simulation of advection-diffusion in porous media emerged in early 1990s and is now a powerful method to relate pore-scale mechanisms to macroscopic transport.[152] Early applications focused on characterization of dispersion[153] and only recently direct comparisons with column experiments on the level of BTC have become reality.[154] Simulation of advection-diffusion of solutes or colloids with adsorptive interactions has been reported[114,155,156] but direct comparison with heterogeneous PMA, especially without invoking any fitting parameters, has not been attempted. In this work, exact digital reconstructions of heterogeneous PMAs were used in lattice Boltzmann (LB) and random walk particle tracking (RWPT) simulations. For the first time, an experimentally determined range of colloid-bead surface interaction and a Langmuir surface blocking function were incorporated into RWPT to simulate deposition of colloids without any fitting parameter. Experiments and pore-scale simulations of colloidal transport in heterogeneous porous media are directly compared in this study.

4.3 Materials and methods

4.3.1 Materials

Polydimethylsiloxane (PDMS) was purchased from Dow Corning (Sylgard 184, Midland, MI). 1H-1H-2H-2H-perfluorooctyltrichlorosilane was bought from Gelest (Morrisville PA). Photoresist (KMPR1010 and KMPR1050) came from MicroChem (Newton, MA) and the developer (AZ300 MIF) was from AZ Electronic Materials (Somerville, NJ). 0.5 µm (diameter) carboxylated fluorescent (580/605 ex/em) polystyrene (PS) nanoparticles were purchased from Life Technologies (Carlsbad, CA), 10 µm (diameter) fluorescent (360/407 ex/em) carboxyl-functionalized PS microspheres (*i.e.*, beads) were purchased from Polysciences, Inc (Warrington, PA) and 10 µm amine-functionalized PS microspheres were purchased from Spherotech, Inc. (Lake Forest, IL). The zeta potentials of carboxylated nanoparticles, amine-functionalized beads, and carboxyl-functionalized beads in deionized water were measured by ZetaPALS potential analyzer (Brookhaven Instruments). Three-inch silicon wafers were from Silicon Inc. (Boise, ID). Gauge 30 Tygon tubing was from Saint-Gobain North America (ID = 0.01″, OD = 0.03″, Valley Forge, PA). Biopsy punch (0.75 mm) was from World Precision Instrument (Sarasota, FL). Microfluidic 4-way valve (MV202) was purchased from LabSmith, Inc. (Livermore, CA).

4.3.2 Device fabrication and operation

Microfluidic devices used in this study were fabricated with PDMS using standard soft lithography techniques[123] while master wafers were made by a two-step photolithography procedure reported previously.[117] Here, the first photoresist layer was 8 μm thick (KMPR1010, 8000 rpm for 40 sec) and the second layer was 7 μm thick (44%w KMPR, 4500 rpm for 40 sec).

4.3.3 Microfluidic device operation

Figure 4.1 shows the schematics of our experimental setup for both fabrication of the chemically heterogeneous porous media and measurement of nanoparticle transport and retention therein. Device A2 is a general configuration for us to fabricate four different kinds of chemically heterogeneous porous media where the oppositely charged beads pack into alternating horizontal layers, vertical layers, individual patches, and random mixtures. For the horizontal layer configuration, ‘‘+’’ and ‘‘−’’ beads were withdrawn through the inlet f' alternatingly and the length of each horizontal layer was controlled by both concentration of the beads and solution withdrawing time. For vertical layers, ‘‘+’’ and ‘‘−’’ beads were withdrawn through inlets d' and e' separately. Similarly, the concentration of each type of the beads determines the width of the vertical layers. To create individual patches, we withdrew one type of the beads from inlet d' and e' continuously and the other type from inlet f' intermittently, which formed patches in the porous medium. For random packing configuration, the oppositely charged beads were pre-mixed with certain ratios and they were withdrawn from the inlet f'. The fraction of each type beads in the fabricated porous medium match the pre-mixing ratio well.

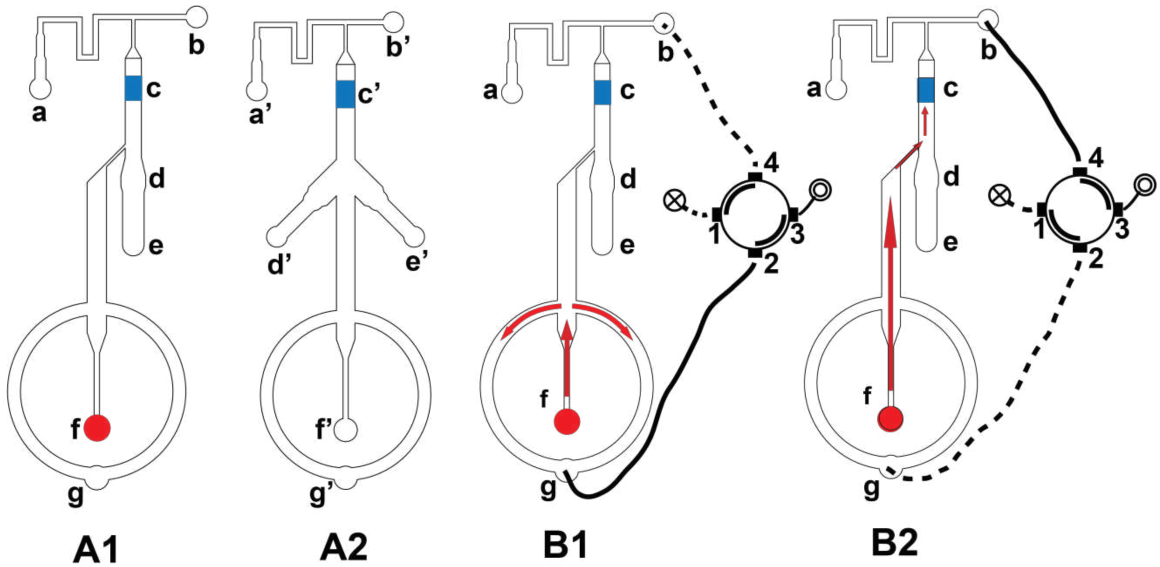

Figure 4.1 Configuration of the microfluidic devices designed to pack a binary mixture of beads into porous media that exhibit chemical heterogeneities and to perform *in situ* colloid transport/retention experiments. (A1) The ports *d* and *f* are the inlets for injecting the beads mixture (10 μm) and nanoparticle suspension (0.5 μm). The port *e* is the inlet for injecting washing solution after the porous medium is fabricated. Outlet *a* connects to a syringe pump that withdraws the bead solution from *d* and the 10 μm beads pack into the porous medium at section *c* because of the height barrier.[117] After the porous medium is fabricated, we stop withdrawing the fluid and block the inlet *d*. Washing solution (i.e., DI water) is then injected from inlet *e* to flush the porous medium for 30 minutes. Suspension of 0.5 μm nanoparticles is then injected at *f* and collected at *b*. *g* is a side channel that connects to an off-chip microfluidic valve that assists to introduce a square-wave input of colloids. (A2) Schematics showing the setup for assembling porous media with various distribution of chemical heterogeneities. The inlets *d'*, *e'*, and *f'* are used for introducing different types of beads, depending on the final porous medium configurations. (B1) Schematics showing the nanoparticle injection mode, where the microfluidic valve is set to block outlet *b* (dashed line) and to open outlet *g* (solid line). (B2) Schematics illustrating the nanoparticle transport mode, where the microfluidic valve is set to block outlet *g* and to open outlet *b*.

Although device A2 demonstrates the feasibility of our bead-based fabrication approach, we designed device A1 for the nanoparticle transport experiments due to better control of the solution injection. It was operated in three different modes: the bead filling, nanoparticle introducing, and nanoparticle transport modes. In the bead filling mode, a dilute mixture (2×10^5/ml) of "+" and "−" beads was withdrawn through inlet *d* by a syringe pump through outlet *a*. All other inlets and outlets were blocked. The beads were then trapped at barrier *c*, where the channel height was reduced from 15 μm to 8 μm. After the fabrication of porous medium, colloidal solution was introduced from inlet *f* and directed to outlet *g* to the open atmosphere through an off-chip 4-way microfluidic valve. The reason that we flushed the nanoparticle solution is to reduce the effect of nanoparticle dispersion in the tubing before it entered the channel when we assembled and flushed the porous medium. After flushing the nanoparticle solution for 5 minutes at 5 nL/s, the nanoparticle concentration entering the channel reached its bulk concentration, then the valve was switched to B2 to inject the nanoparticle solution into the fabricated porous medium at 1 nL/s for 200 seconds. After this, nanoparticle injection was stopped and DI water was injected from inlet *e* at 1 nL/s to wash the bead packing for 80 seconds. During this period the nanoparticle concentration that entered and exited the porous medium were recorded by video microscopy. After that, the microfluidic device was transferred to a confocal microscope for imaging the locations of both beads and nanoparticles.

The dispersion of nanoparticles within the external tubing makes a sharp front at the entrance of the porous medium difficult to achieve. To solve this problem, we used an off-chip 4-way microfluidic valve connected to a cross channel at the upstream of the fabricated porous medium. After flushing the assembled porous medium with DI water for 30 minutes, the nanoparticles suspension entering the device was first directed to outlet *g* through the circular side channels as illustrated in Figure 4.1-B1 to eliminate the influence of dispersion. After the concentration of the incoming nanoparticles reached a steady state, the 4-way valve was turned 90º clockwise to connect outlet *b* to the cross channel and seal the outlet *g*. The nanoparticle suspension was then directed to flow through the porous medium. Figure 4.2 shows the difference of nanoparticles front at the entrance of the porous medium with and without this specific valve design. With the valve, the nanoparticle concentration exhibited a rapid rise and reached steady state in 4 pore volumes (PV). In contrast, the one without valve shows a gradual increment in concentration which did not reach steady state even after 30 PV. Therefore, in all experiments we implemented the valve design.

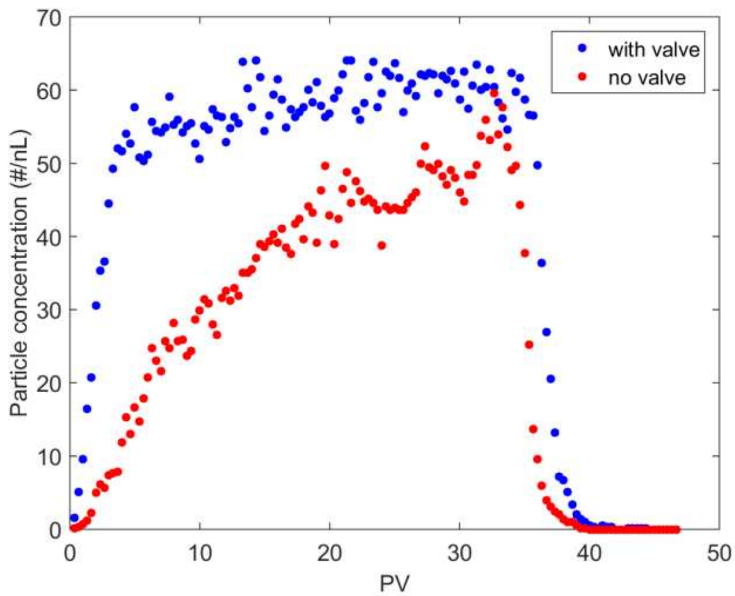

Figure 4.2 Comparison of inlet nanoparticle concentration between operation with and without 4-way valve as a function of pore volume (PV).

4.3.4 Breakthrough curves and retention profiles

Inlet nanoparticle concentration profiles and breakthrough curves were obtained by recording images of nanoparticles in the channel right before they entered and immediately after they exited the porous medium (Figure 4.3). We used a programmable, motorized stage (Prior Scientific, Inc, MA) on an inverted epifluorescence microscope (10X, NA = 0.3, Olympus IX81) so that images were taken at those two locations alternatively with a two-second time interval. After the flow-through experiments, the PMA was transferred to a confocal microscope for beads/nanoparticle location analysis with a customized MATLAB script.

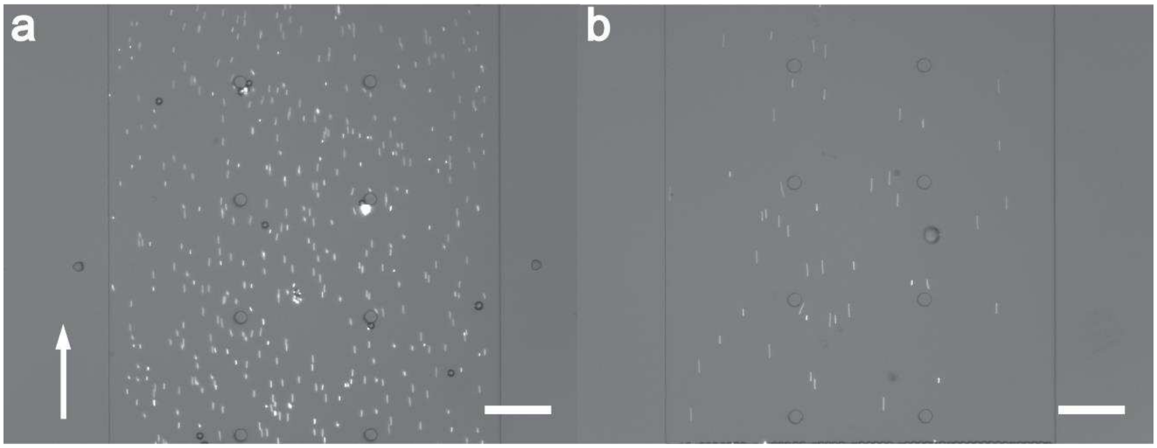

Figure 4.3 Static images (t = 100s) of the nanoparticle solution at (a) inlet and (b) outlet of the porous media randomly packed by 9% "+" beads and 91% "−" beads. The arrow indicates the flow direction. Scale bar: 100 µm.

4.3.5 Identification the locations of individual beads and nanoparticles

We used a confocal microscope (60X, NA = 1.2, Olympus FV10i) to identify the *x-y-z*-position of each bead within the PMA. An image analysis algorithm identified the *x-y* positions of the center for each bead in the PMA. In that, a filter for bead perimeter was set between 10 µm and 51 µm, followed by a second filter for bead area between 4.3 and 25.7 μm^2. Other thresholds in the MATLAB script remain the same as in our previous report.[117] The *z* position of each bead was determined by adjusting the focal plane during the confocal imaging. In addition to the *x-y-z* positions of each bead, fluorescent and negatively ("−") charged beads were distinguished from the non-fluorescent and positively ("+") charged beads.

4.3.6 Pore-scale nanoparticle deposition

The dynamics of nanoparticle deposition on individual beads was measured in separate experiments with the inverted microscope (60X, NA = 1.35) to record events of nanoparticle deposition at a fixed location (field of view = 144 µm × 110 µm, 200 µm downstream from entrance) for one hour with a time interval of one second. Following the experiment, the porous medium was placed under the confocal microscope to measure the three-dimensional (3D) position of the deposited nanoparticles. The dynamics of nanoparticle deposition in the porous medium was modeled as[52]

$$\frac{\partial \theta}{\partial t} = \pi a_{\mathrm{p}}^2 k_{\mathrm{p}} C B(\theta) \tag{3.1}$$

where θ is the fractional surface coverage of a bead, determined from the pore-scale experiment. t is time, a_{p} is nanoparticle's radius, k_{p} is the rate constant of deposition, C is nanoparticle concentration in the solution, and $B(\theta)$ is the surface blocking function described in the next section. Eq. (4.1) was solved numerically with an initial condition of $\theta = 0$ at $t = 0$. We used explicit Euler method for temporal discretization.

$$\frac{\theta^{j+1} - \theta^{j}}{\Delta t} = \pi a_{\mathrm{p}}^2 k C B(\theta^{j}),\ j = 0, 1, 2, ..., N_t \tag{3.2}$$

where N_t is the numbers of temporal grids. To capture enough information from the domain, we applied a uniform temporal grid $N_t = 1000$. Our benchmarking procedure showed that the relative error evaluated using maximum norm is less than 0.1 %. We then performed numerical simulations for given operating parameters. Using the Least Square fitting method, we determined the coefficient k_{p} that fitted the experimental measurements best.

4.3.7 Random sequence adsorption (RSA) model

During the deposition there is a surface blocking effect caused by the deposited nanoparticles occupying adsorption sites on "+" beads. To describe this phenomenon in the pore-scale simulations, we used the RSA model to describe the surface blocking function $B(\theta)$, the probability of particle adsorption for a given surface coverage θ. Based on a statistical approach developed by Schaaf *et al*[157] for non-interacting particles,

$$B(\theta) = 1 - c_1\theta + c_2\theta^2 + c_3\theta^3 \tag{3.3}$$

We note that Eq. (2) applies only when $0 \le \theta \le \theta_{\max}$. When screened Coulombic interaction between deposited nanoparticles is taken into account, the coefficients in Eq. (4.3) are[158]

$$c_1 = 4\left(\frac{1+H^*}{1+A}\right)^2,\ c_2 = \frac{6\sqrt{3}}{\pi}\left(\frac{1+H^*}{1+A}\right)^4,\ c_3 = 1.407\left(\frac{1+H^*}{1+A}\right)^6 \qquad (3.4)$$

Here, H^* is a dimensionless length that characterizes the range of electrostatic repulsion between deposited nanoparticles, A is the aspect ratio of nanoparticles to beads. To find H^*, we let Eq. (4.3) satisfy the boundary conditions $B(\theta) = 1$ at $\theta = 0$ and $B(\theta) = 0$ at $\theta = \theta_{\max}$, where $\theta_{\max}$ is 0.051, determined from our pore-scale experiments. Calculations gave $H^* = 2.2$, $c_1 = 37.2$, $c_2 = 285.5$, and $c_3 = 1127.3$.

4.3.8 Reconstruction of microfluidic PMAs

A custom MATLAB code was used to generate voxel-based computational domains for LB and RWPT simulations, based on reconstruction of fabricated microfluidic PMA. The center locations of beads came from experiments and the diameters of both "–" beads and "+" beads were set to 10 μm. Pillars of diameter of 24 μm were used to provide mechanical support in the large-aspect-ratio microfluidic channels. The computational domains for homogeneous PMAs contain only "–" beads while those of heterogeneous PMAs contain both "+" and "–" beads. All computational domains were discretized into cubic voxels, whose size is 1 μm. The overall size of the computational domain was set as 602 voxels in width, 17 voxels in height, and 1981 voxels in length. The total number of voxels exceeded 20 million and the number of fluid voxels was about 11 million.

4.3.9 Lattice Boltzmann (LB) and random walk particle tracking (RWPT) simulation of fluid flow and nanoparticle transport through bead-based microfluidic PMAs

A single-phase parallelized D3Q19 LB code with multiple relaxation time (MRT) collision operator[159] was used to obtain steady-state velocity fields in digitalized PMAs.[160] We assume that flow fields are not affected by surface charge heterogeneities (*i.e.* no net electrokinetic flow) and a constant body force was applied to drive the flow. A RWPT code was developed to solve advection-diffusion of nanoparticles through the PMAs.[117] Volumeless tracers representing nanoparticles were moved on the same voxel-based computational domains that LB used. The steady-state velocity fields obtained from LB simulations were passed to RWPT to determine advective displacements of tracers. Diffusive displacements by random motions were then added to locate the final positions. The scheme to move the tracers follows the method of biased random walk

$$\boldsymbol{x}(t+\Delta t)=\boldsymbol{x}(t)+\boldsymbol{v}(\boldsymbol{x}(t))\Delta t+\sqrt{6D_0\Delta t}\boldsymbol{\xi} \tag{3.5}$$

where $\boldsymbol{x}$ is the location of tracers, $\boldsymbol{v}$ is the velocity, t is the time, Δt is the time step, D_0 is the molecular diffusion coefficient, and $\boldsymbol{\xi}$ is a randomly oriented vector whose size follows a Gaussian distribution with unit variance.

As nanoparticles are highly charged and non-aggregative with each other, the RWPT code did not consider tracer-to-tracer interactions. The no-flux boundary condition between nanoparticles and non-adsorbing surfaces was implemented in RWPT using a specular reflection method by which a tracer is reflected on the interface between solid and fluid nodes. Heterogeneous PMAs contained a certain percentage of "+" beads and these beads attract nanoparticles by electrostatic attraction and retain particles by combined electrostatic and van der Waals forces. Hence, over surfaces of "+" nodes specular reflection was disabled. Instead, nanoparticles that are within a capture distance L away from a "+" solid node were captured and retained on the bead. This treatment models nanoparticle deposition as a kinetic process rather than an equilibrium process, following the observations from the pore-scale experiments that depositions always occurred irreversibly. The capture distance L was determined from the Derjaguin-Landau-Verwey-Overbeek (DLVO) theory that governs the double-layer interaction between the nanoparticle and bead[161]

$$U/kT = \frac{\varepsilon}{4}\frac{kT}{e^2}\frac{a_1 a_2}{(a_1 + a_2 + h)}\left[(y_1 + y_2)^2 \ln\left(1 + e^{-\kappa h}\right) + (y_1 - y_2)^2 \ln\left(1 - e^{-\kappa h}\right)\right] \quad (3.6)$$

where kT is the thermal energy, e is the electron charge, a_1 (5 μm) and a_2 (250 nm) are radii of the "+" bead and the carboxylated (negatively charged) nanoparticles respectively, $y_i = \zeta_i e / kT$ is the scaled surface potential of particle i, h is the surface to surface distance, ε is the permittivity of the solvent, and κ^{-1} is the Debye length.[162] Although we used deionized (DI) water in our experiments, dissolved carbon dioxide (CO_2) from air still generates H^+ and HCO_3^- ions. The concentration of H^+ can be inferred from the pH, which measured 5.8, in agreement with data provided by Ropp *et al*.[163] Correspondingly, the concentration of HCO_3^- was estimated to be 2.23×10^{-6} M, which yields a Debye length of 205 nm. This value, however, is on the higher end of the Debye length reported in literature,[164–166] since ion leakage from both glassware and particle surfaces usually would further reduce the Debye length. Here, we used the value from Kampf *et al*,[167] which gives a Debye length of 68 nm by fitting the experimentally measured double layer interactions with the DLVO theory. Figure S4 shows the interaction energy as a function of surface-to-surface separation h. We assumed that when $U/kT = 10$, nanoparticles would be irreversibly deposited on the beads, which occurs when $h = 4\kappa^{-1} \sim 272$ nm. After taking the radius of nanoparticle (a_1=250 nm) into account, the capture distance L in the RWPT simulation was set to $a_1 + h \sim 500$ nm, equivalent to half of the voxel size.

In RWPT, to suppress statistical noise in the BTCs, 55,000 tracers were released into the computational domain. In the experiments, the concentration of nanoparticle was ~70/nl leading to ~370 nanoparticles in one PV of PMA. The ratio of tracers to nanoparticles is therefore approximately 150, which means that 150 tracers in RWPT are statistically equivalent to one nanoparticle in the experiment. Therefore, in the implementation of the blocking function on the surface of a "+" bead, the maximum adsorptive capacity of a single voxel was scaled by the experimentally determined maximum retention of nanoparticles on a single "+" bead as

$$n_{node} = N_{bead} \times \frac{\text{tracer-to-nanoparticle ratio}}{\text{surface area of bead}} \approx 40 \qquad (3.7)$$

where Nnode is the maximum tracer adsorptive capacity of a single "+" voxel in RWPT and Nbead (=82) is the maximum number of nanoparticles retained on a "+" bead measured directly from pore-scale experiments. With this conversion established, the RSA model was then applied to RWPT on "+" voxels to simulate the effect of surface blocking.

4.4 Results and discussion

4.4.1 Fabrication, characterization, and digital reconstruction of heterogeneous PMA

To assemble a porous medium with heterogeneities in surface charge, we injected suspension of both amine- and carboxyl-functionalized beads (*i.e.*, the "+" and "–" beads) into microfluidic channel (600 µm ×15 µm) supported by pillars. The measured zeta potentials of these beads were 59 ± 1 mV and −40 ± 5 mV, respectively. If we directly mix these oppositely charged beads in deionized water, they will aggregate with each other and deposit on the channel wall. To solve this issue, we mixed these two types of beads in 0.01 M sodium hydroxide solution. Since the pK_a of alkylamine is ~10, the "+" beads bear negative surface charges at pH

12 ($\zeta = -92 \pm 2$ mV). This surface charge reversal allows us to inject the mixture into the microfluidic chamber without deposition or aggregation. After the beads were injected to form the porous medium, we perfused DI water (20 nL/s for 30 minutes) to lower the pH to ~ 6 and restored the positive surface charge on the "+" beads. An *ex situ* measurement confirmed that the zeta potential of the amine-functionalized beads recovered to 68 ± 4 mV (Table 4.1).

Table 4.1 Zeta potential measurement of the amine-functionalized ("+") beads under different conditions.

	DI water	0.01M NaOH	washing off NaOH and re-suspending in DI water
zeta potential (mV)	57.52	-90.16	63.04
	58.59	-94.17	72.08
	59.41	-90.93	69.96
mean	58.51±0.77	-91.75±1.74	68.36±3.86

The image processing procedure are shown in fig. 4.4 for fluorescence beads recognition and fig. 4.5 for top and bottom beads identification. Fig. 4.4a shows the original beads packing image after merging the grey (bright field), blue (DAPI fluorescence) and red (TRITC fluorescence) channels into one RGB image. In the composite the green particles are "-" charged, the blue particles are "+" charged, the large blue circle at the bottom left corner is the pillar we used to support the channel. Fig. 4.4b is the grey channel extraction from the composite. From which we obtained the x-y coordinate of all the beads in the field of view, shown as the blue dots in the center of each beads. In fig 4.4c, the non-fluorescent beads ("+" charged) are filtered out due to their low intensity in the isolated blue channel, then the blue channel is overlaid with grey channel to map out the "-" beads in bright field, displayed by blue dots in the figure. In the last step, the "-" beads centers are subtracted from all beads centers to discern the "+" beads, shown as yellow dots in fig 4.4d.

In fig 4.5, a similar procedure is taken to discern the beads located at the bottom of the channel from those at the top. Fig 4.5a is same as fig 4.4b, which detects the centers of all the beads. In fig 4.5b, we focused on the top beads in the packing, indicated by the blue centers. By subtracting the top beads from all the beads, the bottom beads centers are determined. In fig 4.5c, blue dots indicate top beads, red dots indicate bottom beads. Combined this results with the fluorescent label results, we are able to obtain the x-y-z coordinate of both types of beads in our porous media.

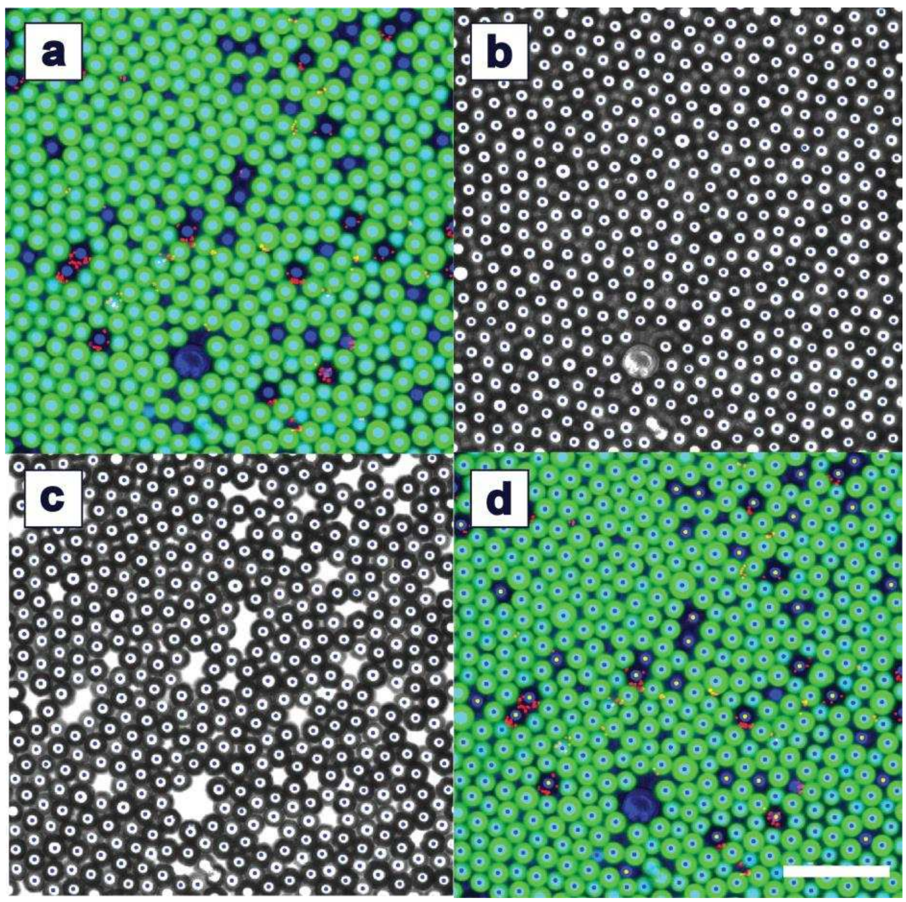

Figure 4.4 Image processing procedures for distinguishing "+" and "-" beads based on their fluorescence. (a) Original composite image with grey, blue, red channels overlaid. (b) Detected centers for all the beads in the grey channel. (c) Detected centers for "-" beads based on blue and grey channel composite. (d) Detected centers for both "+" and "-" beads. Scale bar: 50 µm

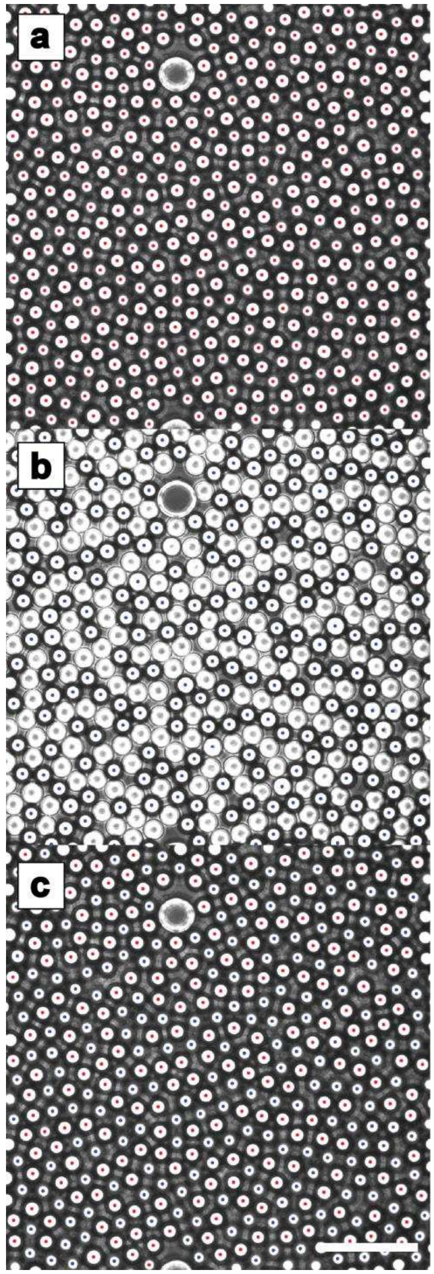

Figure 4.5 Image processing procedures for distinguishing top and bottom beads based on their focal plane. (a) Detected centers for all the beads. (b) Detected centers for top beads based on their higher vertical position (d) Detected centers for both top and bottom beads. Scale bar 50 μm.

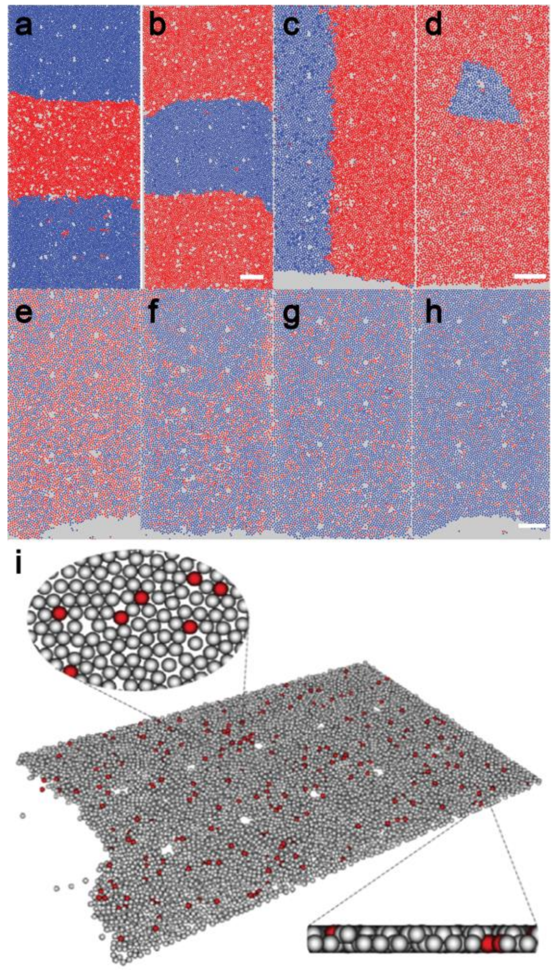

Figure 4.6 Porous media analogs (optical image with pseudo colors) with different configurations of charge heterogeneity: (a) and (b) alternating horizontal layers, (c) vertical layers, (d) a single patch, and (e)-(h) random mixtures with 48%, 24%, 17%, and 9% “+” beads, respectively. The red and blue spheres represent amine- (“+”) and carboxyl-functionalized (“–”) beads, respectively. Scale bars: 100 µm. (i) Digital reconstruction of the porous medium with randomly mixed 4% “+” and 96% “–” beads. The insets show top and side views, and red and gray represent “+” and “–”, respectively. The two column of void space in the figure are pillars used to support the channel not plotted in the figure.

Figures 4.6a-d show different configurations of surface charge heterogeneities made in device A2. Oppositely charged beads were packed into alternating horizontal layers, vertical layers, or patches. Figures 4.6e-h show media with different fractions of “+” beads randomly mixed with “–” beads and these media were used to study nanoparticle transport. To quantify the degree of randomness in bead packing, we computed the two-dimensional radial distribution function $g_{\alpha\beta}(r)$ defined as

$$g_{\alpha\beta}(r)=\frac{1}{m_\alpha}\sum_{i=1}^{m_\alpha}\frac{n_\beta}{2\pi r\Delta r\rho_\beta} \tag{3.8}$$

where α and β represent "+" and "–" beads respectively, m_α is the number of reference α-type beads, n_β is the number of β-type beads within distance r and $r + \Delta r$ from a specific reference α-type bead, and ρ_β is the number density of β-type bead. Figure 4.7 shows that the experimentally measured $g_{\alpha\beta}(r)$ are in good agreement with those from a numerically generated porous media where particle types were randomly assigned for different fractions of the "+" beads. This agreement confirms that our porous media are indeed random mixtures of oppositely charged beads. The *x*-*y*-*z* positions of beads in porous media, identified from image analysis over confocal images, allowed us to digitally reconstruct the porous media (Figure 4.6i) for LB and RWPT simulations.

4.4.2 Pore-scale measurement of nanoparticle deposition dynamics

A unique advantage of our approach is that we can directly measure the *in situ* dynamics of particle deposition at the level of a single grain. Video S1 shows temporal deposition of nanoparticles in a porous medium with heterogeneous surface charge consisting of 7% "+" and 93% "–" beads (in green and blue respectively). In the video, the focal plane was chosen near the middle of the channel at ~7 μm from the bottom substrate. The red dots are 0.5 μm fluorescent carboxylated PS nanoparticles. For beads located at the bottom of the chamber, deposited nanoparticles were obscured by the beads' equator and thus a ring appeared surrounding the bead due to light scattering. The video shows that, as expected, most nanoparticles deposited on the "+"

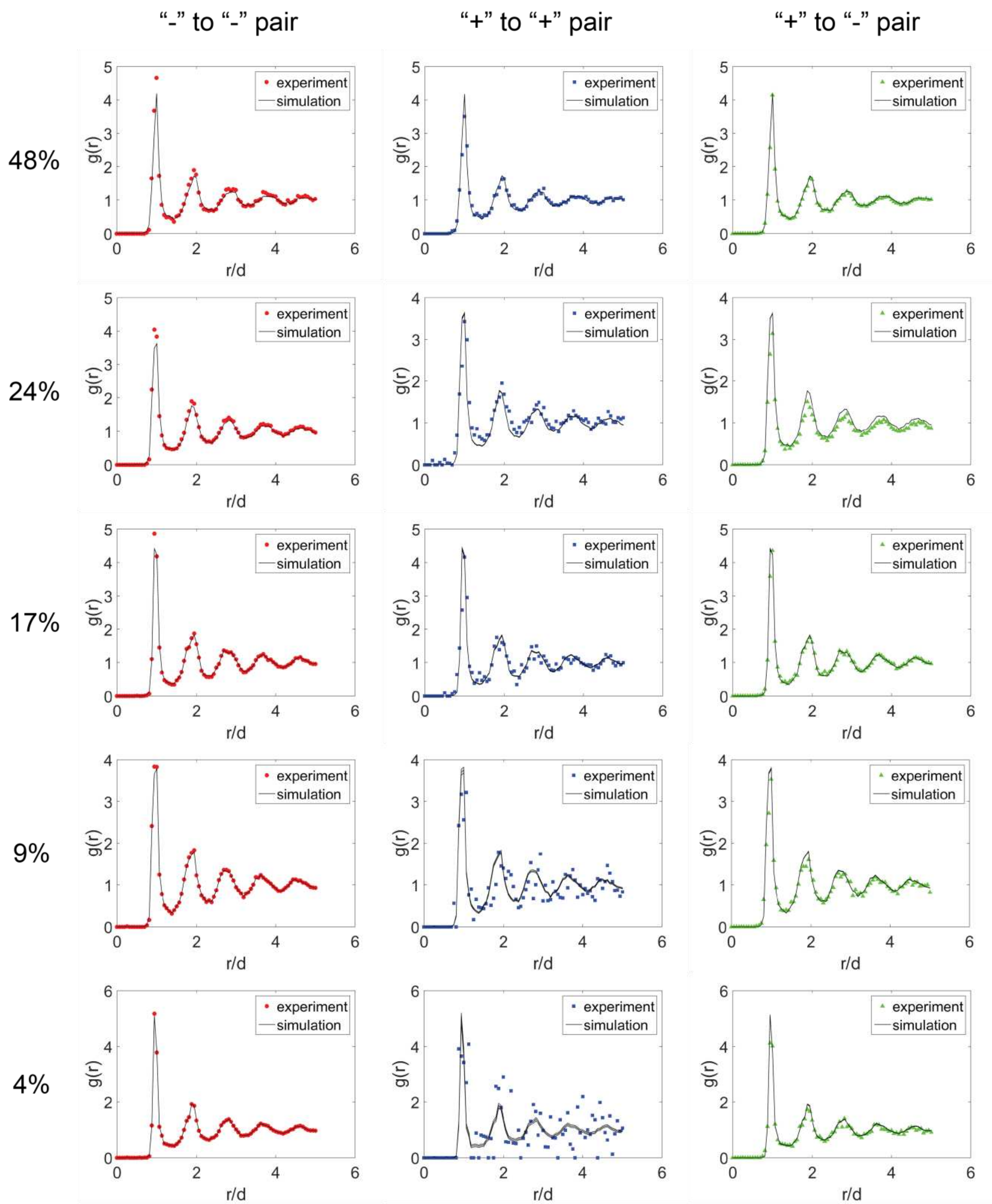

Figure 4.7 Radial distribution functions $g_{++}(r)$, $g_{--}(r)$ $g_{+-}(r)$ for different pairs of beads measured in the fabricated porous media that are randomly packed by different fractions of "+" and "–" beads. The solid lines are obtained from numerically simulations. .

bead, but a few also deposited on the "–" beads either due to straining or DLVO interaction at the secondary minimum.[168] From the video, we also observed that most nanoparticle deposition occurred first on the upstream hemisphere of the "+" beads. As the adsorption sites were gradually filled there, particle deposition progressively moved to the downstream hemisphere. This phenomenon can be seen more clearly by observing the nanoparticle deposition at single bead level (Video S2).

Figure 4.6a shows deposited nanoparticles on the bottom hemisphere of a "+" bead at different focal planes after flowing 80 particles/nL solution for one hour at 1 nL/s. Figure 4.8b shows the digital reconstruction of 3D positions of nanoparticles based on Figure 4.8a. Clearly, more particles deposited on the front, upstream hemisphere than the rear, downstream hemisphere. The bottom left corner of the "+" bead is free of deposited particles because there is a nearby "–" bead at touching distance, physically blocking the access and preventing nanoparticles from depositing.

Figure 4.8c shows the temporal change of surface coverage of five "+" beads in Video S1. The variation in these data could be due to the variance in these "+" beads' positions relative to their "–" neighbors and surface potentials. The general trends, however, are consistent. Surface coverage increased linearly for the first ~200 seconds and then attenuates as binding sites fill. All curves demonstrate surface-blocking, *i.e.*, the initially deposited particles hinder the deposition of later particles nearby, similar to Langmuir effect.[52] When we fit the experimental data in Figure 4.8c to Eqs. (4.1) and (4.3) solved by finite difference we obtained a deposition coefficient $k_{\mathrm{p}} = 6.8 \pm 1.59 \times 10^{-6}$ (m/s). This value is ten-fold higher than reported by Johnson *et al.*[52] However, considering that our "+" beads have a higher zeta potential (68 mV vs. 20 mV) and our experiment was conducted in DI water, which leads to a longer particle-surface interaction range, the k_p value appears reasonable. We further found an average 82 ± 13 nanoparticles were deposited per “+” bead (n = 5) after 1 hour. Hence, we use N_{bead} = 82 in Eq. (4.7) for RWTP simulations.

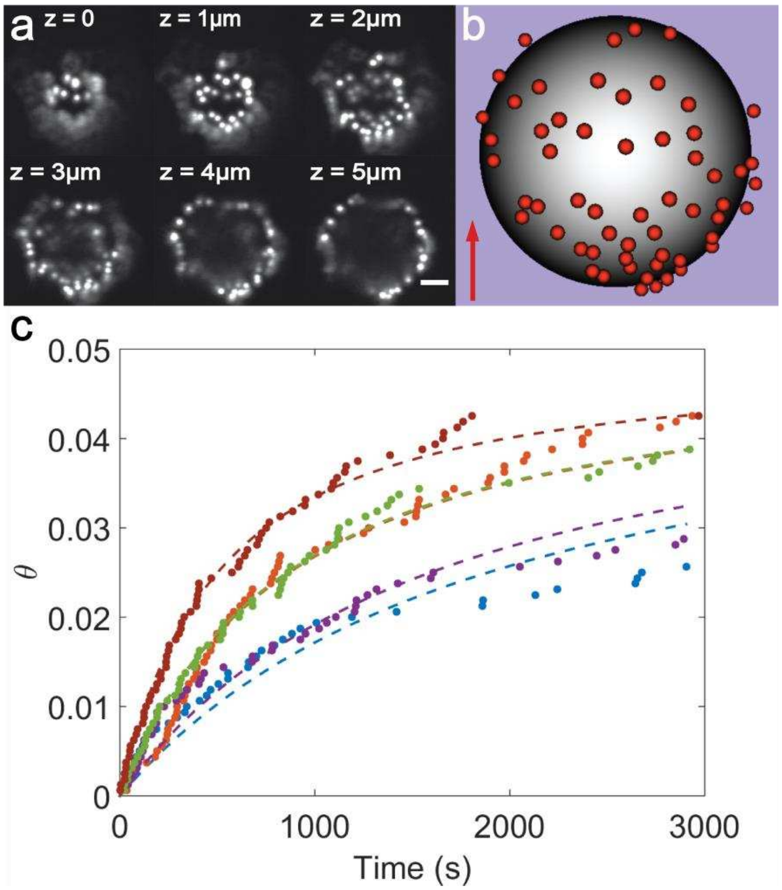

Figure 4.8 Nanoparticles deposited on a “+” bead. (a) Snapshots of confocal microscopy images scanning from the bottom of the bead to its equator with 1 μm step change and (b) the digital reconstruction of deposited nanoparticles on the bottom hemisphere. The flow direction of nanoparticles is indicated by the red arrow. Scale bar: 3 μm. (c) The time evolution of surface coverage (θ) on five different “+” beads. Dashed lines are the least square fits based on Eqs. (4.1) and (4.3).

4.4.3 Experimentally measured and simulated breakthrough curves

Experimentally measured BTCs were generated from a square wave input concentration profile of 0.5 μm carboxylated PS nanoparticles (ζ = −45 ± 1 mV) achieved with a 4-way off-chip valve. Figure 4.7a shows the BTCs for porous media packed with different fractions of “+”

beads. For the homogeneous medium packed by "–" beads only (0%), the curve reached the plateau of C/C_0 ~ 1 at around five pore volumes (PV). In comparison, the onset of "plateau" was delayed to approximately eight PV for porous media with even a small fraction of "+" beads (4% and 9%). Note that "plateaus" in these two cases were not perfectly leveled. Past eight PV, the concentration still increased with increasing PV slowly because of surface blocking. When the "+" beads fraction was increased further, no clear plateau was observed. Instead, the outlet concentration increased continuously until terminated by the DI water flush introduced at 200th second. A notable observation is that the presence of a small fraction of "+" beads in the porous medium can significantly alter the BTC. For example, only 4% "+" beads in the porous medium reduced plateau of the BTC by 60% (Fig. 4.8a). When the fraction of "+" beads is 24%, almost no nanoparticle can pass through the porous medium. This observation agrees qualitatively with results obtained from column experiments.[52]

Our collaborator performed corresponding numerical simulations using the LB-RWPT approach. The molecular diffusion coefficient in RWPT was chosen to match the Péclet number of the experiment, $Pe = ud/D = 1295$. Here u is the superficial velocity through PMA, d is the diameter of beads, and D is the diffusion coefficient of nanoparticles. To faithfully simulate experiments, they used logistic growth curves to fit the actual inlet concentration profiles so that the nanoparticle concentration measured at the inlet was reproduced in the simulation Details of this procedure are explained in the Cho's thesis.[169] It is worth noting here that efforts spent in matching the inlet concentration profile led to significant improvements in the agreements of BTCs between simulations and experiments, and hence it is a procedure highly recommended for future studies.

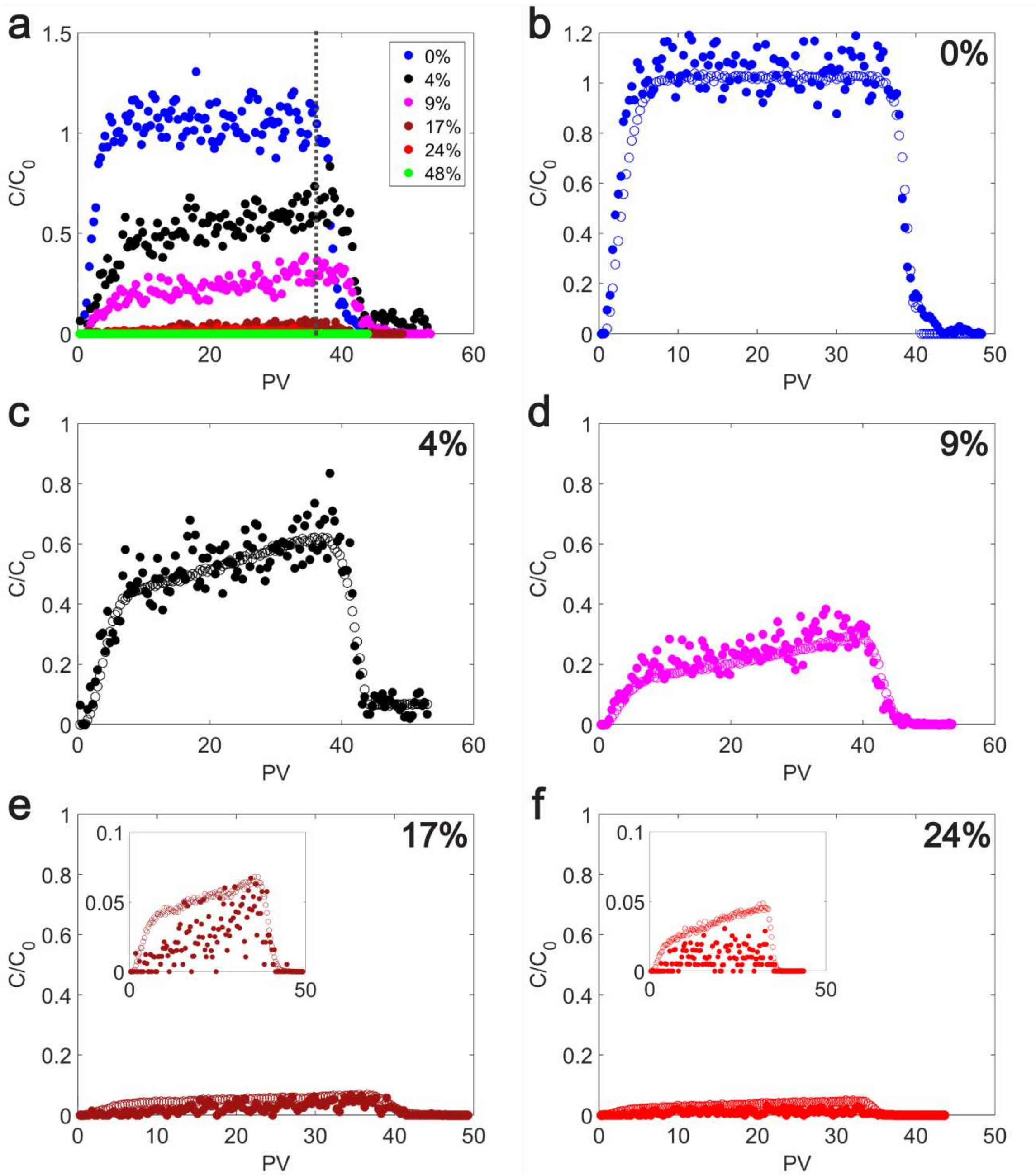

Figure 4.9 (a) Experimental breakthrough curves (BTC) for the transport of 0.5 µm carboxylated nanoparticles in chemically heterogeneous porous media packed by amine- ("+") and carboxyl-functionalized ("−") beads at different mixing ratios. The normalized concentration (C/C_o) at the outlet of the PMA is plotted as a function of pore volumes (PV) injected. 1 PV is 5-6 nL. The dash line indicates the moment when DI water flushing started. (b-f) Experimental (filled symbols) and simulated (hollow symbols) BTCs of PMAs with 0% 4%, 9%, 17%, and 24% "+" beads. Inset in e and f are the zoom in of the corresponding BTC. Simulations used capture distance $L = 0.5$ µm and nodal adsorption capacity $n_{\text{node}} = 40$ obtained from experiments.

Figures 4.9b-d show that RWPT simulations implemented with inlet concentration profiles, interception length for electrostatic adsorption, and blocking functions measured from experiments can predict the dynamics of nanoparticle transport and retention in PMA with low percentages of "+" beads (0%, 4%, and 9%). This good agreement between experiments and simulations confirms that the dominant mechanisms that controlled advection-dispersion and the shape of BTCs of nanoparticles in heterogeneous PMA are irreversible electrostatic adsorption combined with surface blocking. For PMA with higher fractions of "+" beads (17% and 24%), the effluent concentration profiles predicted by RWPT were slightly higher than experimental data. This discrepancy may come from three sources: the volumeless representation of nanoparticles in simulations, neglecting of particle interactions between nanoparticles, and differences between real PMAs and their digital reconstructions. First, the RWPT method models nanoparticles as volumeless points, and thus omits the effect of straining as well as adsorbed particles on the flow. Straining is significant for high "+" beads fractions, as the pore could be surrounded by "+" beads and narrowed by the nanoparticles adsorbed on these beads, leading to straining and potential clogging. In contrast, for low "+" beads fraction, "+" beads are normally far from each other, and "−" beads barely adsorb nanoparticles, the straining is not significant. Second, the RWPT neglects the interactions between nanoparticles and "−" beads as well as among nanoparticle themselves. The interactions include van der Waals and electrostatic repulsion; the electrostatic repulsion is expected to be dominant over the van der Waals interaction due to the high surface charges of the nanoparticles. And it could lead to more nanoparticles approaching "+" beads. Lastly, digitally constructed PMAs had a uniform height of 15 μm; PMAs in the experiments, however, tend to have reduced heights approaching the sides of the PMAs, an imperfection from the fabrication. As a result, there were extra void spaces along the sides of the PMAs in the simulations. We observed that these void spaces generated preferential flow paths that were not present in the experiments. Tracers could pass through PMAs through these spaces easily without encountering many “+” beads, leading to effluent concentrations higher than those from the experiments.

4.4.4 Experimentally measured and simulated retention profiles

Figure 4.8 shows retention profiles as the number of deposited nanoparticles as a function of distance along PMA measured by confocal microscopy. All retention profiles were obtained at the end of experiments used to generate the BTCs in Figure 4.9. We neglected 0% case because the fraction of deposited nanoparticle was less than 1% of the injected total. Figure 4.10a shows that the retention profiles follow an apparent logarithm relationship with distance, which is consistent with filtration theory.[170] Additionally, the slope of the retention profile appears to increase as the fraction of “+” beads decreased.

This observation may be explained as smaller “+” beads fraction allows deeper nanoparticles penetration into the PMA. We observed that, for the 17% “+” beads case, there were a few hundred nanoparticles deposited near the end of the PMA. For the 24% “+” beads case, however, deposition dropped sharply to tens of nanoparticles about 800 μm into the PMA, which means that nearly all flowing nanoparticles were adsorbed upon reaching this point. This measurement agrees with our BTC data that barely any nanoparticles were detected in the effluent for the 24% “+” beads case. For the 48% “+” beads case, the retention profile showed a steep decline at 400 μm and there were no nanoparticles 600 μm into the PMA.

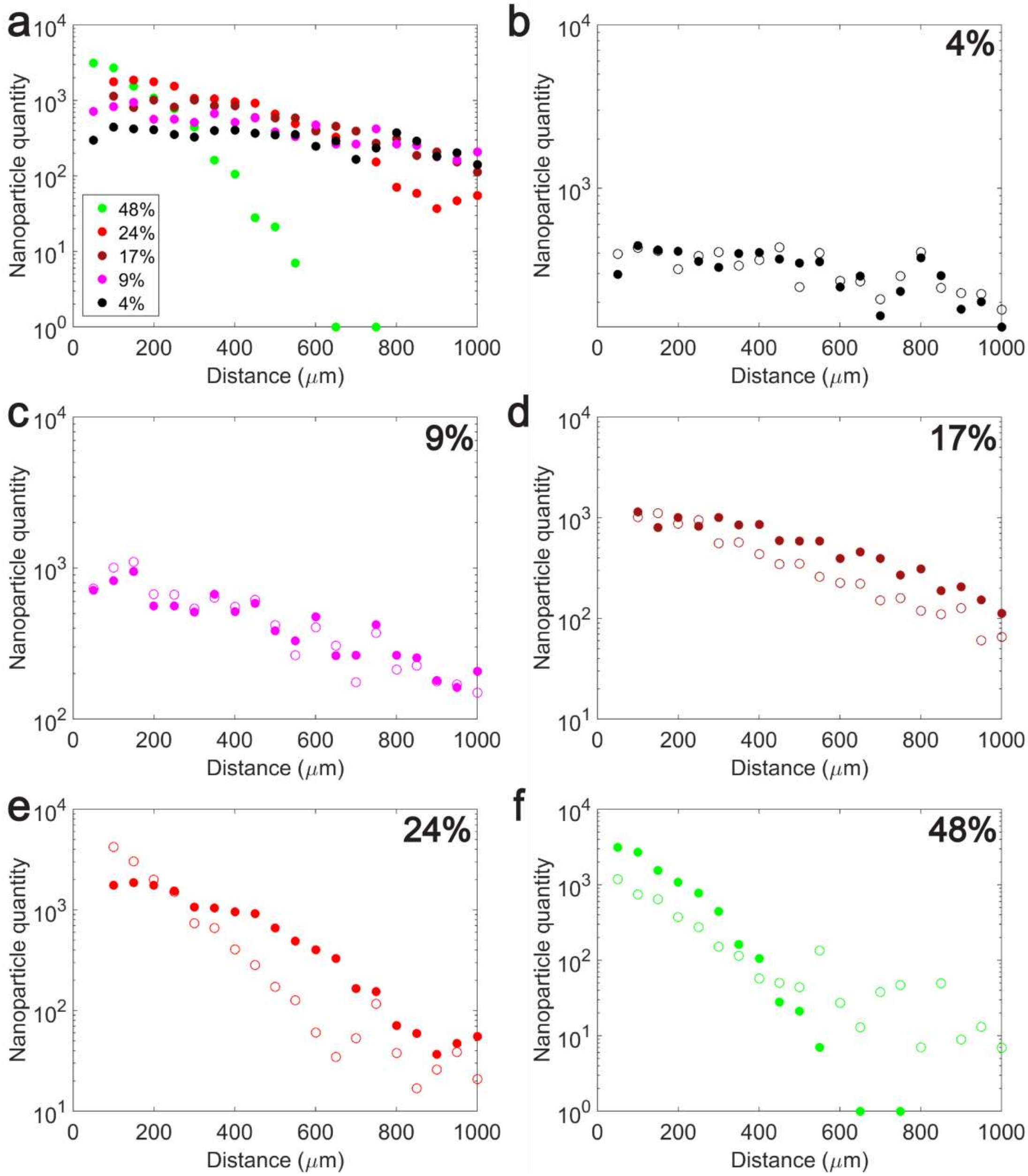

Figure 4.4.10 (a) Experimentally measured retention profiles of 0.5 μm nanoparticles in chemically heterogeneous PMAs with 4%, 9%, 17%, 24% and 48% "+" beads. (b-f) The comparison between experimental measured (solid) and simulated (hollow) retention profiles at different "+" beads fractions.

Similar to the comparison of BTC, retention profiles obtained from RWPT agrees well with those from experiments when the fraction of "+" beads is 4% and 9%. Fluctuations in the simulation data were mainly caused by the local variations in the fraction of "+" beads. Starting from the case with 17% “+” beads, simulation results began to deviate from experiments. The experimental profiles concave slightly upwards, whereas the simulation results were roughly linear. For the cases with high fractions of “+” beads (17%, 24%, 48%) the retention profiles from experiments were all higher than those from simulations, which is consistent with the observation from the BTCs that in these cases simulations predicted more nanoparticles flowing through the PMAs than experiments. The possible reasons include the volumeless representation of nanoparticles in simulations, the neglect of interactions between nanoparticles, and the differences between real PMAs and their digital reconstructions, as discussed above.

In summary, we presented a new approach to fabricate microfluidic PMAs consisting of randomly packed spherical beads of opposite surface charge properties. Such kind of PMAs allowed us to experimentally study the transport of nanoparticles in chemically heterogeneous soil / sediment environments. We also performed numerical simulations based on the LB and RWPT methods in the same PMAs. Using experimentally determined maximum surface coverage and blocking functions of nanoparticle deposition and theoretically derived nanoparticle-surface capture distance, our RWPT simulations successfully reproduced both breakthrough curves and retention profiles of nanoparticles measured from the experiments without any fitting parameter. Our comparative study shows that transport of nanoparticles in chemically heterogeneous PMAs was indeed primarily controlled by irreversible kinetic adsorption and surface blocking / exclusion. Good agreement between experiments and simulations also indicates that the developed simulation scheme, using parameters directly obtained from the single pore experiments, can be generalized and extended to future applications in simulating transport in porous media with other types of surface interactions.

4.5 Acknowledgments

This work is supported by the Department of Energy NEUP program via Grant DE-NE0000719 and National Science Foundation CAREER awards (CBET-1454095, N.W. and CBET-1351672, K.B.N.).

CHAPTER 5

MULITPHASE FLOW IN POROUS MEDIA ANALOGS WITH WETTABILITY HETEROGENEITIES

5.1 Introduction

Multiphase flow in porous media has been widely studied because it is important to several environmental and industrial applications such as enhanced oil recovery (EOR), CO_2 sequestration, non-aqueous phase liquid (NAPL) remediation, and membrane separation. To better understand this phenomenon in details, researchers have developed micromodels that replicate the porous structures commonly found in real reservoir and subsurface. Meanwhile, these micromodels are made of transparent materials (e.g., glass, PMMA, PDMS, and NOA81), which greatly facilitates direct observations of multiphase flow behavior at pore scales.

The origination of micromodels dates back to 1950s when Chatenever *et al.* first sandwiched a layer of glass beads between two glass plates.[95] With this setup they studied the water-oil displacement in both channel flow and slug flow regimes. But at that time, the limitation of imaging technologies prevented them from obtaining very detailed and informative images. Later Mattax *et al.* used the wet etching method to engrave channel networks on a glass plate that was covered by a layer of wax and followed by bonding it with another glass plate to seal the system.[70] But at early era wet etching had some problems like poor sealing and abnormal curvature at the channel bottom. Later on in the 90s, when PDMS was widely used in soft lithography, one can conveniently fabricate a mold by using photolithography and wet etching and mass-produce PDMS-based micromodels by using soft lithography, which greatly simplified the fabrication produces and reduced the cost.[123] Since then, micromodels began to appear more and more in the studies of multiphase flow.

In 1988, Lenormand *et al.* conducted both micromodel experiments and numerical simulations for two-phase (oil-water) displacement under the drainage condition. They mapped out the phase diagram of viscous and capillary fingering based on both capillary number and viscosity ratio.[106] Later on Wan *et al.* used micromodels to visualize the transport of colloidal particles in unsaturated porous media and found that they were easily trapped at the gas-water interface.[99] Jeong *et al.* studied the foam flooding removal of NAPL in micromodels and found that using surfactant foam was twice more effective in removing residual trichloroethylene (TCE) than just surfactant flooding.[171] In the above studies, however, the micromodels used were mostly made of one material with uniform surface properties. Hence, they are called chemically homogeneous micromodels. In recently years, some researchers started to modify the surface of micromodels to create heterogeneities in terms of wettability or surface charge. For example, Ma *et al.* used UV-ozone treatment to oxidize and hydrophilize the surface of PDMS micromodels.[19] Trojer *et al.* silanized glass beads to different degree of hydrophobicity and packed them in a Hele-Shaw cell.[110] Zhao *et al.* used chemical vapor deposition of silane and deep UV exposure to modify the wettability of NOA81 surface in the micromodel.[111] Lee *et al.* applied stop flow lithography to fabricate pillars with different wettability by using different photoinitiators and crosslinkers.[94]

Except for Lee's method, all other approaches can only modify the surface property uniformly, and Lee's method has a drawback of low resolution and large pore space, which limited its application in multiphase flow studies. Here, we developed a bead-based micromodel that utilized two types of beads with very different wettability to oil and water and fabricated the porous media analogs. By using fluorescent beads we are able to distinguish one type from the other. We further demonstrated that our micromodel provides a useful platform in studying multiphase flow in porous media with wettability heterogeneity.

5.2 Materials and methods

5.2.1 Materials

Norland Optical Adhesive 81 (NOA81) was purchased from Norland Products (Cranbury, NJ). Polydimethylsiloxane (PDMS) was purchased from Dow Corning (Sylgard 184, Midland, MI). 1H-1H-2H-2H-perfluorooctyltrichlorosilane was bought from Gelest (Morrisville PA). Photoresist (KMPR1010) came from MicroChem (Newton, MA) and the developer (AZ300 MIF) was from AZ Electronic Materials (Somerville, NJ). Fluorescent (465/480 ex/em) polystyrene (PS) particles (7.4±0.5 μm in diameter) were purchased from Spherotech, Inc. (Lake Forest, IL). 8 μm silica microspheres were purchased from Fiber Optic Center Inc. (New Bedford, MA). Low viscosity mineral oil was purchased from ASI standards (Oak Ridge North, TX). FD&C Blue #1 was purchased from Spectrum Chemical Mfg. Corp. (New Brunswick, NJ). Decane (30570), Sigmacote and Oil Red O was purchased from Sigma-Aldrich (St. Louis, MO). Reagent alcohol (200 proof, ACS grade) was purchased from Pharmco-Aaper (Shelbyville, KY).

5.2.2 Device fabrication and operation

Microfluidic devices used in this study were fabricated with NOA81 using soft lithography techniques. A master wafer was made by a two-step photolithography procedure reported previously.[117] Here, the first photoresist layer was 14 μm thick (KMPR1010, 2000 rpm for 40 sec) and the second layer was 11 μm thick (KMPR1010, 3000 rpm for 40 sec). Then a polydimethylsiloxane (PDMS) mold was imprinted from the master wafer and used to mass-produce NOA81 devices. Before NOA81 molding, the inlets and outlets on the PDMS mold were punched using a 0.75mm biopsy punch. Gauge 22 blunt needles that were dipped in 1 mm^3

liquid PDMS that was aged for 12 hours were inserted in all inlets and outlets. The aged PDMS was solidified after 30-minute baking at 80 ℃. This step aimed at building a cone shape inlet to reduce the adhesion of beads at the inlet during the experiments.

During the fabrication of NOA81 devices, gauge 22 blunt needles were placed in all inlets/outlets to ensure their connectivity after molding. For the beads inlet, a piece of 3×3 mm PDMS panel was punched and hung on the needle. A PDMS frame (2mm thick) was first placed outside of the channel, then 1ml NOA81 was dropped inside the frame and formed a reservoir at the same height of the frame.[172,173] The PDMS panel on the needle was pushed to immerse at the same level of the NOA81. The liquid NOA81 was cured after exposing under 365 long-wave UV for 150 seconds from the top and 40 seconds from the bottom. Then all the needles were removed, and the device was placed with channel features facing up in a petri dish for future surface modification. In parallel, a 25×75 mm glass slide was prepared with spin coating NOA81 at 2300 rpm and exposed under same UV for 75 seconds from the top. Then the channel surface was modified to be hydrophobic (see details in the next section) and the device was pressed on the NOA81 slide firmly and exposed under long-wave UV from the top for 120 seconds. Afterwards, the whole device was baked on a hot plate at 60 ℃ for 3 hours to age the NOA81. After that the gauge 30 Teflon tubing was epoxied on all inlets and outlets except the beads inlets.

In the experiments, the beads used to assemble the porous media were first introduced as a suspension in reagent alcohol. Reagent alcohol was chosen because it disperses both the hydrophilic and hydrophobic beads well. Inside the channel, the flowing beads were stopped by a line of pillars placed at the downstream. After the porous medium was formed, decane was injected to flush the porous media for 100 pore volume (PV). Since decane is miscible with the reagent alcohol that we used, this flushing did not form any liquid-liquid interface that may disturb the bead packing. After the decane wash, low viscosity mineral oil (7 cst at 25 ℃) was injected for 100 PV to completely replace decane as the defending fluid. In the last step the dyed water was injected under a constant pressure and the displacement process was recorded under an optical microscope (10X, NA = 0.3, Olympus IX81). The recording stops at water breakthrough.

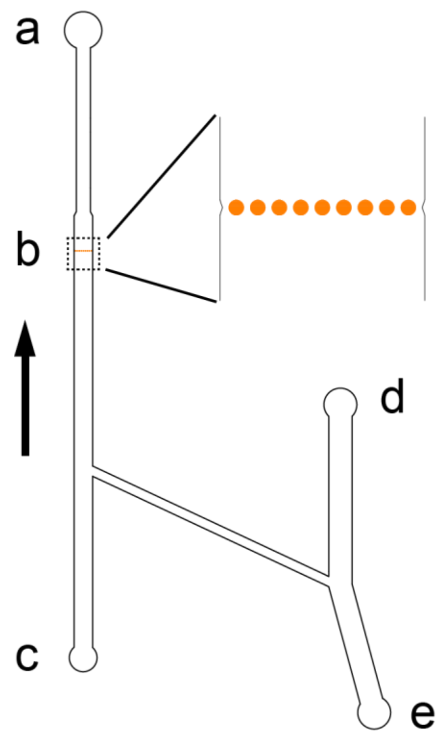

Figure 5.1 Configurations of the microfluidic device used for multiphase flow experiments, where *a* is the outlet of the channel, *b* is the cylindrical stoppers (orange circles) that assemble the porous media, *c* is the inlet for beads, decane, and mineral oil, *d* is the inlet for dyed water, and *e* is the outlet used to discharge the water/oil emulsion and form a stable interface when water is first injected.

5.2.3 Device and beads surface modification

In order to create a drainage environment, the surface of the channel was modified to be hydrophobic to prevent any preferential flow during the experiments. Here we adopted the chemical vaper deposition (CVD) method (Zhao *et al.*) to modify the unbonded NOA81 device and slide with 10 μL 1H-1H-2H-2H perfluorooctyltrichloro-silane in a vacuum desiccator for 30 minutes.[111] The silica beads is naturally hydrophilic. To make it hydrophobic, 1 gram of the beads were immersed in 0.5 mL Sigmacote for 1 minute and washed with reagent alcohol for three times. The modified beads were stored in reagent alcohol as well.

To make the hydrophilic PS beads to have a similar surface composition as the silica beads, we grew a thin SiO_2 shell on the PS beads using Graf *et al.* method.[174] 0.4 mL 1% PS particle stock solution was washed 3 times in reagent alcohol to remove water. Then the suspension was dispersed in 4 mL poly vinylpyrrolidone (PVP, M_w=360k) solution in ethanol (7 g/L). After that, 0.33 mL ammonium hydroxide and 0.8 mL 10% tetraethyl orthosilicate dissolved in ethanol were added drop-by-drop sequentially under stirring. Finally, the suspension was placed on a rotator (100 rpm) to react for 12 hours. After the reaction, the beads were washed by deionized (DI) water and stored in reagent alcohol.

5.2.4 Image analysis to measure the invading fluid saturation and fractal dimension of the fingering patterns

In order to analyze the displacement pattern from the experiments, a customized MATLAB script was used. The optical image was first cropped along the porous media's boundary with the *polycrop* command. Then the gray scale image was turned into a binary image by *im2bw* with a certain threshold. At last the oil saturation was obtained by dividing the number of black pixels (remaining oil) by that of total pixels in the image.

The fractal dimension of the fingering patterns is an important parameter to characterize the extent of branching/fingering during oil displacement. Here a box-counting script developed by Moisy was used to determine the occupancy of black pixels in boxes of variable dimensions and the slope of the filled boxes vs. box size gives the fraction dimensions.[175]

5.2.5 Phase diagram estimation

In Lenormand *et al.* paper in 1988, they predicted a phase diagram that separated different regimes of invading patterns based on their numerical and theoretical calculation.[106] Following their method, we estimated the phase diagram as well as the location of our experimental regime. First, we estimated the permeability of the porous media based on the Darcy's law.

$$Q = k\frac{A\Delta P}{\mu L} \tag{3.9}$$

where the volumetric fluid flowrate $Q = 0.4 \times 10^{-12}$ m^3/s, viscosity $\mu = 1\times10^{-3}$ Pa·s, the length $L = 1.5\times10^{-3}$ m, and the cross-sectional area $A = 2.4\times10^{-9}$ m^2. The permeability is ~ 2.5×10^{-14} m^2, which is close to 1×10^{-13} m^2 base on our previous measurement.[117] Here we adopt $k = 1\times10^{-13}$ m^2 for simplicity.

According to Lenormand *et al.*, three kinds of forces should be considered here, the viscos force of the displaced fluid 1, viscous force of the invading fluid 2, and capillary force between fluids 1 and 2. The viscosity ratio M is defined by μ_2/μ_1. The phase diagram can then be estimated by comparing the viscous and capillary pressures.

viscous pressure:

$$P_v = \frac{\mu v L}{k} \tag{3.10}$$

capillary pressure:

$$P_c = \frac{\gamma\cos\theta}{r} \tag{3.11}$$

where γ is the interfacial tension between two phases, r is the radius of pores, and θ is the contact angle of invading fluid. The capillary number Ca is defined as

$$Ca = \frac{\mu \, v}{\gamma} \tag{3.12}$$

where u is the linear velocity of the invading fluid 2. At large Ca number, the capillary force is negligible, so the displacement pattern only depends on the viscosity ratio M. Under such a situation, when M is small, viscous fingering dominates, and when M is large, the displacement is stable.

At small Ca number, stable capillary fingering can be observed when the viscous pressure of the invading fluid 2 is negligible ($P_v < P_c$), *i.e.*, $v/\gamma < k\cos\theta/\mu Lr$. In zone I, $\mu = \mu_1$, so the capillary number $Ca = \mu_2 v/\gamma < M \times k\cos\theta/Lr \approx 4\times10^{-5} M$. In zone III, where the displacement is stable, $\mu = \mu_2$ and $Ca = \mu_2 v/\gamma < k\cos\theta/Lr \approx 4\times10^{-5}$. As Ca increases, the viscous pressure dominates, i.e., $P_c < P_v$. Therefore, in zone I, $\mu = \mu_1$, $Ca = \mu_2 v/\gamma > M\times k\cos\theta/Lr \approx 4\times10^{-5} M$. In zone III, $\mu = \mu_2$, $Ca = \mu_2 v/\gamma > k\cos\theta/Lr \approx 4\times10^{-5}$. The phase diagram is shown in Figure 2, where the dash lines are based on above estimation, which was validated by simulations where a constant water saturation was achieved at fixed M and varying Ca.[106]

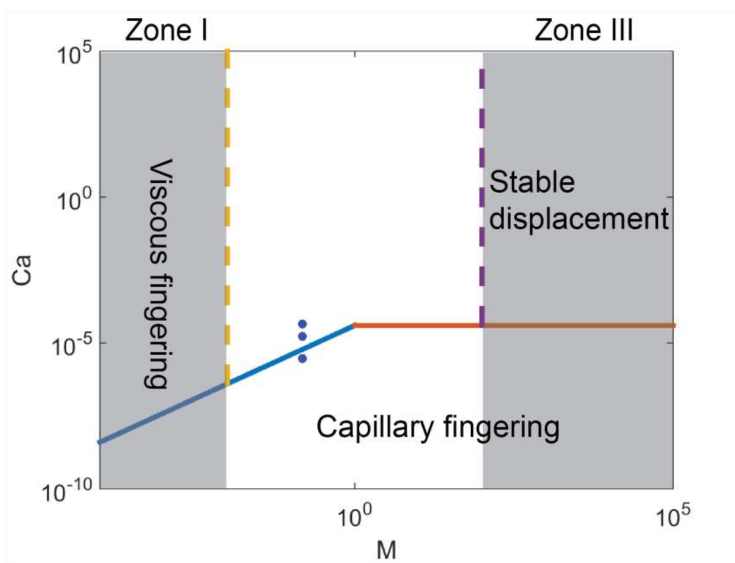

Figure 5.2 The estimated phase diagram based on our experimental parameters. The dots indicate the location of our experiment condition

5.3 Results and discussion

We first measured the contact angles of the thin films formed by hydrophilic and hydrophobic beads by using a KSV Cam 200 (Fig. 5.3). The water-air-particle three-phase-contact lines can be clearly seen. The contact angles measured by image analysis are 79° for the hydrophilic beads and 129° for the hydrophobic beads, respectively. There is a clear difference in wettability between these two types of beads.

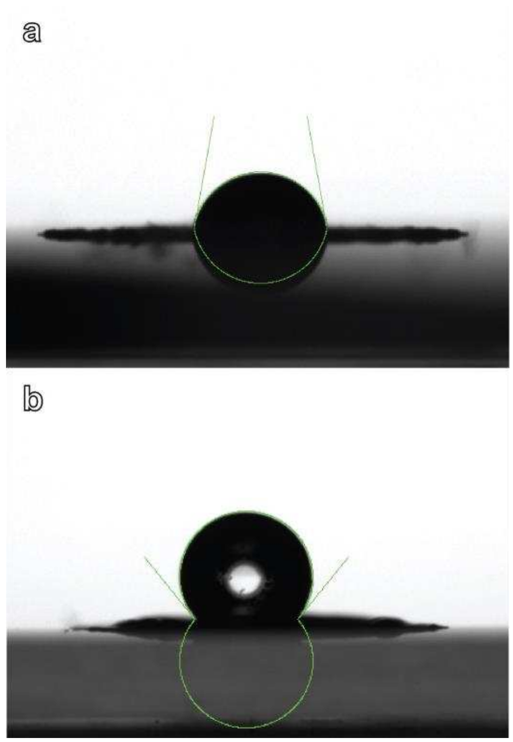

Figure 5.3 The measurement of contact angles for surfaces that are covered by (a) hydrophilic beads (PS microspheres coated by a thin layer of pristine SiO_2) and (b) hydrophobic beads (SiO_2 micropsheres coated by alkylsilane molecules).

The procedures to make the porous media were similar to what we have reported in Chapter 4. And once assembled, the porous medium was saturated by mineral oil. Since the refractive index of the silica beads is close to the mineral oil, using a 10X objective does not reveal the edges of silica beads clearly. Instead we saw grey discs. Note that the white space between two silica beads or between silica and PS beads does not indicate that it is empty, the edges of the silica beads are not clear enough to create a significant contrast with the oil. For PS beads, since their refractive indices are quite different from that of the mineral oil, we can see their clear edges when they are immersed in both oil and water.

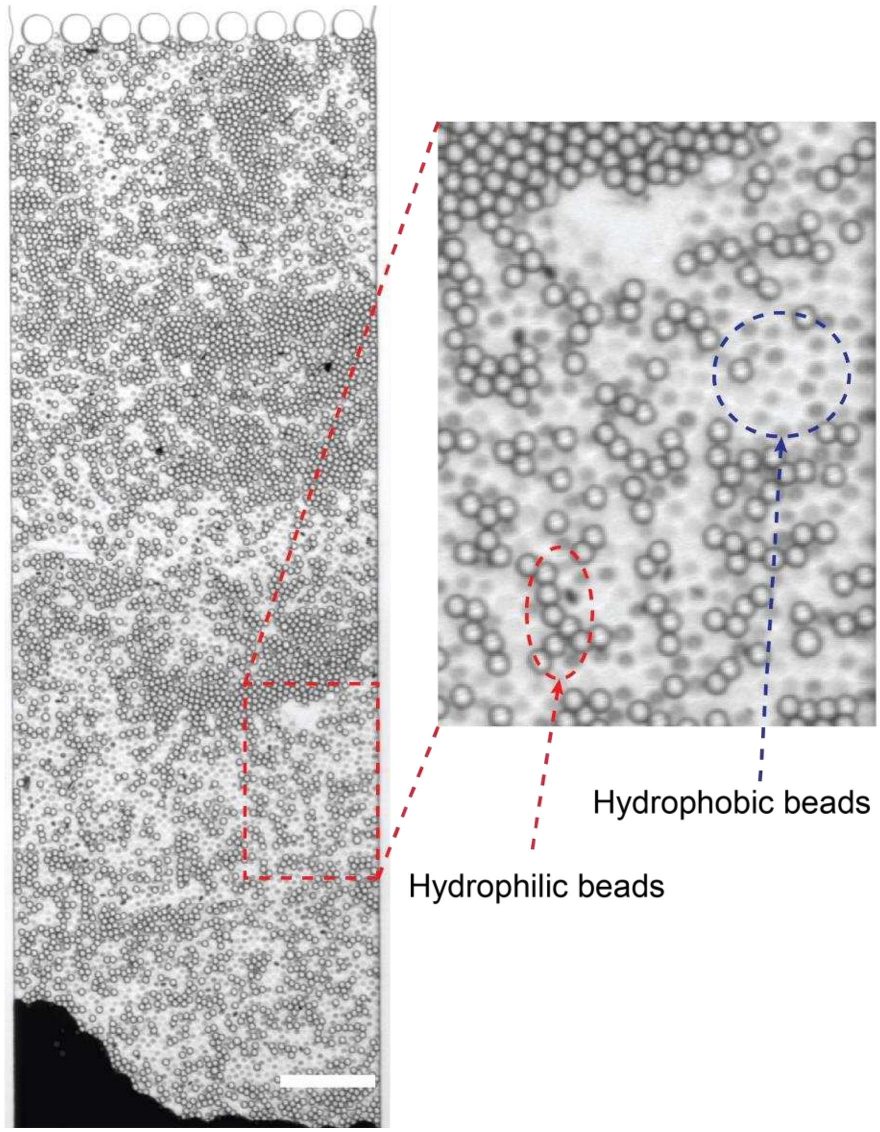

Figure 5.4 The mixed wettability porous medium with ~40% hydrophobic beads. The zoom-in image illustrates the difference in optical contrast between hydrophilic (those with clear edges) and hydrophobic beads (grey discs). Scale bar: 100 μm.

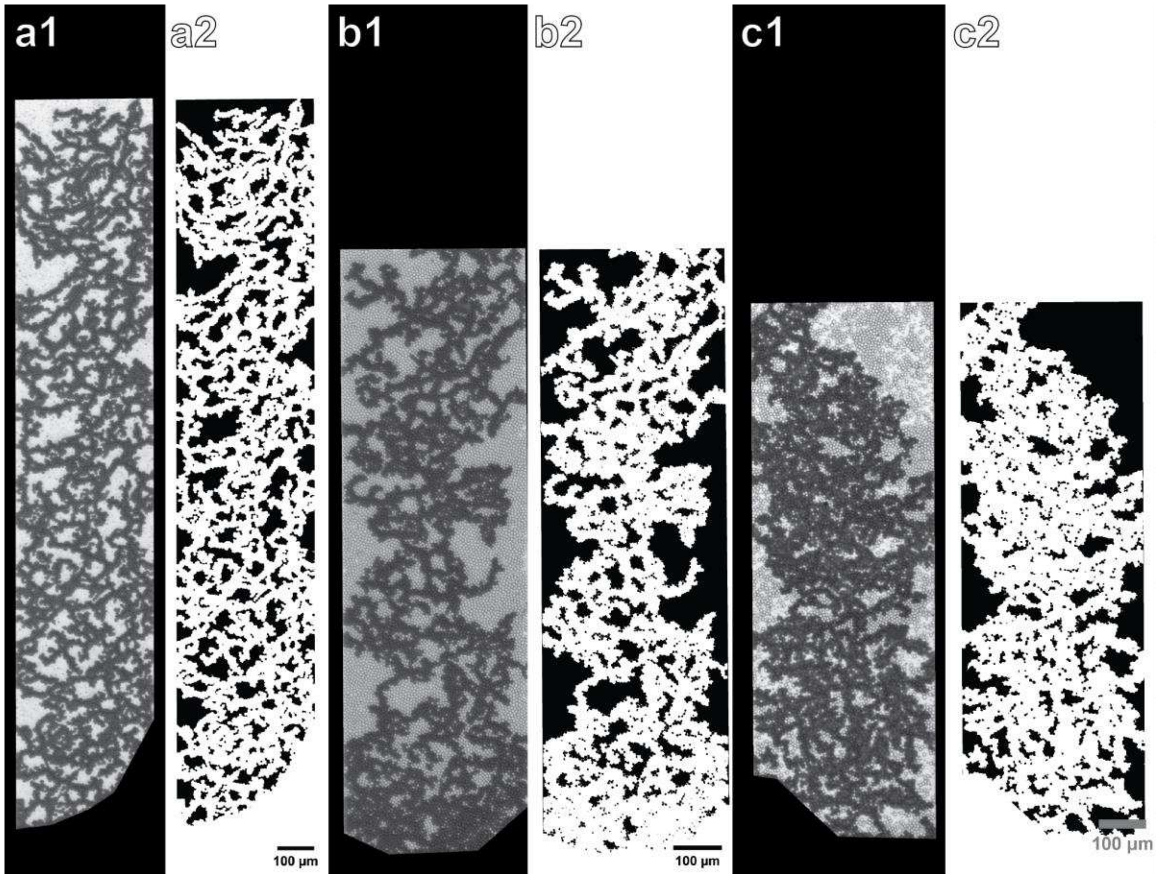

Figure 5.5 The optical images of mineral oil displacement by dyed deionized water in porous media packed by (a1) all hydrophilic beads, (b1) all hydrophobic beads, and (c1) a mixture of hydrophilic and hydrophobic beads. The dark color indicates the dyed water while the defending oil is transparent (in light grey). The corresponding binary images after image processing are shown in (a2) – (c2). After the image processing, the invading water is converted to white and the oil is in black.

Our image processing program also captured the oil displacement patterns well shown in Fig 5.5. With such a program, we are able to calculate the invading water saturation, the fractal dimensions of the fingering patters, and the breakthrough flow rates of water. Based on our experimental conditions, the viscosity ratio M = 0.15 (The viscosities of mineral oil and dyed water are 7 mPa·s and 1.03 mPa·s, respectively) and capillary number $Ca = 2.96\times10^{-6}$-4.45×10^{-5}, we expected that our operating regime is located near the upper boundary of the capillary fingering regime in Fig. 5.2 (shown in blue dots). Our experimental observations confirmed this as the development of fingering patterns in general is toward all directions, rather than simply pointing to the downstream, which is characteristic to viscous fingering. But in terms of how the fingering patterns developed, there were some differences between these three types of porous media. For the one packed by all hydrophobic beads, water initially invaded from several locations and grew simultaneously to form a network-like invading pattern. In comparison, in the one packed by all hydrophilic beads two distinct stages displayed. At the first stage of oil displacement, the water invasion was slow and had multiple invading points. But water saturation at the end of this stage was very high – it reached 82%. However, water invasion during this period only spanned roughly 20% of the total length of the porous medium, although it took about 60% of the total displacement time. In the second stage, during each time interval, there was only one location that generated an invasion towards the exit. After this invasion, from the same location or some previous invading locations, breakthrough occurred toward the side or backward directions. Meanwhile, water saturation during this second stage was smaller than that during the first stage. The time spent at this stage was ~40% of the total displacement time.

Table 5.1 The overall water saturation and fractal dimensions (D_f) of the fingering patterns at the end of oil displacement experiments

	Hydrophobic medium	Hydrophilic medium	Mix wettability medium
Ca	4.45×10^{-5}	1.69×10^{-5}	2.96×10^{-6}
water saturation	0.64	0.59	0.64
D_f	1.9	1.83	1.85

Compared to the previous two cases, the displacement pattern for the mixed wettability porous medium did not have clear invading features. At some time, it looked like the hydrophobic case where several invasion routes appeared simultaneously. While during other time, it was similar to the case of hydrophilic beads where only one invasion occurred. Counterintuitively, most invasions happened along the paths formed by the hydrophobic beads rather than the hydrophilic ones. But for the capillary invasions behind the front, most of them happened around hydrophilic beads, which helped increase the overall saturation.

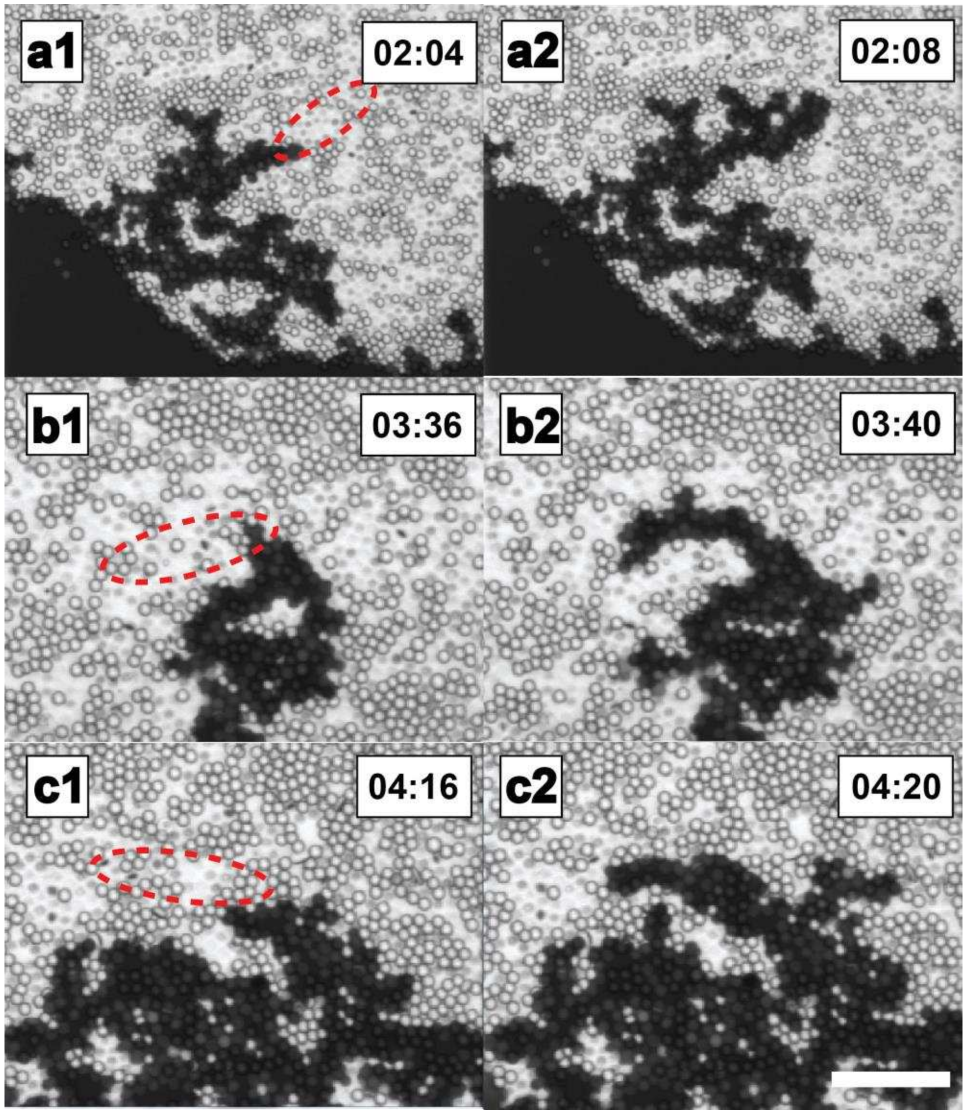

Figure 5.6 Three water-invasion patterns in the mixed wettability porous media. The red dashed circles in the left column indicate the locations where water invaded. Scale bar: 100 µm.

There are several possible explanations for this phenomenon. One would be that the hydrophobic beads are actually slightly smaller than the hydrophilic beads, therefore the pore space created between the hydrophobic beads and the channel is slightly larger than that created by hydrophilic beads. In order to test this hypothesis, we used image processing program to measure the average diameter of two kinds of beads based on their center-to-center distances. From our measurement, the average diameter of the silica particles is 8.0 μm, while the average diameter of the polystyrene beads is 7.2 μm. Hence, this hypothesis is disproved.

Another possible reason could be since the hydrophobic beads have a good affinity to oil, when water invades, those beads retained a thin film of oil on their surfaces which reduced the resistance for water flow. This phenomenon had been observed in many microfluidic experiments where coating of oil on the surface of the channel facilitated the generation of water droplets.[176] In contrast, for hydrophilic beads, no such layer of lubrication oil existed therefore the flow resistance was higher. However, our current observation is only based on one experiment performed in the mixed wettability porous medium. To test this hypothesis, additional experiments with dyed oil phase will be needed.

5.4 Conclusion

We have successfully fabricated micromodels with wettability heterogeneities by packing two types of beads of the similar size but different water contact angles. The micromodel was made of high elastic modulus material with optical transparency, which allowed us to directly characterize the displacement of mineral oil by deionized water in three types of porous media: those packed by all hydrophilic beads, by all hydrophobic beads, and by a mixture of hydrophobic and hydrophilic beads. The one packed by all hydrophobic beads has the highest water saturation and the largest fractal dimension in the fingering pattern, while the one packed by all hydrophilic beads has the lowest water saturation. While it is still hard to draw any solid conclusion about the development of viscous and capillary fingering patterns, our preliminary results demonstrated a promising platform for future studies of multiphase flow in porous media.

CHAPTER 6

SUMMARY AND OUTLOOK

6.1 Summary

In this thesis we have investigated a new approach that is versatile enough to make bead-based micromodels with chemically homogeneous or heterogeneous porous media with pore size ranging from 1 to 5 μm. With specially designed accessories such as off-chip valves, exit T-junctions, and side channels, we are able to directly observe the pore-scale transport behavior under optical microscope and obtain population data for colloidal particle transport and water-oil displacement in porous media. In addition, with the custom-made image processing programs we also digitally replicate the exact experimental porous media, which are used in numerical simulations. Therefore, faithful comparison between experiments and simulations under the same experimental conditions is allowed.

In Chapter 3, we first developed the bead-based micromodel to make homogeneous porous media. With this setup we obtained the pathlines of individual colloidal particles flowing through the bead pack. Based on the velocities calculated from the pathlines we demonstrated the size exclusion effect in colloidal transport. Meanwhile, we designed a T-junction at the exit of the porous media to collect the exiting colloidal particles with aqueous droplets in mineral oil, which facilitated measurement of the breakthrough curves. In addition, the beads location detection program was applied to obtain the *x-y* coordinate of each bead in the porous medium.

In Chapter 4, we further improved this method to assemble porous media with different configurations of surface charge heterogeneities, by packing a mixture of oppositely charged beads in the microfluidic channel. In particular, by soaking aminated PS beads in 0.01M sodium hydroxide, we were able to temporarily change their surface charges from positive to negative, thus preventing them from aggregating with the negatively charged beads in the mixture or sticking to the channel wall during device fabrication. After fabricating the porous media, the positive surface charges on the animated PS beads were restored by flushing DI water. With such a method we were able to form various configurations of the surface charge heterogeneities such as horizontal layers, vertical layers, single patch, and random mixture. Moreover, due to the fluorophore carried on the negatively charged beads, we could distinguish them from the positively charged beads under fluorescent microscopy. By using an improved bead location detection program and confocal microscopy, we were able to identify the *x-y-z* coordinate of each bead as well as its surface property. Using such information an exact reconstruction of the experimental porous media was accomplished in the simulation domain. LB and RWPT were applied to simulate the breakthrough curves and retention profiles for different ratios between the oppositely charged beads. The comparison between experiments and modeling showed good agreement when the fraction of positively charged beads was below 17%. In addition, the dynamics of pore-scale colloidal deposition on a single positively charged bead was measured and the maximum surface coverage and surface blocking function were extracted from the experiments and used in RWPT.

In Chapter 5, we further expanded the application of our bead-based porous media to the study of multiphase flow. Here, we adopted a different material called NOA81 which has a modulus 1000 times higher than that of PDMS to fabricate the micromodel. It can withstand high pressure required for large flow rates or more viscous fluid. At the same time, we modified the surface of NOA81 hydrophobically to create a drainage condition for the water-oil displacement. Hence, by injecting a mixture of silanized hydrophobic silica beads and hydrophilic PS beads in ethanol in the microfluidic channel, we were able to fabricate porous media with well-defined heterogeneous wettability. We studied the displacement of more viscous mineral oil by deionized water in porous media packed by purely hydrophobic beads, purely hydrophilic beads, and a mixture of hydrophobic and hydrophilic beads. The overall water saturation and fractal dimensions of the fingering patterns in these three types of porous media were measured.

6.2 Outlook

6.2.1 Colloidal transport study at pore scales

In the RWPT simulation, we assumed that the negatively charged colloidal particles did not deposit on negatively charged PS beads due to electrostatic repulsion. But in our pore-scale experiments, there were still a small fraction of colloids adsorbed. Johnson *et al.* believed that impurities on the beads could provide a mechanism for colloidal attraction.[116] However, in our experiments, there were clearly two kinds of adsorption. In some cases, the colloids were trapped firmly on the beads, which appeared to be resulted from strong attraction forces. There were also cases that the colloids were trapped loosely on the beads, with some freedom to move within a limited range near the surface of beads. Moreover, we have also observed colloids that were slowed down by the nearby positively charged beads but finally captured by a negatively charged bead. All these phenomena seem to contribute to the commonly observed colloidal deposition problem under unfavorable conditions. Therefore, future work focusing on the unfavorable depositions conditions needs to be conducted with our setup to elucidate the underlying mechanisms.

6.2.2 Oil displacement by water at pore scales

In Chapter 5, we have demonstrated our ability to make bead-based porous media with tunable wettabilities. Therefore, it would be interesting to study the oil displacement by water under different configurations. For example, in the random mixture of hydrophobic and hydrophilic bead packing, we assumed that the overall water saturation after invading would increase as the fraction of hydrophilic beads increases. However, there could be a critical ratio beyond which the invading water will find a preferential path that are connected by those hydrophilic beads. Once this preferential path is established, water saturation in the porous media will no longer increase. Such a hypothesis needs to be tested. Another interesting phenomenon to study would be the displacement pattern at the pore scales. For example, how would the invading front behave when it encounters pores made of both hydrophilic and hydrophobic beads. Would the direction of the flow matter under such a scenario? In addition, some surfactant molecules can change not only the interfacial tension between water and oil but also the wettability of the porous media. With our setup, we could further study the wettability alternation effect on water-oil displacement.

REFERENCE

(1) Xu, K.; Liang, T.; Zhu, P.; Qi, P.; Lu, J.; Huh, C.; Balhoff, M. A 2.5-D Glass Micromodel for Investigation of Multi-Phase Flow in Porous Media. *Lab Chip* **2017**, *17* (4), 640–646.

(2) Krummel, A. T.; Datta, S. S.; Munster, S.; Weitz, D. A. Visualizing Multiphase Flow and Trapped Fluid Configurations in a Model Three-Dimensional Porous Medium. *AIChE J.* **2013**, *59* (3), 1022–1029.

(3) Liu, Y.; Zhang, C.; Hu, D.; Kuhlenschmidt, M. S.; Kuhlenschmidt, T. B.; Mylon, S. E.; Kong, R.; Bhargava, R.; Nguyen, T. H. Role of Collector Alternating Charged Patches on Transport of Cryptosporidium Parvum Oocysts in a Patchwise Charged Heterogeneous Micromodel. *Environ. Sci. Technol.* **2013**, *47*, 2670–2678.

(4) Song, W.; de Haas, T. W.; Fadaei, H.; Sinton, D. Chip-off-the-Old-Rock: The Study of Reservoir-Relevant Geological Processes with Real-Rock Micromodels. *Lab Chip* **2014**, *14*, 4382–4390.

(5) Li, J.; Chen, D.; Chen, G. Low-Temperature Thermal Bonding of PMMA Microfluidic Chips. *Anal. Lett.* **2005**, *38*, 1127–1136.

(6) Anna, S. L.; Bontoux, N.; Stone, H. A. Formation of Dispersions Using “Flow Focusing” in Microchannels. *Appl. Phys. Lett.* **2003**, *82* (3), 364–366.

(7) Xiao, S.; Zeng, Y.; Vavra, E. D.; He, P.; Puerto, M.; Hirasaki, G. J.; Biswal, S. L. Destabilization, Propagation, and Generation of Surfactant-Stabilized Foam during Crude Oil Displacement in Heterogeneous Model Porous Media. *Langmuir* **2018**, *34* (3), 739–749.

(8) Ryan, J. N.; Elimelech, M. Colloid Mobilization and Transport in Groundwater. *Colloids Surfaces A Physicochem. Eng. Asp.* **1996**, *107*, 1–56.

(9) McCarthy, J.; Zachara, J. Subsurface Transport of Contaminants. *Environ. Sci. Technol.* **1989**, *23*, 496–502.

(10) Tanaka, S.; Nagasaki, S. Impact of Colloid Generation Nn Actinide Migration in High-Level Radioactive Waste Disposal: Overview and Laboratory Analysis. *Nucl. Technol.* **1996**, *118*, 58–68.

(11) Kersting, A. B.; Efurd, D. W.; Finnegan, D. L.; Rokop, D. J.; Smith, D. K.; Thompson, J. L. Migration of Plutonium in Ground Water at the Nevada Test Site. *Nature* **1999**, *397*, 56–59.

(12) Karathanasis, A. D. Subsurface Migration of Copper and Zinc Mediated by Soil Colloids. *Soil Sci. Soc. Am. J.* **1999**, *63*, 830–838.

(13) Kretzschmar, R.; Borkovec, M.; Grolimund, D.; Elimelech, M. Mobile Subsurface Colloids and Their Role in Contaminant Transport. *Adv. Agron.* **1999**, *66*, 121–193.

(14) Roy, S. B.; Dzombak, D. A. Colloid Release and Transport Processes in Natural and Model Porous Media. *Colloids Surfaces A Physicochem. Eng. Asp.* **1996**, *107*, 245–262.

(15) Villholth, K. G. Colloid Characterization and Colloidal Phase Partitioning of Polycyclic Aromatic Hydrocarbons in Two Creosote-Contaminated Aquifers in Denmark. *Environ. Sci. Technol.* **1999**, *33*, 691–699.

(16) Chalmers, R. M. Waterborne Outbreaks of Cryptosporidiosis. *Ann Ist Super Sanità* **2012**, *48* (4), 429–416.

(17) MacKenzie, W. R. A Massive Outbreak in Milwaukee of Cryptosporidium Infection Transmitted Through the Public Water Supply. *N. Engl. J. Med.* **1994**, *331*, 161–167.

(18) Brennen, C. E. *Fundamentals of Multiphase Flow*; 2005.

(19) Ma, K.; Rivera, J.; Hirasaki, G. J.; Biswal, S. L. Wettability Control and Patterning of PDMS Using UV-Ozone and Water Immersion. *J. Colloid Interface Sci.* **2011**, *363* (1), 371–378.

(20) Benson, S. M.; Cole, D. R. Sequestration in Deep Sedimentary Formations. *Elements* **2008**, *5*, 325–331.

(21) Soga, K.; Page, J. W. E.; Illangasekare, T. H. A Review of NAPL Source Zone Remediation Efficiency and the Mass Flux Approach. *J. Hazard. Mater.* **2004**, *110* (1–3), 13–27.

(22) Maruyama, T.; Matsushita, H.; Uchida, J. I.; Kubota, F.; Kamiya, N.; Goto, M. Liquid Membrane Operations in a Microfluidic Device for Separation of Metal Ions. *Anal. Chem.* **2004**, *76* (15), 4495–4500.

(23) Muggeridge, A.; Cockin, A.; Webb, K.; Frampton, H.; Collins, I.; Moulds, T.; Salino, P. Recovery Rates, Enhanced Oil Recovery and Technological Limits. *Philos. Trans. R. Soc. A Math. Phys. Eng. Sci.* **2014**, *372*, 1–25.

(24) Saiers, J. E.; Hornberger, G. M. The Role of Colloidal Kaolinite in the Transport of Cesium through Laboratory Sand Columns. **1996**, *32* (1), 33–41.

(25) Penrose, W. R.; Polzer, W. L.; Essington, E. H.; Nelson, D. M.; Orlandini, K. A. Mobility of Plutonium and Americium through a Shallow Aquifer in a Semiarid Region. *Environ. Sci. Technol.* **1990**, *24* (2), 228–234.

(26) Grolimund, D.; Borkovec, M.; Barmettler, K.; Sticher, H. Colloid-Facilitated Transport of Stronlgy Sorbing Contaminants in Natural Porous Media: A Laboratory Column Study. *Environ. Sci. Technol.* **1996**, *30* (10), 3118–3123.

(27) Grolimund, D.; Borkovec, M. Release of Colloidal Particles in Natural Porous Media by Monovalent and Divalent Cations. *J. Contam. Hydrol.* **2006**, *87* (3–4), 155–175.

(28) Champ, D. R.; Merritt, W. F.; Young, J. L.; Cnalk, T.; Nuclear, R.; River, C. Potential for the Rapid Transorp of Plutonium in Groundwater as Demonstrated by Core Column Studies. *Sci. Basis Radioact. Waste Manag.* **1982**, 745–754.

(29) Buddemeier, R. W.; Hunt, J. R. Transport of Colloidal Contaminants in Groundwater: Radionuclide Migration at the Nevada Test Site. *Appl. Geochemistry* **1988**, *3* (5), 535–548.

(30) Frimmel, F. H.; Kammer, F. von der; Flemming, H.-C. *Colloidal Transport in Porous Media*; 2007.

(31) Ptak, T.; Piepenbrink, M.; Martac, E. Tracer Tests for the Investigation of Heterogeneous Porous Media and Stochastic Modelling of Flow and Transport — a Review of Some Recent Developments. **2004**, *294*, 122–163.

(32) Bösel, D.; Herfort, M.; Ptak, T.; Teutsch, G. Design, Performance, Evaluation and Modelling of a Natural Gradient Multitracer Transport Experiment in a Contaminated Heterogeneous Porous Aquifer. *Tracers Model. Hydrogeol.* **2000**, *262*, 45–51.

(33) Herfort, M.; Ptak, T.; Uranin, M.; Transportgleichung, D.; Abstands-, D. Z. Multitracer-Versuch Im Kontaminierten Grund- Wasser Des Testfeldes Süd. *Grundwasser* **2002**, *7*, 31–40.

(34) Rugge, K.; Bjerg, P. L.; Pedersen, J. K.; Mosbaek, H.; Christensen, T. H. An Anaerobic Field Injection Experiment in a Landfill Leachate Plume, Grindsted, Denmark 1. Experimental Setup, Tracer Movement, and Fate of Aromatic and Chlorinated Compounds. *Water Resour. Res.* **1999**, *35*, 1231–1246.

(35) Harvey, R.; Garabedian, S. Use of Colloid Filtration Theory in Modeling Movement of Bacteria through a Contaminated Sandy Aquifer. *Environ. Sci. Technol.* **1991**, *25* (1), 178–185.

(36) Chen, J. S.; Chen, C. S.; Gau, H. S.; Liu, C. W. A Two-Well Method to Evaluate Transverse Dispersivity for Tracer Tests in a Radially Convergent Flow Field. *J. Hydrol.* **1999**, *223*, 175–197.

(37) Fernàndez-Garcia, D.; Sánchez-Vila, X.; Illangasekare, T. H. Convergent-Flow Tracer Tests in Heterogeneous Media: Combined Experimental-Numerical Analysis for Determination of Equivalent Transport Parameters. *J. Contam. Hydrol.* **2002**, *57*, 129–145.

(38) Ptak, T.; Teutsch, G. Forced and Natural Gradient Tracer Tests in a Highly Heterogeneous Porous Aquifer: Instrumentation and Measurements. *J. Hydrol.* **1994**, *159* (1–4), 79–104.

(39) Brusseau, M. L.; Srivastava, R. Nonideal Transport of Reactive Solutes in Heterogeneous Porous Media. 4. Analysis of the Cape Cod Natural-Gradient Field Experiment. *Water Resour. Res.* **1999**, *35*, 1113–1125.

(40) Annable, M. D.; Jawitz, J. W.; Rao, P. S. C.; Dai, D. P.; Kim, H.; Wood, A. L. Field Evaluation of Interfacial and Partitioning Tracers for Characterization of Effective NAPL-Water Contact Areas. *Ground Water* **1998**, *36*, 495–502.

(41) 1998_annable_hill Tracers.Pdf.

(42) Loveland, J. P.; Bhattacharjee, S.; Ryan, J. N.; Elimelech, M. Colloid Transport in a Geochemically Heterogeneous Porous Medium: Aquifer Tank Experiment and Modeling. *J. Contam. Hydrol.* **2003**, *65* (3–4), 161–182.

(43) Loveland, J. P.; Bhattacharjee, S.; Ryan, J. N.; Elimelech, M. Colloid Transport in a Geochemically Heterogeneous Porous Medium: Aquifer Tank Experiment and Modeling. *J. Contam. Hydrol.* **2003**, *65* (3–4), 161–182.

(44) Grolimund, D.; Elimelech, M.; Borkovec, M.; Barmettler, K.; Kretzschmar, R.; Sticher, H. Transport of in Situ Mobilized Colloidal Particles in Packed Soil Columns. *Environ. Sci. Technol.* **1998**, *32*, 3562–3569.

(45) Bradford, S. A.; Simunek, J.; Bettahar, M.; Van Genuchten, M. T.; Yates, S. R. Significance of Straining in Colloid Deposition: Evidence and Implications. *Water Resour. Res.* **2006**, *42* (12), 1–16.

(46) Torok, J.; Buckley, L. .; Woods, B. . The Separation of Radionuclide Migration by Solution and Particle Transport in Soil. *J. Contam. Hydrol.* **1990**, *6*, 185–203.

(47) Puls, R. W.; Powell, R. M. Transport of Inorganic Colloids through Natural Aquifer Material: Implications for Contaminant Transport. *Environ. Sci. Technol.* **1992**, *26*, 614–621.

(48) Amrhein, C.; Mosher, P. A.; Strong, J. E. Colloid-Assisted Transport of Trace Metals in Roadside Soils Receiving Deicing Salts. *Soil Sci. Soc. Am. J.* **1993**, *57*, 1212–1217.

(49) Yao, K. M.; Habibian, M. T.; O'Melia, C. R. Water and Waste Water Filtration. Concepts and Applications. *Environ. Sci. Technol.* **1971**, *5* (11), 1105–1112.

(50) Elimelech, M.; Nagai, M.; Ko, C. H.; Ryan, J. N. Relative Insignificance of Mineral Grain Zeta Potential to Colloid Transport in Geochemically Heterogeneous Porous Media. *Environ. Sci. Technol.* **2000**, *34* (11), 2143–2148.

(51) Chen, J. Y.; Ko, C. H.; Bhattacharjee, S.; Elimelech, M. Role of Spatial Distribution of Porous Medium Surface Charge Heterogeneity in Colloid Transport. *Colloids Surfaces A Physicochem. Eng. Asp.* **2001**, *191*, 3–15.

(52) Johnson, P. R.; Sun, N.; Elimelech, M. Colloid Transport in Geochemically Heterogeneous Porous Media : Modeling and Measurements. *Environ. Sci. Technol.* **1996**, *30*, 3284–3293.

(53) Bradford, S. A.; Yates, S. R.; Bettahar, M.; Simunek, J. Physical Factors Affecting the

Transport and Fate of Colloids in Saturated Porous Media. *Water Resour. Res.* **2002**, *38*, 63-1-63–12.

(54) Rajagopalan, R.; Tien, C. Trajectory Analysis of Deep Bed Filtration with the Sphere-in-Cell Porous Media Model. *Aiche J.* **1976**, *22* (3), 523–533.

(55) Happel, J. Viscous Flow in Multiparticle Systems: Slow Motion of Fluids Relative to Beds of Spherical Particles. *AIChE J.* **1958**, *4* (2), 197–201.

(56) Tufenkji, N.; Elimelech, M. Correlation Equation For Predicting Single-Collector Eficiency in Physiochemical Filtration in Saturated Porous Media. *Environ. Sci. Technol.* **2004**, *38*, 529–536.

(57) Tufenkji, N.; Elimelech, M. Deviation from the Classical Colloid Filtration Theory in the Presence of Repulsive DLVO Interactions. *Langmuir* **2004**, *20*, 10818–10828.

(58) Tufenkji, N.; Redman, J. A.; Elimelech, M. Interpreting Deposition Patterns of Microbial Particles in Laboratory-Scale Column Experiments. *Environ. Sci. Technol.* **2003**, *37*, 616–623.

(59) N. K. Karadimitriou and S. M. Hassanizadeh. A Review of Micromodels and Their Use in Two-Phase Flow Studies. *Vadose Zo. J.* **2012**, *11*, 1539–1563.

(60) Lenormand, R.; Zarcone, C. Invasion Percolation in an Etched Network: Measurement of a Fractal Dimension. *Phys. Rev. Lett.* **1985**, *54*, 2226–2229.

(61) Wu, M.; Xiao, F.; Johnson-Paben, R. M.; Retterer, S. T.; Yin, X.; Neeves, K. B. Single- and Two-Phase Flow in Microfluidic Porous Media Analogs Based on Voronoi Tessellation. *Lab Chip* **2012**, *12*, 253–261.

(62) Kumar Gunda, N. S.; Bera, B.; Karadimitriou, N. K.; Mitra, S. K.; Hassanizadeh, S. M. Reservoir-on-a-Chip (ROC): A New Paradigm in Reservoir Engineering. *Lab Chip* **2011**, *11*, 3785–3792.

(63) Xu, W.; Ok, J. T.; Xiao, F.; Neeves, K. B.; Yin, X.; Xu, W.; Ok, J. T.; Xiao, F.; Neeves, K. B. Effect of Pore Geometry and Interfacial Tension on Water-Oil Displacement Efficiency in Oil-Wet Microfluidic Porous Media Analogs Effect of Pore Geometry and Interfacial Tension on Water-Oil Displacement Efficiency in Oil-Wet Microfluidic Porous. *Phys. Fluids* **2014**, *26*, 093102.

(64) Yadali Jamaloei, B.; Kharrat, R. Fundamental Study of Pore Morphology Effect in Low Tension Polymer Flooding or Polymer-Assisted Dilute Surfactant Flooding. *Transp. Porous Media* **2009**, *76*, 199–218.

(65) Bowden, S. A.; Cooper, J. M.; Greub, F.; Tambo, D.; Hurst, A. Benchmarking Methods of Enhanced Heavy Oil Recovery Using a Microscaled Bead-Pack. *Lab Chip* **2010**, *10*, 819–823.

(66) Auset, M.; Keller, A. A. Pore-Scale Processes That Control Dispersion of Colloids in Saturated Porous Media. *Water Resour. Res.* **2004**, *40*, W03503.

(67) Baumann, T.; Werth, C. J. Visualization and Modeling of Polystyrol Colloid Transport in a Silicon Micromodel. *Vadose Zo. J.* **2004**, *3*, 434–443.

(68) Auset, M.; Keller, A. Pore-Scale Visualization of Colloid Straining and Filtration in Saturated Porous Media Using Micromodels. *Water Resour. Res.* **2006**, *42*, 1–9.

(69) Corapcioglu, M. Y.; Fedirchuk, P. Glass Bead Micromodel Study of Solute Transport. *J. Contam. Hydrol.* **1999**, *36*, 209–230.

(70) Mattax, C. C.; Kyte, J. R. Ever See a Water Flood. *Oil and Gas journal*. 1961, pp 123–128.

(71) Lenormand, R.; Touboul, E.; Zarcone, C. Numerical Models and Experiments on Immiscible Displacements in Porous Media. *J. Fluid Mech.* **1988**, *189* (1), 165.

(72) Lenormand, R.; Zarcone, C. Capillary Fingering: Percolation and Fractal Dimension. *Transp. Porous Media* **1989**, *4* (6), 599–612.

(73) Iliescu, C.; Chen, B.; Miao, J. On the Wet Etching of Pyrex Glass. *Sensors Actuators, A* **2008**, *143*, 154–161.

(74) Zhang, C.; Oostrom, M.; Wietsma, T. W.; Grate, J. W.; Warner, M. G. Influence of Viscous and Capillary Forces on Immiscible Fluid Displacement: Pore-Scale Experimental Study in a Water-Wet Micromodel Demonstrating Viscous and Capillary Fingering. *Energy and Fuels* **2011**, *25* (8), 3493–3505.

(75) Madou, M. J. *Fundamentals of Microfabrication*; 1997.

(76) Basoy, N. G.; Danilychev, V. A.; Popov, Y. M.; Khodkevich, D. D. Laser Operating in the Vacuum Region of the Spectrum by Excitation of Liquid Xenon with an Electron Beam ♯. *JETP Lett.* **1970**.

(77) Blauw, M. A.; Zijlstra, T.; van der Drift, E. Balancing the Etching and Passivation in Time-Multiplexed Deep Dry Etching of Silicon. *J. Vac. Sci. Technol. B Microelectron. Nanom. Struct.* **2001**, *19*, 2930–2934.

(78) Yeom, J.; Wu, Y.; Selby, J. C.; Shannon, M. A. Maximum Achievable Aspect Ratio in Deep Reactive Ion Etching of Silicon Due to Aspect Ratio Dependent Transport and the Microloading Effect. *J. Vac. Sci. Technol. B Microelectron. Nanom. Struct.* **2005**, *23*, 2319–2329.

(79) Hull, C. W. Patent: Apparatus for Production of Three-Dimensional Objects by Stereolithography, 1986.

(80) Anbari, A.; Chien, H.; Datta, S. S.; Deng, W.; Weitz, D. A. Microfluidic Model Porous

Media : Fabrication and Applications. *Small* **2018**, *1703575*, 1–15.

(81) Melchels, F. P. W.; Feijen, J.; Grijpma, D. W. A Review on Stereolithography and Its Applications in Biomedical Engineering. *Biomaterials* **2010**, *31* (24), 6121–6130.

(82) D'urso, P. S.; Earwaker, W. J.; Barker, T. M.; Redmond, M. J.; Thompson, R. G.; Effeney, D. J.; Tomlinson, F. H. Custom Cranioplasty Using Stereolithography and Acrylic. *Br. J. Plast. Surg.* **2000**, *53*, 200–204.

(83) Popov, V. K.; Evseev, A. V; Howdle, S. M. Laser Stereolithography and Supercritical Fluid Processing for Custom-Designed Implant Fabrication. *J. Mater. Sci. Mater. Med.* **2004**, *15*, 123–128.

(84) Langer, R.; Vacanti, J. P. Tissue Engineering. *Science (80-.).* **1993**, *260*, 920–928.

(85) Wurm, G.; Tomancok, B.; Holl, K.; Trenkler, J. Prospective Study on Cranioplasty with Individual Carbon Fiber Reinforced Polymere (CFRP) Implants Produced by Means of Stereolithography. *Surg. Neurol.* **2004**, *62*, 510–521.

(86) Jansen, J.; Melchels, F. P. W.; Grijpma, D. W.; Feijen, J. Fumaric Acid Monoethyl Ester-Functionalized Poly(D,L-Lactide)/N-Vinyl-2- Pyrrolidone Resins for the Preparation of Tissue Engineering Scaffolds by Stereolithography. *Biomacromolecules* **2009**, *10*, 214–220.

(87) Dendukuri, D.; Gu, S. S.; Pregibon, D. C.; Hatton, T. A.; Doyle, P. S. Stop-Flow Lithography in a Microfluidic Device. *Lab Chip* **2007**, *7* (7), 818–828.

(88) Duffy, D. C.; McDonald, J. C.; Schueller, O. J. A.; Whitesides, G. M. Rapid Prototyping of Microfluidic Systems in Poly(Dimethylsiloxane). *Anal. Chem.* **1998**, *70* (23), 4974–4984.

(89) Larsen, A. C.; Dunn, M. R.; Hatch, A.; Sau, S. P.; Youngbull, C.; Chaput, J. C. A General Strategy for Expanding Polymerase Function by Droplet Microfluidics. *Nat. Commun.* **2016**, *7*, 1–9.

(90) Bartolo, D.; Degré, G.; Nghe, P.; Studer, V. Microfluidic Stickers. *Lab Chip* **2008**, *8*, 274–279.

(91) Cygan, Z. T.; Cabral, J. T.; Beers, K. L.; Amis, E. J. Microfluidic Platform for the Generation of Organic-Phase Microreactors. *Langmuir* **2005**, *21* (8), 3629–3634.

(92) Love, J. C.; Wolfe, D. B.; Jacobs, H. O.; Whitesides, G. M. Microscope Projection Photolithography for Rapid Prototyping of Masters with Micron-Scale Features for Use in Soft Lithography. *Langmuir* **2001**, *17* (19), 6005–6012.

(93) Dendukuri, D.; Pregibon, D. C.; Collins, J.; Hatton, T. A.; Doyle, P. S. Continuous-Flow Lithography for High-Throughput Microparticle Synthesis. *Nat. Mater.* **2006**, *5* (5), 365–369.

(94) Lee, H.; Lee, S. G.; Doyle, P. S. Photopatterned Oil-Reservoir Micromodels with Tailored Wetting Properties. *Lab Chip* **2015**, *15* (14), 3047–3055.

(95) Chatenever, A.; Calhoun, J. C. Visual Examinations of Fluid Behavior in Porous Media - Part I. *J. Pet. Technol.* **1952**, *4* (06), 149–156.

(96) Datta, S. S.; Chiang, H.; Ramakrishnan, T. S.; Weitz, D. A. Spatial Fluctuations of Fluid Velocities in Flow through a Three-Dimensional Porous Medium. *Phys. Rev. Lett.* **2013**, *111* (6), 1–5.

(97) Lenormand, R. Flow Through Porous Media: Limits of Fractal Patterns. *Proc. R. Soc. A Math. Phys. Eng. Sci.* **1989**, *423* (1864), 159–168.

(98) Lenormand, R.; Zarcone, C.; Sarr, A. Mechanisms of the Displacement of One Fluid by Another in a Network of Capillary Ducts. *J. Fluid Mech.* **1983**, *135* (July), 337.

(99) Wan, J.; Wilson, J. L. Visualization of the Role of the Gas-Water Interface on the Fate and Transport of Colloids in Porous Media. *Water Resour. Res.* **1994**, *30*, 11–23.

(100) Corapcioglu, Y. M.; Chowdhury, S.; Roosevelt, S. E. Micromodel Visualization and Quantification of Solute Transport in Porous Media. *Water Resour. Res.* **1997**, *33* (11), 2547.

(101) Sirivithayapakorn, S.; Keller, A. Transport of Colloids in Saturated Porous Media: A Pore-Scale Observation of the Size Exclusion Effect and Colloid Acceleration. *Water Resour. Res.* **2003**, *39* (4), 1109.

(102) Brown, D. G.; Abramson, A. Collision Efficiency Distribution of a Bacterial Suspension Flowing through Porous Media and Implications for Field-Scale Transport. *Water Res.* **2006**, *40* (8), 1591–1598.

(103) Baumann, T.; Toops, L.; Niessner, R. Colloid Dispersion on the Pore Scale. *Water Res.* **2010**, *44*, 1246–1254.

(104) Liu, Y.; Zhang, C.; Hilpert, M.; Kuhlenschmidt, M. S.; Kuhlenschmidt, T. B.; Nguyen, T. H. Transport of Cryptosporidium ParvumOocysts in a Silicon Micromodel. *Environ. Sci. Technol.* **2012**, 120127160321002.

(105) Elimelech, M.; Chen, J. Y.; Kuznar, Z. A. Particle Deposition onto Solid Surfaces with Microscopic Charge Heterogeneity: The "Bump Effect." *Langmuir* **2003**, No. 19, 6594–6597.

(106) Lenormand, R.; Touboul, E.; Zarcone, C. Numerical Models and Experiments on Immiscible Displacements in Porous Media. *J. Fluid Mech.* **1988**, *189* (April 1988), 165–187.

(107) Chen, Y. F.; Fang, S.; Wu, D. S.; Hu, R. Visualizing and Quantifying the Crossover from Capillary Fingering to Viscous Fingering in a Rough Fracture. *Water Resour. Res.* **2017**,

53 (9), 7756–7772.

(108) Abdallah, W.; Buckley, J. S.; Carnegie, A.; Edwards, J.; Herold, B.; Fordham, E.; Graue, A.; Habashy, T.; Seleznev, N.; Signer, C.; et al. Fundamentals of Wettability. *Oilf. Rev.* **2007**.

(109) Treiber, L. E.; Owens, W. W. A Laboratory Evaluation of the Wettability of Fifty Oil-Producing Reservoirs. *Soc. Pet. Eng. J.* **1972**, *12*, 531–540.

(110) Trojer, M.; Szulczewski, M. L.; Juanes, R. Stabilizing Fluid-Fluid Displacements in Porous Media Through Wettability Alteration. *Phys. Rev. Appl.* **2015**, *3* (5), 1–8.

(111) Zhao, B.; Macminn, C. W.; Juanes, R. Wettability Control on Multiphase Flow in Patterned Microfluidics. *Proc. Natl. Acad. Sci. U. S. A.* **2016**, *113*, 10251–10256.

(112) Gao, H.; Han, J.; Jin, Y.; Wang, L. Modeling Microscale Flow and Colloid Transport in Saturated Porous Media. No. February 2008.

(113) Gao, H.; Qiu, C. Q.; Fan, D.; Jin, Y.; Wang, L. P. Three-Dimensional Microscale Flow Simulation and Colloid Transport Modeling in Saturated Soil Porous Media. *Comput. Math. with Appl.* **2010**, *59* (7), 2271–2289.

(114) Pham, N. H.; Swatske, D. P.; Harwell, J. H.; Shiau, B. J.; Papavassiliou, D. V. Transport of Nanoparticles and Kinetics in Packed Beds: A Numerical Approach with Lattice Boltzmann Simulations and Particle Tracking. *Int. J. Heat Mass Transf.* **2014**, *72*, 319–328.

(115) Pham, N. H.; Papavassiliou, D. V. Effect of Spatial Distribution of Porous Matrix Surface Charge Heterogeneity on Nanoparticle Attachment in a Packed Bed. *Phys. Fluids* **2017**, *29* (8).

(116) Johnson, W. P.; Rasmuson, A.; Pazmiño, E.; Hilpert, M. Why Variant Colloid Transport Behaviors Emerge among Identical Individuals in Porous Media When Colloid-Surface Repulsion Exists. *Environ. Sci. Technol.* **2018**, *52*, 7230–7239.

(117) Guo, Y.; Huang, J.; Xiao, F.; Yin, X.; Chun, J.; Um, W.; Neeves, K. B.; Wu, N. Bead-Based Microfluidic Sediment Analogues: Fabrication and Colloid Transport. *Langmuir* **2016**, *32*, 9342–9350.

(118) Seymour, M. B.; Chen, G.; Su, C.; Li, Y. Transport and Retention of Colloids in Porous Media: Does Shape Really Matter? *Environ. Sci. Technol.* **2013**, *47*, 8391–8398.

(119) Russom, A.; Haasl, S.; Ohlander, A.; Mayr, T.; Brookes, A. J.; Andersson, H.; Stemme, G. Genotyping by Dynamic Heating of Monolayered Beads on a Microheated Surface. *Electrophoresis* **2004**, *25*, 3712–3719.

(120) Grumann, M.; Dobmeier, M.; Schippers, P.; Brenner, T.; Kuhn, C.; Fritsche, M.; Zengerle, R.; Ducréea, J. Aggregation of Bead-Monolayers in Flat Microfluidic Chambers

Simulation by the Model of Porous Media. *Lab Chip* **2004**, *4*, 209–213.

(121) Seong, G. H.; Heo, J.; Crooks, R. M. Measurement of Enzyme Kinetics Using a Continuous-Flow Microfluidic System. *Anal. Chem.* **2003**, *75*, 5206–5212.

(122) Lee, J.; Kim, O.; Jung, J.; Na, K.; Heo, P.; Hyun, J. Simple Fabrication of a Smart Microarray of Polystyrene Microbeads for Immunoassay. *Colloids Surfaces B Biointerfaces* **2009**, *72*, 173–180.

(123) Xia, Y.; Whitesides, G. M. Soft Lithography. *Annu. Rev. Mater. Sci.* **1998**, *28*, 153–184.

(124) Garstecki, P.; Fuerstman, M. J.; Stone, H. A.; Whitesides, G. M. Formation of Droplets and Bubbles in a Microfluidic T-Junction-Scaling and Mechanism of Break-Up. *Lab Chip* **2006**, *6*, 437–446.

(125) van Steijn, V.; Kleijn, C. R.; Kreutzer, M. T. Predictive Model for the Size of Bubbles and Droplets Created in Microfluidic T-Junctions. *Lab Chip* **2010**, *10*, 2513–2518.

(126) Schneider, T.; Burnham, D. R.; VanOrden, J.; Chiu, D. T. Systematic Investigation of Droplet Generation at T-Junctions. *Lab Chip* **2011**, *11*, 2055–2059.

(127) Preibisch, S.; Saalfeld, S.; Tomancak, P. Globally Optimal Stitching of Tiled 3D Microscopic Image Acquisitions. *Bioinformatics* **2009**, *25*, 1463–1465.

(128) Canny, J. A Computational Approach to Edge Detection. *IEEE Trans. Pattern Anal. Mach. Intell.* **1986**, *8*, 679–698.

(129) Montero, R. S.; Bribiesca, E. State of the Art of Compactness and Circularity Measures. *Int. Math. Forum* **2009**, *4*, 1305–1335.

(130) Cornish, R. J. Flow in a Pipe of Rectangular Cross-Section. *Proc. R. Soc. A Math. Phys. Eng. Sci.* **1928**, *120*, 691–700.

(131) Verruijt, A. *Soil Mechanics*, 1st ed.; Delft University of Technology, 2004.

(132) Carman, P. C. Fluid Flow through Granular Beds. *Chem. Eng. Res. Des.* **1997**, *75*, S32–S48.

(133) Pace, M. N.; Mayes, M. A.; Jardine, P. M.; Mehlhorn, T. L.; Zachara, J. M.; Bjornstad, B. N. Quantifying the Effects of Small-Scale Heterogeneities on Flow and Transport in Undisturbed Core from the Hanford Formation. *Vadose Zo. J.* **2005**, *4*, 1220–1223.

(134) Scown, T. M.; Van Aerle, R.; Tyler, C. R. Review: Do Engineered Nanoparticles Pose a Significant Threat to the Aquatic Environment. *Crit. Rev. Toxicol.* **2010**, *40*, 653–670.

(135) Choi, O.; Yu, C. P.; Esteban Fernández, G.; Hu, Z. Interactions of Nanosilver with Escherichia Coli Cells in Planktonic and Biofilm Cultures. *Water Res.* **2010**, *44*, 6095–6103.

(136) Smith, C. J.; Shaw, B. J.; Handy, R. D. Toxicity of Single Walled Carbon Nanotubes to Rainbow Trout, (Oncorhynchus Mykiss): Respiratory Toxicity, Organ Pathologies, and Other Physiological Effects. *Aquat. Toxicol.* **2007**, *82*, 94–109.

(137) Handy, R. D.; Von Der Kammer, F.; Lead, J. R.; Hassellöv, M.; Owen, R.; Crane, M. The Ecotoxicology and Chemistry of Manufactured Nanoparticles. *Ecotoxicology* **2008**, *17*, 287–314.

(138) Ahmed, F.; Rodrigues, D. F. Investigation of Acute Effects of Graphene Oxide on Wastewater Microbial Community: A Case Study. *J. Hazard. Mater.* **2013**, *256–257*, 33–39.

(139) Jung, H.; Navarre-Sitchler, A. Physical Heterogeneity Control on Effective Mineral Dissolution Rates. *Geochim. Cosmochim. Acta* **2018**, *227*, 246–263.

(140) Mccarthy, J. F.; Mckay, L. D. Colloid Transport in the Subsurface : Past , Present , and Future Challenges. **2004**, 326–337.

(141) Rod, K.; Um, W.; Chun, J.; Wu, N.; Yin, X.; Wang, G.; Neeves, K. Effect of Chemical and Physical Heterogeneities on Colloid-Facilitated Cesium Transport. *J. Contam. Hydrol.* **2018**, *213*, 22–27.

(142) Molnar, I. L.; Gerhard, J. I.; Willson, C. S.; O'Carroll, D. M. The Impact of Immobile Zones on the Transport and Retention of Nanoparticles in Porous Media. *Water Resour. Res.* **2015**, *51*, 8973–8994.

(143) Babakhani, P.; Bridge, J.; Doong, R. an; Phenrat, T. Continuum-Based Models and Concepts for the Transport of Nanoparticles in Saturated Porous Media: A State-of-the-Science Review. *Adv. Colloid Interface Sci.* **2017**, *246*, 75–104.

(144) Li, X.; Johnson, W. P. Nonmonotonic Variations in Deposition Rate Coefficients of Microspheres in Porous Media under Unfavorable Deposition Conditions. *Environ. Sci. Technol.* **2005**, *39*, 1658–1665.

(145) Goldberg, E.; Scheringer, M.; Bucheli, T. D.; Hungerbuhler, K. Critical Assessment of Models for Transport of Engineered Nanoparticles in Saturated Porous Media. *Environ. Sci. Technol.* **2014**, *48*, 12732–12741.

(146) Johnson, W. P.; Rasmuson, A.; Pazmiño, E.; Hilpert, M. Why Variant Colloid Transport Behaviors Emerge among Identical Individuals in Porous Media When Colloid-Surface Repulsion Exists. *Environ. Sci. Technol.* **2018**, *52* (13), 7230–7239.

(147) Keller, A. A.; Auset, M. A Review of Visualization Techniques of Biocolloid Transport Processes at the Pore Scale under Saturated and Unsaturated Conditions. *Adv. Water Resour.* **2007**, *30*, 1392–1407.

(148) Sinton, D. Microscale Flow Visualization. *Microfluid. Nanofluidics* **2004**, *1*, 2–21.

(149) Murison, J.; Semin, B.; Baret, J.; Herminghaus, S.; Schröter, M.; Brinkmann, M. Wetting Heterogeneities in Porous Media Control Flow Dissipation. *Phys. Rev. Appl.* **2014**, *2*, 034002.

(150) Grate, J. W.; Warner, M. G.; Pittman, J. W.; Dehoff, K. J.; Wietsma, T. W.; Zhang, C.; Oostrom, M. Silane Modification of Glass and Silica Surfaces to Obtain Equally Oil-Wet Surfaces in Glass-Covered Silicon Micromodel Applications. *Water Resour. Res.* **2013**, *49* (8), 4724–4729.

(151) Grate, J. W.; Warner, M. G.; Pittman, J. W.; Dehoff, K. J.; Wietsma, T. W.; Zhang, C.; Oostrom, M. Silane Modification of Glass and Silica Surfaces to Obtain Equally Oil-Wet Surfaces in Glass-Covered Silicon Micromodel Applications. *Water Resour. Res.* **2013**, *49*, 4724–4729.

(152) Salles, J.; Thovert, J. -F.; Delannay, R.; Prevors, L.; Auriault, J. -L.; Adler, P. M. Taylor Dispersion in Porous Media. Determination of the Dispersion Tensor. *Phys. Fluids A Fluid Dyn.* **1993**, *5*, 2348–2376.

(153) Maier, R. S.; Kroll, D. M.; Bernard, R. S.; Howington, S. E.; Peters, J. F.; Davis, H. T. Pore-Scale Simulation of Dispersion. *Phys. Fluids* **2000**, *12*, 2065–2079.

(154) Scheibe, T. D.; Perkins, W. A.; Richmond, M. C.; McKinley, M. I.; Romero-Gomez, P. D. J.; Oostrom, M.; Wietsma, T. W.; Serkowski, J. A.; Zachara, J. M. Pore-Scale and Multiscale Numerical Simulation of Flow and Transport in a Laboratory-Scale Column. *Water Resour. Res.* **2015**, *51*, 1023–1035.

(155) Hlushkou, D.; Gritti, F.; Daneyko, A.; Guiochon, G.; Tallarek, U. How Microscopic Characteristics of the Adsorption Kinetics Impact Macroscale Transport in Chromatographic Beds. *J. Phys. Chem. C* **2013**, *117*, 22974–22985.

(156) Hlushkou, D.; Gritti, F.; Guiochon, G.; Seidel-Morgenstern, A.; Tallarek, U. Effect of Adsorption on Solute Dispersion: A Microscopic Stochastic Approach. *Anal. Chem.* **2014**, *86*, 4463–4470.

(157) Schaaf, P.; Talbot, J. Surface Exclusion Effects in Adsorption Processes. *J. Chem. Phys.* **1989**, *91*, 4401–4409.

(158) Adamczyk, Z.; Belouschek, P. Localized Adsorption of Particles on Spherical and Cylindrical Interfaces. *J. Colloid Interface Sci.* **1991**, *146*, 123–136.

(159) D'Humières, D.; Ginzburg, I.; Krafczyk, M.; Lallemand, P.; Luo, L.-S. Multiple-Relaxation-Time Lattice Boltzmann Models in Three Dimensions. *Philos. Trans. A. Math. Phys. Eng. Sci.* **2002**, *360*, 437–451.

(160) Xiao, F.; Yin, X. Geometry Models of Porous Media Based on Voronoi Tessellations and Their Porosity-Permeability Relations. *Comput. Math. with Appl.* **2016**, *72*, 328–348.

(161) Sader, J. E.; Carnie, J. L.; Chan, D. Y. C. Accurate Analytic Formulas for the Double-

Layer Interaction between Spheres. *J. Colloid Interface Sci.* **1995**, *171*, 46–54.

(162) Israelachvili, J. *Intermolecular and Surface Forces*, 3rd ed.; Academic Press: London, UK, 2011.

(163) Ropp, R. C. *Encyclopedia of the Alkaline Earth Compounds*, 1st ed.; Elsevier: Oxford, UK, 2013.

(164) Wu, H. J.; Pangburn, T. O.; Beckham, R. E.; Bevan, M. A. Measurement and Interpretation of Particle-Particle and Particle-Wall Interactions in Levitated Colloidal Ensembles. *Langmuir* **2005**, *21*, 9879–9888.

(165) Rupp, B.; Torres-Díaz, I.; Hua, X.; Bevan, M. A. Measurement of Anisotropic Particle Interactions with Nonuniform Ac Electric Fields. *Langmuir* **2018**, *34*, 2497–2504.

(166) Ghosal, S. Mathematical Modeling of Electrokinetic Effects in Micro and Nano Fluidics. In *Microfluidics and Microfabrication*; Chakraborty, S., Ed.; Springer, Boston, MA, 2010; pp 87–112.

(167) Kampf, N.; Ben-Yaakov, D.; Andelman, D.; Safran, S. A.; Klein, J. Direct Measurement of Sub-Debye-Length Attraction between Oppositely Charged Surfaces. *Phys. Rev. Lett.* **2009**, *103*, 1–4.

(168) Tufenkji, N.; Elimelech, M. Breakdown of Colloid Filtration Theory: Role of the Secondary Energy Minimum and Surface Charge Heterogeneities. *Langmuir* **2005**, *21*, 841–852.

(169) Cho, J. K. PORE-SCALE SIMULATION OF SOLUTE AND COLLOID TRANSPORT AND DIRECT COMPARISON WITH COLUMN AND MICROFLUIDICS EXPERIMENTS, 2018.

(170) Kretzschmar, R.; Barmettler, K.; Grolimund, D.; Yan, Y.; Borkovec, M.; Sticher, H. Experimental Determination of Colloid Deposition Rates and Collision Efficiencies in Natural Porous Media. *Water Resour. Res.* **1997**, *33*, 1129–1137.

(171) Jeong, S. W.; Yavuz Corapcioglu, M. A Micromodel Analysis of Factors Influencing NAPL Removal by Surfactant Foam Flooding. *J. Contam. Hydrol.* **2003**, *60*, 77–96.

(172) Vavra, E. D.; Zeng, Y.; Xiao, S.; Hirasaki, G. J.; Biswal, S. L. Microfluidic Devices for Characterizing Pore-Scale Event Processes in Porous Media for Oil Recovery Applications Microfluidic Devices for Characterizing Pore-Scale Event Processes in Porous Media for Oil. *Recover. Appl. J. Vis. Exp* **2018**, *131*, e56592.

(173) Kenzhekhanov, S. Chemical EOR Process Visualization Using NOA81 Micromodels. **2016**, 1–74.

(174) Graf, C.; Vossen, D. L. J.; Imhof, A.; Blaaderen, A. van. A General Method To Coat Colloidal Particles with Silica. *Langmuir* **2003**, *19*, 6693–6700.

(175) Moisy, F. Boxcount. MATLAB Central File Exchange 2008.

(176) Anna, S. L. Droplets and Bubbles in Microfluidic Devices. *Annu. Rev. Fluid Mech.* **2016**, *48*, 285–309.

APPENDIX

SUPPLEMENTAL ELECTRONIC FILES

The videos in the supplemental materials demonstrate our ability to observe colloidal particle deposition at single pore level. Video S1 showed the colloidal particle deposition under a 60X objective field of view. Video S2 is a zoom in of colloidal particle deposition on a single “+” bead.

Video S1	Colloidal deposition in the heterogeneous surface charge porous medium. Where red beads indicate "+" beads, blue beads are "-" beads and green dots are "-" colloidal particles.
Video S2	Colloidal deposition on a single "+" bead.